Experimental investigation of PdTe2, doped PdTe2 and BiCh2 superconductors

Salis, M.V.

Publication date
2023
Document Version
Final published version

Experimental Investigation of $PdTe_2$, Doped $PdTe_2$ and $BiCh_2$ Superconductors

Marc. V. Salis

Experimental Investigation of $PdTe_2$, Doped $PdTe_2$ and $BiCh_2$ Superconductors

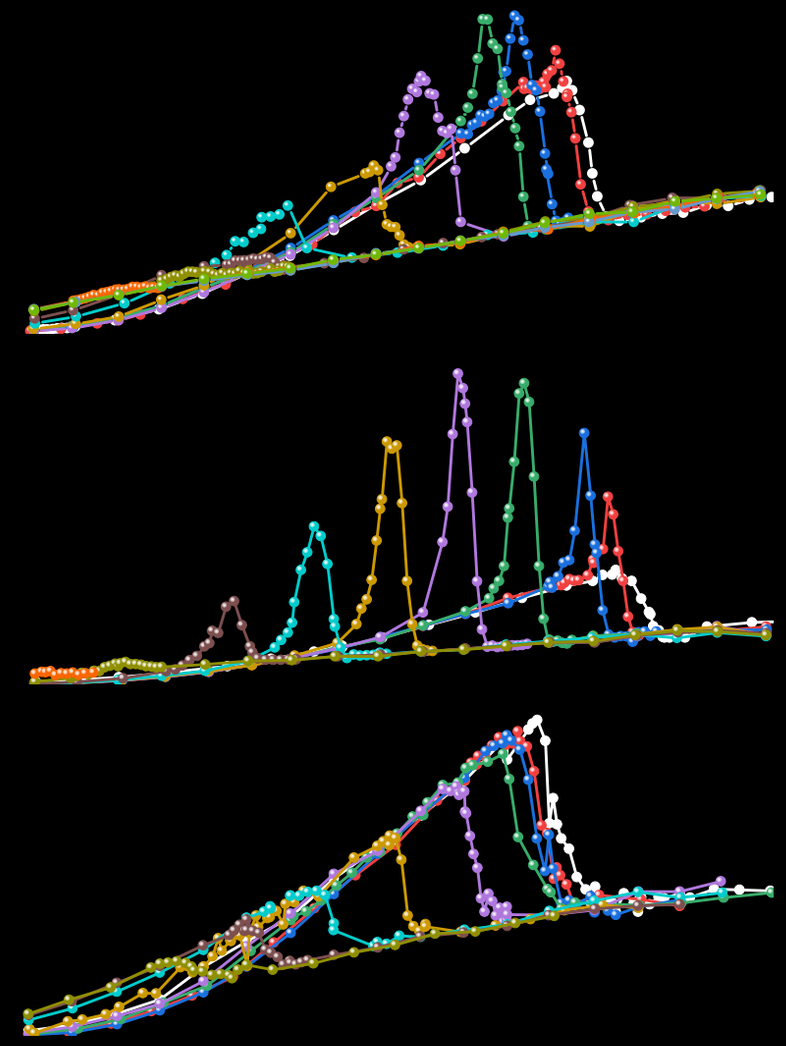

Marc. V. Salis

Experimental Investigation of $PdTe_2$, Doped $PdTe_2$ and $BiCh_2$ Superconductors

ACADEMISCH PROEFSCHRIFT

ter verkrijging van de graad van doctor
aan de Universiteit van Amsterdam
op gezag van de Rector Magnificus
prof. dr. ir. P.P.C.C. Verbeek
ten overstaan van een door het College voor Promoties
ingestelde commissie, in het openbaar te verdedigen in de Agnietenkapel
op woensdag 12 april 2023, te 10.00 uur
door Marc Vincent Salis
geboren te Amsterdam

Promotiecomissie

Promotor:	dr. A de Visser,	Universiteit van Amsterdam
Copromoter:	prof. dr. M. S. Golden,	Universiteit van Amsterdam
Overige leden:	prof. dr. E.H. Brück,	TU Delft
	dr. E van Heumen,	Universiteit van Amsterdam
	prof. dr. A Ohmura,	University of Niigata
	dr. P. P. V. Rodière,	Institut Néel
	prof. dr. P. Schall,	Universiteit van Amsterdam
	dr. J. van Wezel,	Universiteit van Amsterdam

Faculteit der Natuurwetenschappen, Wiskunde en Informatica

Title: Experimental Investigation of $PdTe_2$, Doped $PdTe_2$ and $BiCh_2$ Superconductors
Doctoral Thesis, University of Amsterdam, 2023
Contact: marc_salis@hotmail.nl

The research reported in this dissertation was carried out at the van der Waals-Zeeman Institute for Experimental Physics, University of Amsterdam. The work was financed by the Nederlandse Organisatie voor Wetenschappelijk Onderzoek (NWO) project number 680-91-109.

Contents

Chapter 1

Introduction

Superconductors have garnered great interest since their discovery more than a century ago owing to their exotic properties. A conducting state with zero resistivity that expels all magnetic fields up to a certain temperature and magnetic field is the characteristic description of a superconductor. The understanding of superconductivity gradually formed over the last century with the theoretical crown jewel being the Bardeen-Cooper-Schrieffer (BCS) theory that gives a microscopic description of the underlying electron-phonon coupling that mediates the formation of the macroscopic superconducting condensate in conventional superconductors [1]. Technological applications of superconductivity are widespread, particularly in the form of superconducting magnets which are found in magnetic resonance imaging (MRI) scanners, magnetic levitation (Maglev) trains and various lab equipment. The original hope for superconductivity was to discover superconductors with a transition temperature near room temperature. In the 1980s a milestone in superconductivity research was reached with the discovery of the high temperature superconducting family of cuprates [2]. The significant increase in the maximum transition temperature beyond the 40 K limit of superconductors described by the BCS theory sets the stage for continued exploration of higher temperature superconductors. Next to this, another fundamental cornerstone of superconductivity is the interplay with other material phases, such as ferromagnetism or a charge density wave [3]. It is through the presence of electrons that simultaneously mediate superconductivity and other electronic phases that novel physics arises and the possibility of innovation in the application of superconductivity is bolstered.

A more recent popular field of study in condensed matter physics is the field of topology. Topology finds its origin in mathematics as a concept in morphology. Topology classifies shapes as the same when it is possible to continuously deform one shape into the other. The interest in topological material systems has risen dramatically by virtue of their fascinating elec-

tronic properties. The first topologically non-trivial system to be recognised was the Quantum Hall system in which quantisation of the Hall conductance was observed [4, 5]. This was succeeded by the discovery of the 2D quantum spin Hall effect [6, 7]. The great spark in interest in topology, however, was the extension of the quantum spin Hall effect leading to discovery of topological insulators (TIs) in the 2000s [7, 8, 9, 10]. These topological phases of matter are induced by spin-orbit coupling causing band inversions in materials with a bandgap. This allows for the system to have a nontrivial topological invariant [11]. Systems with topological invariants are usually protected by symmetries such as time-reversal symmetry (TRS) and crystal symmetry leading to the terminology of symmetry-protected topological phases [10]. TIs are distinguished from regular insulators by the band gap structure. A gapped band structure is present in the bulk for both TIs and regular insulators, whereas TIs host gapless 2D surface states. These 2D surface states are Dirac quasiparticles with linear dispersion relations that cross at the Dirac point in the bulk gap, forming a Dirac cone, with the spin locked to the momentum. These properties are exciting in view of possible applications in spintronics [12, 13]. An archetypal TI is Bi_2Se_3 which has been extensively investigated [11, 14].

Other forms of topological phases of matter can, similarly to TIs, appear by band-inversion through strong spin-orbit coupling leading to band crossings with linear dispersions. One such class of systems is presented by the topological semimetals. Two systems within the topological semimetal family are Dirac and Weyl semimetals, named after which equation the topological fermionic quasiparticles obey. In contrast to TIs, the linearly dispersing band crossings in these systems are 3D bulk states [15]. In a Weyl semimetal there are two non-degenerate cones present that give rise to topological Fermi arcs on the surface and chiral magnetic effects in the bulk [16]. The Weyl points are connected by a line forming an open arc, in contrast to the closed loop found in TIs. Either TRS or inversion symmetry (IS) is present for Weyl semimetals providing topological protection [17]. A Dirac semimetal is realised when both TRS and IS are present. Here the two Weyl cones overlap, forming a two-fold degenerate 3D Dirac cone [18]. In general, Dirac semimetal systems lack an additional crystal symmetry on top of TRS and IS to have protection via a topological invariant [19, 20]. Therefore the surface states are unstable in the presence of perturbations and a gap can be formed. Weyl and Dirac semimetals can be further classified in type-I and type-II. This classification distinguishes between two types with a different tilt parameter k of the cones, where $k < 1$ for type-I Weyl/Dirac semimetals and $k > 1$ for type-II Weyl/Dirac semimetals [21]. Weyl/Dirac semimetals with $k > 1$ may have considerably tilted cones such that the one of the linearly dispersive bands runs almost parallel to the Fermi level, thereby greatly increasing the density of states on and near the

Fermi surface.

The combination of topology and superconductivity holds great promise. The quasiparticle excitations in topological superconductors (TSCs) are associated with Majorana bound states [22] that give rise to non-Abelion exchange statistics [23], possibly paving the way for topological quantum computation that is protected from local decoherence [24]. A bulk gap with gapless surface states is present in TSCs. The surface states in this case are Bogoliubov quasiparticles that consist of linear combinations of electrons and hole excitations that obey particle-hole symmetry [25, 26]. Since a Majorana fermion is its own antiparticle, a Majorana state must be an equal superposition of electrons and holes [27]. This, coupled with the topological nature of the particles constituting the excitations, means TSCs present an excellent opportunity to search for Majorana bound states. Experimental confirmation of an actual TSC where the topological surface states enter the superconducting condensate resulting in Majorana bound states is a result that has - as yet - not been achieved in the consensus view of the relevant scientific literature. There are two ways to realise a TSC. The first is to identify a superconductor with topological properties which necessitates unconventional superconductivity [28]. The prime candidate via this avenue is Sr_2RuO_4 although no consensus on its superconducting symmetry has been reached. The second is by inducing superconductivity in a topological system through the proximity effect, pressure or dopants. On the latter route, many candidate TSC materials have been experimentally confirmed, such as the doped 3D TI Bi_2Se_3 family [29, 30, 31], pressure induced superconducting TIs [32, 33, 34] and pressure induced superconducting semimetals [35, 36, 37].

The main focus of the research project that has culminated in this thesis is the candidate topological superconductor $PdTe_2$. The crystal structure is given in figure 1.1. The transition metal dicalchogenide $PdTe_2$ has recently been confirmed to be a type-II Dirac semimetal through ab-initio band structure calculations and angle resolved photoemission spectroscopy [39, 40, 41, 42, 43]. $PdTe_2$ is also confirmed to be a type-I bulk superconductor, also showing nonstandard superconductivity of its (near) surface region [44]. The confirmation of the intrinsic presence of both topology and superconductivity has made $PdTe_2$ a prime candidate TSC. The tilted Dirac cone in $PdTe_2$, as presented in figure 1.2, significantly increases the density of topological Dirac states near the Fermi surface, allowing for an enhanced possibility of topological states to enter the superconducting condensate. Examination of the symmetry of the superconducting state via the penetration depth [45, 46], heat capacity [47, 48] and scanning tunneling microscopy and spectroscopy [43, 49, 50] has uncovered a conventional, weakly-coupled BCS type of superconductivity, indicating no in-gap states. The elusive sur-

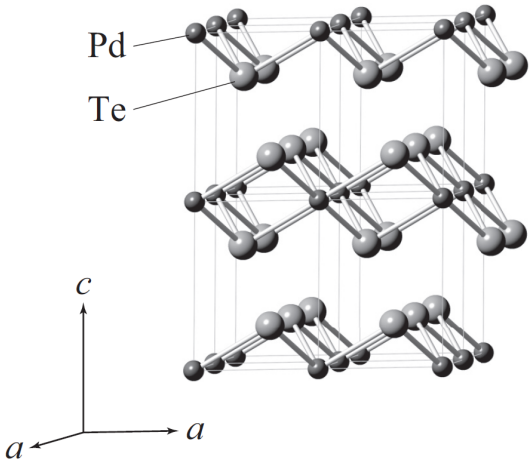

Figure 1.1: Crystal structure of the Dirac semimetal $PdTe_2$ with space group $P\bar{3}m1$. Figure adopted from Ref. [38]

face superconductivity that was observed, however, has been suggested to be influenced by the topological properties in $PdTe_2$ [44]. To further explore the possible effects topology can have on the superconductivity in $PdTe_2$, it is vital to fully understand all aspects of the superconducting state. This has been done in the research presented here by a careful investigation of the heat capacity in $PdTe_2$ as well as by increasing the disorder of the system to induce type-II superconductivity.

The key instrument used to explore the superconducting state of $PdTe_2$ is the in-house heat capacity setup that was built during this research project. Originally the aim of this project was to investigate the candidate TSC $Sr_xBi_2Se_3$ by measuring its heat capacity. Since the discovery of $Sr_xBi_2Se_3$, many reports appeared with promising results that indicated the possibility of topological superconductivity [31, 51, 52, 53]. The aim was to measure the heat capacity of the superconducting state for different orientations of the magnetic field in view of the rotational symmetry breaking present in the system [54]. Since the heat capacity is a probe of all elementary degrees of freedom in a solid and thus a direct measure of the density of states, it lends itself excellently as a tool to explore the properties of candidate TSCs. The ability to probe the density of states is essential in identifying TSCs for which the presence of in gap states is predicted. Unfortunately, to properly measure the heat capacity of the superconducting state of $Sr_xBi_2Se_3$ the precision of a nanocalorimeter is required because of the unusually small Sommerfeld coefficient of order 0.1 mJ/mol K^2 [55]. This precision could not be achieved in our setup, mainly due to an insufficient temperature stability in the heat capacity instrument.

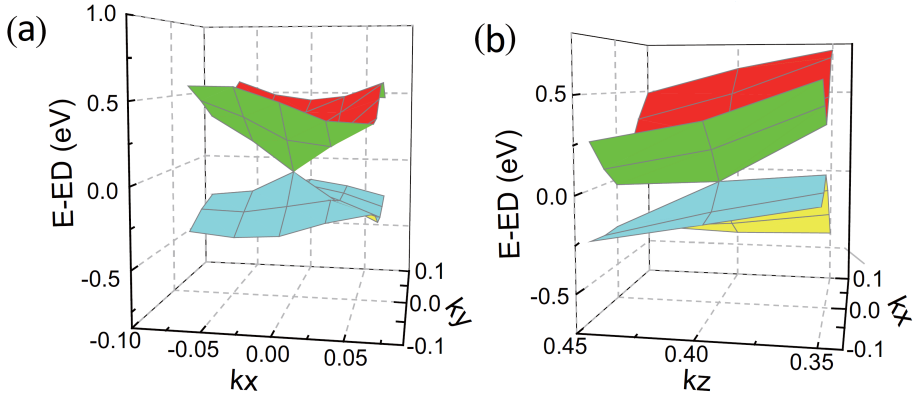

Figure 1.2: Depiction of the calculated type-II Dirac cone of $PdTe_2$ where E_D is the energy of the Dirac point. The tilt is present along k_z. The projection is on k_x and k_y as well as k_z and k_x for (a) and (b), respectively. Figure adopted from Ref. [41].

The outline of this thesis is as follows: In Chapter 2 an overview of the experimental setups employed in this study is given. In Chapter 3 the theoretical background relevant to this study is reviewed. In Chapter 4 the results of the heat capacity study on superconductivity in $PdTe_2$ are presented. In Chapter 5 the findings of the investigation of the effects on superconductivity of iso-electronic substitution of Pt for Pd in $PdTe_2$ are discussed. In Chapter 6 the results of the angle-dependent magnetotransport study of $LaO_{0.8}F_{0.2}BiS_{2-x}Se_x$ ($x = 0.5$ and 1.0) are given. In Chapter 7 the details of a high pressure study of PdTe2 are reported. This thesis is concluded with a summary and acknowledgements.

Chapter 2

Experimental aspects

In this chapter the relevant experimental details are presented. A short review on the cryogenic Oxford Instruments Heliox system is given. Next the heat capacity setup and the relevant ways to operate it are discussed. This is followed by a description of the thermometry. The ac susceptibility setup, rotator cell and pressure cell are introduced in the final part of this chapter.

2.1 Cryogenics

All the calorimetry data below 2 K reported in this thesis have been acquired using a relaxation method in a heat capacity setup placed inside an Oxford Instruments Heliox system. The Heliox system is comprised of a single-shot sorption pump ^{3}He insert and a cryogenic liquid ^{4}He bath dewar. In the dewar a superconducting magnet with a maximum operating field of 14 T is situated. The helium bath is surrounded by a vacuum space and a liquid nitrogen shield to reduce the heat input of the room temperature surroundings. The insert consists of a large inner vacuum chamber in which a ^{3}He pot, 1K pot, sample stage and a sorption pump are situated. Low-temperatures are reached as follows. Firstly, a constant flow of liquid ^{4}He is pumped through the 1K pot, which is kept at its base temperature of 1.5 K. At this stage the sorption pump is at the same temperature and keeps the ^{3}He gas absorbed. Next, by heating the sorption pump to 30 K, the ^{3}He gas is released and it condenses at the 1K pot stage, and is collected in the ^{3}He pot. In the following step, the heating of the sorption pump is stopped, and it cools down to $\sim$ 1.5 K. This results in a reabsorption of the ^{3}He gas and a lowering of the vapour pressure in the ^{3}He pot. In this manner a base temperature of 0.3 K can be achieved at the sample stage, which is thermally connected to the ^{3}He pot.

2.2 Heat capacity setup

The heat capacity setup that has been used in this project was mainly designed to carry out relaxation calorimetry measurements. The system can also function for ac calorimetry. The setup is given schematically in figure 2.1. Typically, the module consists of a platform on which a thermometer, heater and sample are located. The platform is connected via a good thermal link to a copper frame, which acts as the cryogenic bath and can be kept at a stable temperature. For the heat capacity cell we have opted to use a Quantum Design ^{3}He heat capacity puck which was further modified for use in the Heliox system. This cell consists of a sapphire sample platform of 3×3 mm^2 with additional gold sputtered contact pads for the electrical connection from the Au-Pd wires to the heater (RT 100 Ω) and thermometer (Cernox^{TM}-1020, RT 1.43 kΩ), see figures 2.2 and 2.3. Here RT means room temperature. Four wires are present to connect the sample platform to the frame both mechanically and thermally. The sample is attached to the platform with Apiezon N vacuum grease during measurements. Radiation from the 4.2 K environment to the cell is reduced by a radiation shield as shown in figure 2.4. The heat capacity puck is attached to an oxygen free high conductivity (OFHC) copper rod that in turn is in thermal contact with the low eddy current sample holder attached to the ^{3}He pot. In this

manner a good thermal link between the sample platform and the ^{3}He pot is achieved. On the OFHC copper rod a thermometer (Dale RuO_2, RT 5.2 kΩ) and heater (RT 100 Ω) have been placed, as shown in figure 2.4. Further temperature control for a stable bath temperature was achieved by the extra thermometer and heater on the sample rod. The control of the temperature on the sample rod was carried out with a Lakeshore 370 resistance bridge with PID temperature control.

To measure the heat input at the sample stage a Keithley 6221 current source with a Keithley 2182A nanovoltmeter are employed to supply a known current and measure the voltage, respectively. The resistance of the thermometer is recorded using a SR865 lock-in amplifier. Computer control of the setup is carried out using Labview. In the calorimetry setup the magnetic field is oriented vertically, *i.e.,* in the plane of the crystals attached to the sapphire sample platform. Regular sample sizes range from (height $\times$ width $\times$ length) 0.1×2.0×2.0 mm^3 to 0.3×3.0×3.0 mm^3. Regular sample masses range from 1 mg to 50 mg.

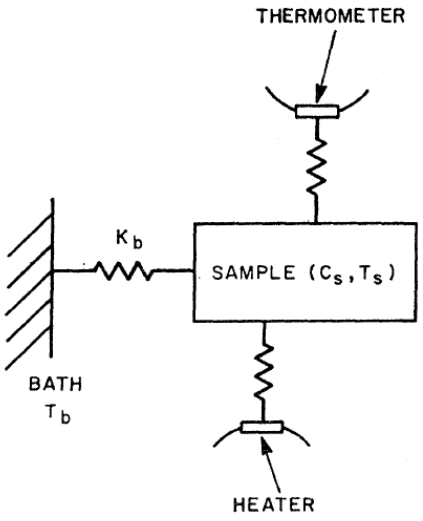

Figure 2.1: Schematic of the experimental setup in relaxation calorimetry. The sample platform is thermally connected with a thermal conductance κ_b to a bath to assume a stable temperature T_b. Passing a current through the heater allows for the temperature T_s of the sample to increase. The thermometer senses the increase in temperature of the sample and is used to record the changes in temperature during the measurements. Figure adopted from [56].

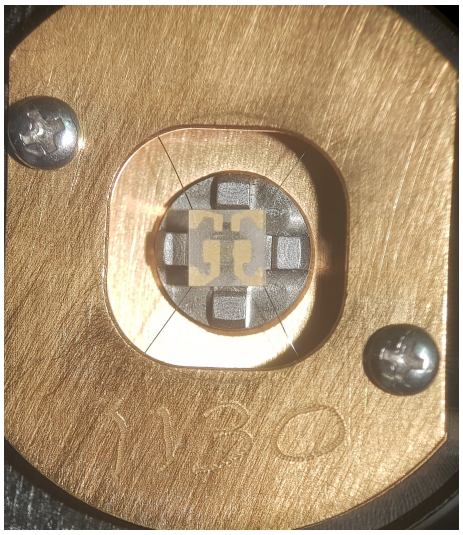

Figure 2.2: Photograph of the Quantum Design ^{3}He heat capacity puck. The sample platform is held suspended by four Au-Pd 50 micron wires which also function as the electrical wiring for the heater and thermometer. The heater and thermometer are situated on the underside of the platform. The gold sputtered areas allow for electrical connection between measuring equipment and the heater and thermometer.

2.2.1 Adiabatic calorimetry

The most basic technique in low-temperature calorimetry is adiabatic calorimetry, first introduced by Nernst [57] and Eucken [58] at the start of the 20$^{\text{th}}$ century, and was widely used for over 50 years. The principle of measurement is directly based on the definition of the heat capacity:

$$C = \lim_{\Delta T \to 0} \frac{\Delta Q}{\Delta T}, \tag{2.1}$$

where ΔQ is the heat input necessary to increase the temperature T by ΔT. A typical adiabatic calorimetry setup consists of a vacuum chamber immersed in liquid helium. Inside the chamber the sample is mounted with the thermometer attached, as well as a heater of high resistance wrapped around the sample. To reach thermal equilibrium a valve is used to allow helium exchange gas enter the chamber, after which vacuum is regained. A current is then applied to the heater and the subsequent change in temperature is recorded. For this measurement to be effective, only the known amount of heat ΔQ must be applied to the sample when recording the change in temperature. Therefore, thermal isolation is a stringent requirement. This technique has several shortcomings. The first is the necessity of efficient thermal isolation limiting the range of temperatures in both the high and low regimes due to radiation and heat leaks, respectively. Heat

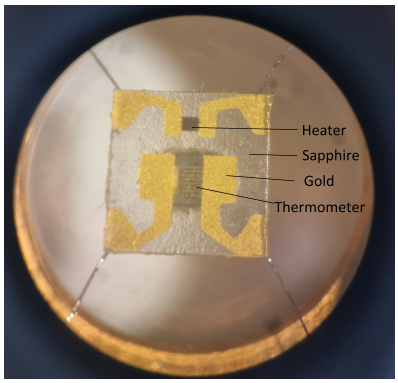

(a) Sample platform topside.

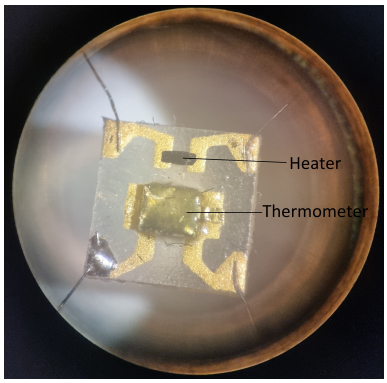

(b) Sample platform underside.

Figure 2.3: Photographs of the Quantum Design ^{3}He heat capacity puck sample platform. (a) The topside of the sapphire sample platform with the gold sputtered pads, thermometer and heater indicated. (b) The underside of the sample platform with the heater and thermometer indicated. A (tin solder) repair connecting a Au-Pd wire to the sample platform is visible in the lower left corner.

leaks also limit the minimum sizes of samples that can be measured. The second drawback is the lack of sensitivity when measuring samples of small sizes and small heat capacities. The third disadvantage is the comparatively slow measurement process. To mediate these issues new low-temperature calorimetry techniques have been designed. Specifically looking at newer instruments capable of noise reduction at high speed data acquisition, one promptly arrives at the use of high speed ac resistance bridges and lock-in amplifiers starting in the 1960s.

2.2.2 Relaxation calorimetry

One way to further increase the sensitivity in heat capacity measurements is by addressing the temporal aspect. To accomplish this, Bachman *et al.* [59] extended heat capacity measurements taking the relaxation time needed to return to thermal equilibrium into account with $\tau = C/\kappa$, where τ is the relaxation time constant, C the heat capacity and κ the thermal conductivity between sample and bath, see figure 2.1. The heat equation can be written as follows [59]

$$C(T) = \left(\frac{dT}{dt}\right)\left[P - \int_{T_0}^{T_1} \kappa(T')dT'\right]. \tag{2.2}$$

Here P is the power put into heating the system, T_0 the starting temperature equal to the temperature of the bath and T_1 the increased temperature reached by heating the sample. For a change in temperature $\Delta T = T_1 - T_0$ that is small enough *i.e.*, $\Delta T/T_b < 0.01$ (where T_b is the stable temperature

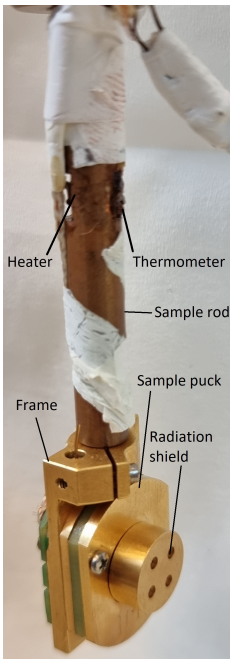

Figure 2.4: Photograph of the heat capacity cell connected to the OFHC copper sample rod. Indicated are the sample rod, sample rod thermometer, sample rod heater, frame, sample puck and radation shield. The Quantum Design ^{3}He heat capacity puck is connected to the bottom of the sample rod using the frame.

of the bath), this equation leads to

$$C = \frac{\kappa(T_{av})}{d(\ln\Delta T)/dT}, \tag{2.3}$$

with T_{av} the average temperature and where

$$\frac{d\ln\Delta T}{dT} = \frac{1}{\tau} = \frac{C}{\kappa}. \tag{2.4}$$

Thus by measuring the relaxation of the temperature one can determine the heat capacity C, given that $\kappa = \Delta T/P$, with ΔT and P being known quantities.

In the thermal relaxation method the sample temperature is kept stable at a temperature T_0. By passing a current through the heater, a known power P is dissipated to the sample platform to heat the sample to a temperature $T_0 + \Delta T$, where $\Delta T = P_0/\kappa$ with κ the thermal conductance of the sample platform to the bath, κ_b in figure 2.1. This is followed by the removal of the current at $t = t_0$ and the accompanying heat relaxation at $t > t_0$.

The sample temperature returns to the stable temperature T_0. This process is schematically presented in figure 2.5. During this process the current I and voltage V over the heater, as well as the sample temperature T, are recorded versus time. Solving equation 2.3 for both heating regimes leads to

$$\begin{aligned} t < t_0 : \; T &= T_b + \Delta T\big(1 - e^{-t/\tau}\big), \\ t > t_0 : \; T &= T_b + \Delta T\big(1 - e^{-t_0/\tau}\big)e^{-(t-t_0)/\tau}. \end{aligned} \tag{2.5}$$

Here T_b is the bath temperature. A caveat of using this technique is its

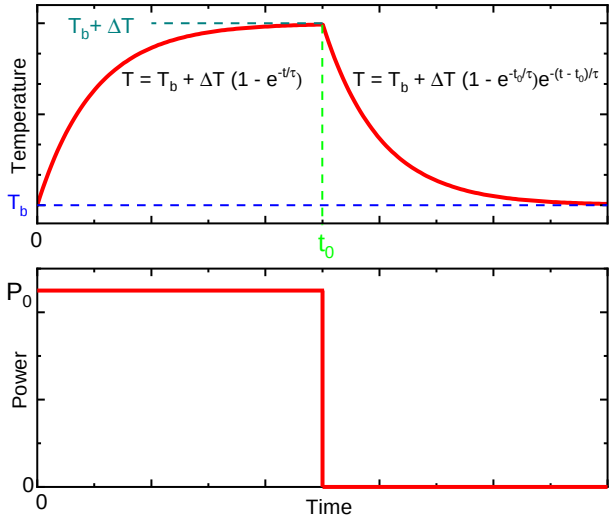

Figure 2.5: Schematic of dual slope relaxation calorimetry. A heat pulse (bottom) with power P_0 is applied between $t = 0$ and $t = t_0$ resulting in a temperature change of T_b to $T_b + \Delta T$ (top). At t_0 the heat pulse is removed and thermal relaxation takes place.

inability to capture large changes in the heat capacity over a small temperature range, as is the case - for instance - at a first-order phase transition where latent heat is present. It is furthermore paramount that κ remains relatively constant. Only then can $\tau = C/\kappa$ be analyzed effectively. The bottleneck of the technique is the ratio of τ between the sample and the bath to other time constants in the system. If the relaxation time between the sample and the sample platform, known as τ_2, is of a similar order as τ, equation 2.5 is no longer valid. This is known as a τ_2 effect and usually shows up as a flat structure in the relaxation curves. This can be analysed properly by adding an extra term in equation 2.5 accounting for this second relaxation process.

2.2.3 Ac calorimetry

To mediate the issues in measuring large changes in the heat capacity over small temperature ranges one can make use of signal averaging instruments to measure the heat capacity relatively. This technique which is now known as ac calorimetry was first introduced by Sullivan *et al.* [56]. Here a steady state calorimetric measurement is achieved by connecting an ac heat supply to the sample, which leads to a constant change in temperature with a dc and an ac part. For a current applied to the heater in the form of $I = I_0\cos(\omega t/2)$ with ω the frequency of the ac current and I_0 the amplitude, it can be shown that [56]

$$T_{ac} = \frac{Q_0}{2\omega C}\left[1 + \frac{1}{\omega^2\tau_1^2} + \omega^2\tau_2^2 + \frac{2K_b}{3K_s}\right], \tag{2.6}$$

where T_{ac} is the amplitude of the oscillating temperature due to the heater input *i.e.*, $T = T_b + T_{ac}$, Q_0 the heat input related to I_0, τ_1 the sample to bath relaxation time, τ_2 an umbrella term for all other relaxation time constants, K_b the sample to bath thermal conductance and K_s the thermal conductance of the sample. A schematic of the measured signal is given in figure 2.6. The term outside the brackets in equation 2.6 describes the amplitude of the oscillating temperature, whereas the last three terms inside the brackets describe corrections to this amplitude. The second term corrects for thermal damping of the sample not reaching equilibrium fast enough at high frequencies. The third term describes the heat flow between the sample and the thermometer and heater, in which equilibrium is reached too fast if the applied frequencies are too low. The last term describes a correction to the amplitude should the thermal conductance of the sample be of similar size to that of the thermal to bath thermal conductance. The last term is rarely non-negligible in actual measurements. The second and third terms are usually small due to the regime in which the equation is valid. Firstly. the heat capacities of the sample platform, heater and thermometer are much less than that of the sample. Secondly, the sample, thermometer and heater should reach thermal equilibrium with a time constant much less than the inverse of the frequency. Thirdly, the sample to bath relaxation time should be smaller than the inverse of the frequency. Denoted in another way for these three conditions:

$$\tau_1^2 >> \omega^2 >> \tau_2^2,\ C_{sample} >> C_{heater}, C_{thermometer}. \tag{2.7}$$

2.3 Thermometry

Temperature sensors are pivotal in calorimetry. By accurately recording the changes in the temperature, the heat capacity can be determined. However, a small amount of noise can readily render the recorded data useless. Therefore, it is imperative to work with thermometers with high sensitivity in the

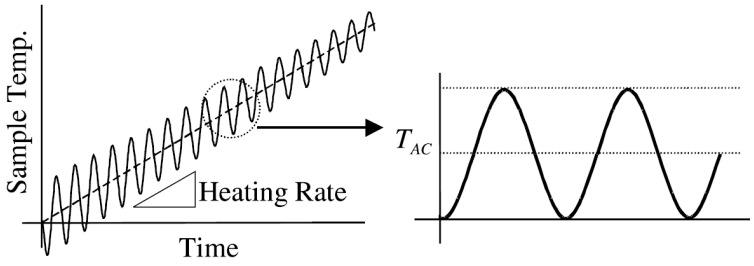

Figure 2.6: Schematic of the heating process of ac calorimetry. Figure adopted from [60].

desired temperature range. Several calibrations of the thermometers used in the set-up have been carried out. In every calibration step, the thermometers were calibrated using a previously calibrated thermometer. The sample rod (frame) thermometer was calibrated using a commercially calibrated RuO_2 thermometer from Lakeshore with serial number M207 and room temperature resistance of 2.2 kΩ. The platform thermometer was in turn calibrated against the sample rod thermometer. To calibrate the thermometers, the resistance and corresponding temperature values were recorded over a 30 second period at stable temperatures. This process has been carried out for many temperatures and the data are presented in figures 2.7a and 2.7b. The relation between the temperature and the resistance of the Lakeshore RuO_2 thermometer takes the form of Chebyshev polynomials for different temperature ranges given by

$$T = \sum_{i=0}^{n} A_i \cos\big(i \arccos\big(X\big)\big), \tag{2.8}$$

where T is the temperature, A_i are determined coefficients and

$$X = \frac{[\log(R) - \log(R_l)] - [\log(R_h) - \log(R)]}{\log(R_h) - \log(R_l)}. \tag{2.9}$$

Here R is the resistance and R_l and R_h are the lower and upper limits of the resistance in a specific temperature range. A small discrepancy between fitted regions is (always) present, which can be reflected in further calibrations. To minimise this effect, there has been made use of different temperature ranges as well as two different fitting functions. One is based on the variable range hopping model by Mott [61]

$$T = T_0 \ln((R + a)/R_0)^{-1/\alpha}, \tag{2.10}$$

where T_0 and R_0 are characteristic constants, α a coefficient describing the dimensionality of the system and a an added fitting parameter. The other

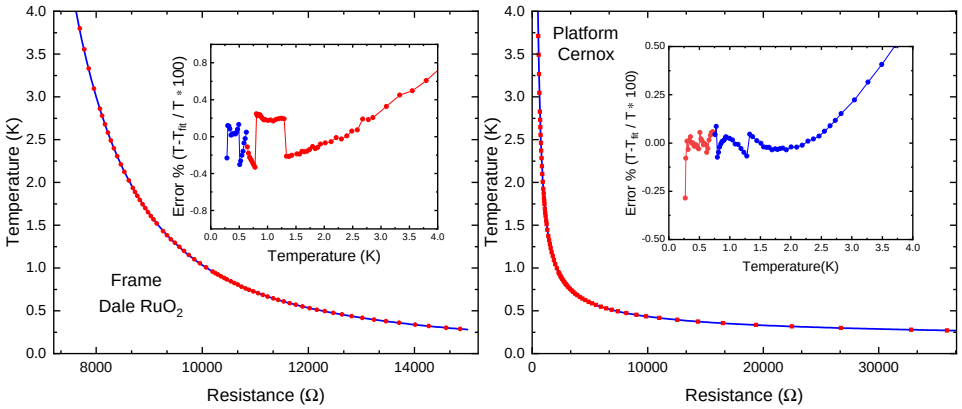

(a) Resistance curve of the thermometer used on the sample rod.

(b) Resistance curve of the thermometer used on the sample platform.

Figure 2.7: Resistance curves against temperatures for the two thermometers used in the experiments. Both figures are given in the temperature range of 0 to 4.0 K in which all measurements have been carried out. The insets show the error percentage on the fitted lines to the data points. The red (blue) color denotes that the fit used is equation 2.10 (2.11). The structure seen in both insets around 1.0 K is due to a change in temperature range fit of the commercially calibrated thermometer.

is a function found through trial and error that effectively captures the temperature-resistance dependence:

$$T = A \exp\left[(B \ln((R + C))^D\right], \tag{2.11}$$

where A, B, C, D are fitting parameters. Allowing the use of both equations for the fitting procedures produces the most reliable R to T curves for the thermometers. Figures 2.7a and 2.7b present the results of the fitting functions for the sample rod thermometer and the platform thermometer, respectively. The insets of these figures show the error percentage of the fits with respect to the measured values. Evident is that the error percentage of the fitting function stays within 0.4% up to 3.0 K for the sample rod thermometer whereas the error percentage of the fitting function for the platform thermometer stays within 0.25%. The structures seen in both insets around 1.0 K, a sharp increase below 1.0 K for figure 2.7a, is due to the transition between fits in that temperature range. This switch in fit present for the sample rod thermometer used on the OFHC copper rod was carried over from the commercial calibrated thermometer. Do note however that these changes are small enough to not influence the measurements to a degree that they are either noticeable or give faulty results.

2.4 Ac susceptibility

Ac susceptibility measurements were carried out with an in-house cell specifically designed for use in the Heliox system that is based on the mutual inductance transformer method [62]. The setup consists of one primary coil and two identical oppositely wound coaxial secondary coils which are connected in series and vertically separated. During the measurement the sample is situated in one of the secondary coils. A small sinusoidal current is passed through the primary coil generating an oscillating magnetic field known as the driving field. The driving field induces an oscillating magnetisation in the sample which in turn induces a voltage in the secondary coils. In the absence of a sample the induced voltage should equal zero. Experimentally a small voltage still remains due to the secondary coils not being exactly compensated. The induced voltage is the measured signal in this experiment, which can be related to the differential susceptibility χ. The measured signal is given in arbitrary units. This can be calibrated with a sample with a known absolute ac susceptibility. The temperature is measured with the RuO_2 M207 thermometer that is attached to the cell. The voltage is read out with the Linear Research 700 ac resistance bridge with a frequency of ~ 14 Hz and a driving current of $\sim 30 - 300\mu$A, which results in fields of $\sim 0.0078 - 0.078$ mT.

2.5 Rotator

In order to measure the angle dependence of the magnetoresistance we have opted to use a rotator in our experiments that is capable of *in-situ* rotation in the croystat at low temperatures. In order for this to work, the rotator should have a low heat-input during operation. To achieve this we have made use of the Attocube ANRv51 RES stepper-motor. This piezo-element rotator works as follows. The stepper motor consists of the main body, the actuator and the internal weight. The actuator is capable of expansion and contraction by virtue of the piezo-element present. When performing a rapid expansion or contraction, the main body is displaced in a fashion that overcomes static friction. In a slow contraction, the static friction can exceed the inertial force so that the main body maintains its position. Repeated use of these two movements allows for the motion of the stepper motor [63]. The motion is controlled by the ANC350 motion controller. To accurately read out the angle of the rotator a resistive sensor is used. This sensor has been calibrated at room temperature by Attocube. A low-temperature calibration at 0.7 K has also been carried out previously using a Hall sensor for greater precision [64]. However, the positioner used has a large negative temperature coefficient at very low temperatures making either calibration unreliable when carrying out measurements at various temperatures below

5 K. An example of this phenomenon is illustrated in figure 2.8 where the angle readout values at different temperatures below 5 K are given. During the acquisition of the data the cell was at a constant physical angle *i.e.*, the system did not perform any rotation. To mediate the unreliability of the angle data the following procedure is carried out for each sample: The system rotates to an unknown angle of which the readout value at base temperature is recorded. The acquired data is compared to a set of data acquired by a different rotator setup and the readout angle value is adjusted to the real physical angle according to the corresponding data-set of the other rotator setup.

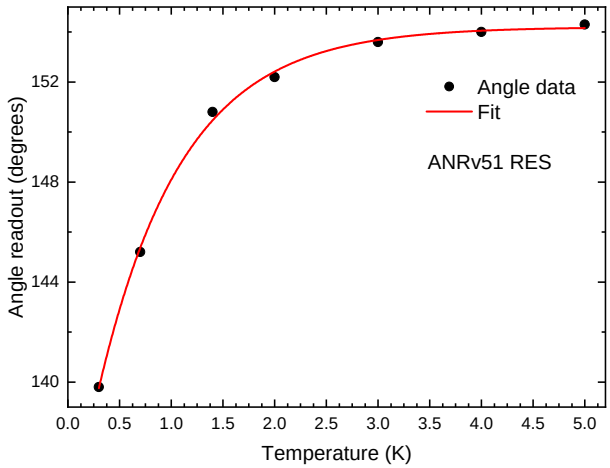

Figure 2.8: Low-temperature data of the temperature dependence of the angle readout value given by the positioner of the rotator. All data points are taken at one physical angle. The data points are given as black circles and the red line is a fit to the data.

2.6 Pressure cell

Resistivity measurements at low temperatures under high pressure were carried out by use of a Cu-Be modified Bridgman anvil cell in the Heliox system [65, 66]. The cell consists of Tungsten Carbide (WC) anvils placed inside a brass guide tube insulated by a Teflon sheet, as illustrated in figure 2.9. The anvils are situated between a WC piston and a CuBe lower plug. A CuBe clamp nut above the WC piston is used to clamp the load onto the piston. The pressure in the cell is generated by use of a hand press (Laboratory Hydraulic Press: LCP20 Unipress) on the piston. The piston, brass guide and lower plug are surrounded by a CuBe body to minimize transversal expansion of the apparatus due to applied pressure. The electrical wiring is introduced to the cell via holes in the lower CuBe plug which allows for four-

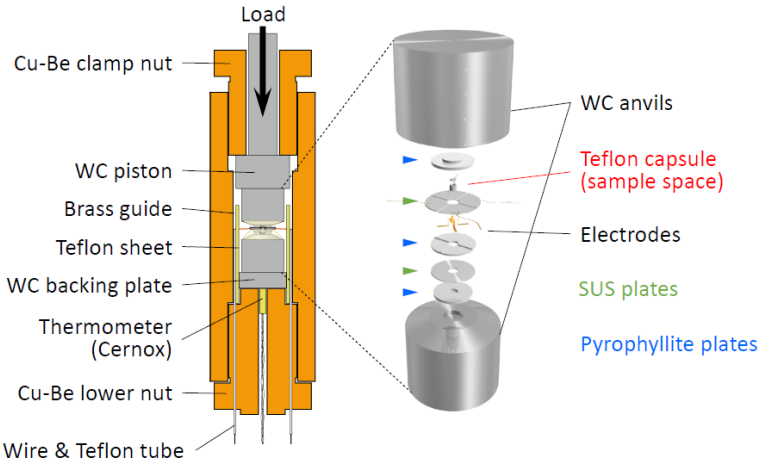

Figure 2.9: Schematic diagram of the modified Bridgman anvil cell used in the Heliox system. On the left side the main body of the cell with its constituents are presented. The right side depicts a zoom of the parts between the Tungsten Carbide anvils. SUS plates mean stainless steel. The diagram is provided by Dr. A. Ohmura (of Niigata University).

terminal measurements. The sample is placed in a Teflon capsule along with a mixture of Flourinert (FC70:FC77 = 1:1), which is a pressure-transmitting medium used for quasihydrostatic compression. Only one sample is placed inside the capsule during measurements. Gold wires connected from the sample to gold foil placed on the Teflon capsule is used for the electrical connection. Stainless steel plates are electrically connected to the gold foil to carry the electrical signal to the outer wiring. Pyrophillite plates surround the stainless steel plates on the bottom and top. The pressure inside the capsule against the load was previously calibrated as a function of the critical pressures of the structural phase transitions of elemental Bismuth (purity 5N) [38, 67]. Typical sample sizes are $\approx 0.3 \times 0.7 \times 0.1$ mm^3 (width $\times$ length $\times$ height). Measurements were carried out in the Heliox system down to ≈ 0.3 K.

Chapter 3

Background theory

In this chapter, the theoretical background is reviewed. First the relevant concepts of heat capacity are treated. This is followed by the necessary components to distinguish between type-I and type-II superconductivity. Next the characteristic behaviour in field of type-I and type-II superconductors is discussed. Second to last is a brief treatment of the Bardeen-Cooper-Schrieffer theory. The chapter ends with a description of the low temperature behaviour of the superconducting state and the heat capacity.

3.1 Heat capacity

The heat capacity is defined as the amount of energy that is necessary to raise the temperature by one degree of a substance with a defined quantity of mass

$$C = \lim_{\Delta T \to 0} \frac{\Delta Q}{\Delta T}, \tag{3.1}$$

where C is the heat capacity and ΔQ is the heat put into the system to raise the temperature by ΔT. The heat capacity generally depends on the temperature of the system, the volume and the pressure. To further introduce basic relations that will be used later on, a short treatment of the thermodynamic identities that govern these processes will be given. From the first law of thermodynamics one obtains

$$dQ = dU - dW, \tag{3.2}$$

where U is the internal energy and W the work done. The heat change is

$$dQ = TdS, \tag{3.3}$$

where dS is the change in entropy. If the work done only allows for a change in volume then

$$dW = PdV, \tag{3.4}$$

where P is the pressure of the system and V the volume. From this it follows that

$$dU = TdS - PdV. \tag{3.5}$$

Then, the heat capacity can be written as

$$C_v = \left(\frac{dQ}{dT}\right)_v = T\left(\frac{dS}{dT}\right)_v, \text{ and } C_p = \left(\frac{dQ}{dT}\right)_p = T\left(\frac{dS}{dT}\right)_p. \tag{3.6}$$

Here the subscripts denote which quantity is held constant *i.e,* C_v and C_p denote the heat capacity at constant volume and constant pressure, respectively. Writing for the change in entropy

$$dS = \left(\frac{dS}{dT}\right)_T dT + \left(\frac{dS}{dP}\right)_T dP, \tag{3.7}$$

then, taking the temperature derivative

$$\left(\frac{dS}{dT}\right)_v = \left(\frac{dS}{dT}\right)_p + \left(\frac{dS}{dP}\right)_T \left(\frac{dP}{dT}\right)_v. \tag{3.8}$$

Now, applying the definitions of C_p and C_v to get

$$C_v = C_p + T\left(\frac{dS}{dP}\right)_T \left(\frac{dP}{dT}\right)_v, \tag{3.9}$$

one can then use the Maxwell relation

$$\left(\frac{dS}{dP}\right)_T = -\left(\frac{dV}{dT}\right)_p, \tag{3.10}$$

to write

$$C_p - C_v = T\left(\frac{dV}{dT}\right)_p \left(\frac{dP}{dT}\right)_v = \frac{\alpha^2 T}{\rho \beta_T}. \tag{3.11}$$

Here α is the thermal expansion coefficient, ρ the density and β_T the compressibility. Equation 3.11 describes the difference between C_v and C_p in terms that are experimentally known. It is notable that all four of the above terms on the right hand side are usually negligibly small at low temperatures (few materials have a large α). Furthermore, experimentally one measures C_p, because the experiment is always kept at a constant pressure in a vacuum. Therefore, C_v and C_p are interchangeable to experimental precision. Beyond this sub-chapter the heat capacity will be expressed as C with subscripts relating to terms other than volume or pressure. Last to be introduced is the relation between the heat capacity and the Gibbs free energy, F:

$$dF = VdP - SdT \tag{3.12}$$

using equation 3.6 at constant volume and taking the temperature derivative one obtains

$$C = \left(\frac{d^2F}{dT^2}\right)_v = -T\left(\frac{dS}{dT}\right)_v. \tag{3.13}$$

3.1.1 Debye lattice heat capacity

In the description of the lattice contribution to the heat capacity of metals at very low temperatures a $\beta_3 T^3$ term is usually sufficient. The derivation of this term is readily given using the Debye model. Debye constructed this model following the Einstein model [68], which succeeded in giving a quantum mechanical derivation of the Dulong-Petit law $C = 3SR$, where S is the number of atoms per formula unit of a given substance and R is the gas constant per mole formula unit. However, this model failed to accurately capture the low-temperature behaviour of the heat capacity due to the assumption of just one occupied phonon frequency. Debye expanded upon this model by allowing for the solid to be an isotropic elastic medium in which only acoustic phonons are taken into account [69], eliminating the single frequency assumption from the Einstein model. Through this the Debye model accurately predicts C at very low and very high temperatures, but fails at intermediate temperatures. In the Debye model the angular phonon frequency ω is related to the wave vector k and wave velocity v by

$$\omega = kv, \tag{3.14}$$

where the wave velocity is taken constant. Solving the wave equation for a simple solid with volume V, the number of available states n is

$$n = \frac{V}{2\pi^2}k^2 dk. \tag{3.15}$$

The density of phonon modes $D(\omega)$ can then be written as

$$D(\omega) = \frac{dn}{d\omega} = \frac{V\omega^2}{2\pi^2 v^3}. \tag{3.16}$$

The average total vibrational thermal energy U follows in the form

$$U = 3\int_0^{\omega_D} D(\omega)\left(\frac{1}{exp(\hbar\omega/k_b T) - 1} + \frac{1}{2}\right)\hbar\omega d\omega, \tag{3.17}$$

where $\hbar$ is the reduced Planck constant, k_B the Boltzmann constant and ω_D the Debye frequency which is a cutoff frequency added to account for the finite amount of phonon modes, $3N$, present. This expression can be rewritten with $x = \hbar\omega/k_B T$ to

$$U = U_0 + \frac{3V(k_B T)^4}{2\pi^2 v^3 \hbar^3}\int_0^{X_D} \frac{x^3}{e^x - 1}dx. \tag{3.18}$$

where $U_0 = 3\hbar V\omega_D^4/16\pi^2 v^3$ is the zero point energy. Introducing the Debye temperature $\Theta_D = \hbar\omega_D/k_B$ and taking the temperature derivative to obtain the heat capacity $C = dU/dT$:

$$C = 9SR\left(\frac{T}{\Theta_D}\right)^3 \int_0^{\Theta_D/T} \frac{x^4 e^x}{[e^x - 1]^2}dx, \tag{3.19}$$

where S is the number of atoms per formula unit. The integral part is regularly written as $D(\Theta_D/T)$ and is called the Debye function. In the low-temperature limit of $T << \Theta_D$ the upper limit of the integral can be increased to infinity with little sacrifice to accuracy and reduces to

$$C = \frac{12\pi^4}{5}SR\left(\frac{T}{\Theta_D}\right)^3 = \beta_3 T^3 \ (T << \Theta_D). \tag{3.20}$$

The β_3 here is commonly found in the scientific literature and denotes the phonon contribution factor ($\beta_3 T^3$ being the phononic contribution) to the heat capacity. It has been empirically shown that the T^3 dependence is universally observed for temperatures up to $\Theta_D/50$ [70]. At intermediate temperatures the Debye model fails to accurately predict the behaviour due to the ω^2 dependence in the phonon density of states. At higher temperatures $T >> \Theta_D$ the model succeeds in retrieving the Dulong-Petit law as the integral reduces to an expansion in which the first term cancels out the $(T/\Theta_D)^3$ term, giving $C = 3SR$.

3.1.2 Electronic heat capacity

The electronic heat capacity at low temperatures in metals is generally described quite simply in the literature. The derivation is straightforward and given in most introductory textbooks on condensed matter physics [71, 72]. Since electrons are fermions, they must obey the Fermi-Dirac distribution function:

$$f(\epsilon) = \frac{1}{e^{(\epsilon-\mu)/k_B T} + 1}, \tag{3.21}$$

where ϵ is the electron energy level and μ the chemical potential. With $\eta(\epsilon)$ the electron density of states, this allows one to write for the total number of electrons N_e in the system

$$N_e = \int_0^\infty f(\epsilon)\eta(\epsilon)d\epsilon, \tag{3.22}$$

The average energy of N_e electrons at a given temperature follows as

$$E = \int_0^\infty \epsilon f(\epsilon)\eta(\epsilon)d\epsilon. \tag{3.23}$$

By taking the temperature derivative one attains the heat capacity

$$C_e = \int_0^\infty (\epsilon - \mu)\frac{df(\epsilon)}{dT}\eta(\epsilon)d\epsilon. \tag{3.24}$$

Applying the Sommerfeld expansion, the integral at low temperatures leads to [71]

$$C_e = \frac{1}{3}\pi^2 k_B^2 \eta(\epsilon_f)T = \gamma T, \tag{3.25}$$

where ϵ_f is the Fermi level and γ is the Sommerfeld coefficient. It is immediately evident that only electrons near ϵ_f contribute to the heat capacity. While this result is only valid for a free electron gas, it is sufficient to capture the typical contribution of electrons to the heat capacity in metals at very low temperatures.

3.1.3 Phase transitions

Another important aspect of heat capacity is its behaviour at a phase transition. Phase transitions can be classified into two categories. In first-order phase transitions a discontinuity in the entropy is present. Phase transitions where the entropy remains continuous throughout the transition are known as second-order phase transitions or continuous phase transitions. Consider a first-order phase transition where the two phases α and β are in thermal equilibrium. Then, using the Gibbs free energy such that $G_\alpha = G_\beta$, where the volume of the system is constant during the transition, the Clausius-Clapeyron equation can be derived as.

$$dG_\alpha = dG_\beta = (VdP)_\alpha - (SdT)_\alpha = (VdP)_\beta - (SdT)_\beta, \tag{3.26}$$

$$dT(S_\alpha - S_\beta) = dP(V_\alpha - V_\beta), \tag{3.27}$$

$$\Delta S = \frac{L(T)}{T} = \Delta V \frac{dP}{dT}. \tag{3.28}$$

Here $L(T)$ is the latent heat which is the additional heat gained or lost by the system during a first-order phase transition. Similarly for a magnetic transition where there is no change in volume or pressure:

$$dG = -SdT - \mu_0 M \cdot dH, \tag{3.29}$$

$$\Delta S = \Delta M \frac{dH}{dT}, \tag{3.30}$$

where M is the magnetisation and H the applied magnetic field. figure 3.1 depicts the latent heat as observed in heat capacity measurements of the type-I superconducting transition in field for polycrystalline aluminium with a demagnetisation factor $N = 0.094$ (see section 3.4).

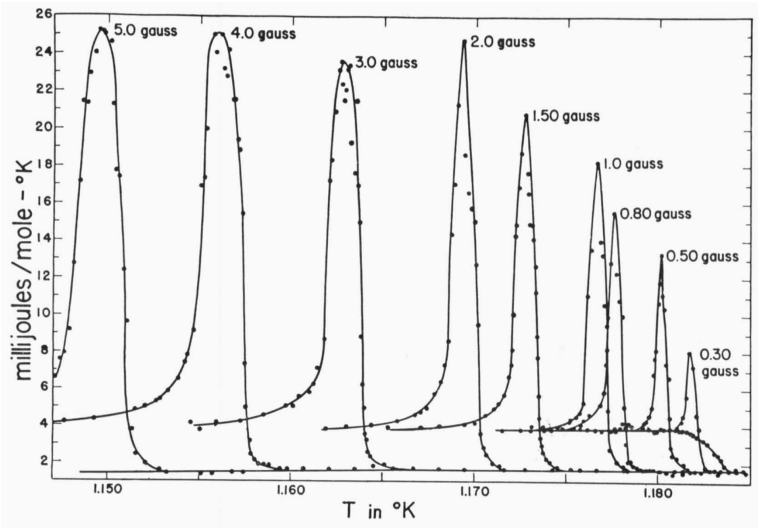

Figure 3.1: Specific heat data at the superconducting transition of Al in zero field and magnetic fields up to 5 gauss (0.5 mT). The sample is 99.999% pure aluminium and has a demagnetisation factor $N = 0.094$. Note the increase of the heat capacity jump size in fields compared to the zero-field value. Figure adopted from [73].

The Clausius-Clapeyron equation describes the change in entropy between two phases that are in equilibrium with respect to other parameters such as pressure or volume. Recalling that $C = -TdS/dT$ it is evident that the heat capacity should diverge at a first-order phase transition. Experimentally this is rarely observed due to the broadening of transitions

in imperfect systems. To distinguish between first and second-order phase transitions it is better to investigate the presence of the latent heat or hysteresis. The necessary introductory remarks on the heat capacity have been given at this point. The remainder of this chapter will focus on introducing the necessary introductory remarks on superconductivity.

3.2 London model

The first notion of a magnetic penetration depth in superconductors was proposed by the London brothers, who derived a governing equation for superconductors that encompassed the phenomenon of zero resistivity and the Meissner effect in the style of a two fluid model based on ^{4}He [74]:

$$\vec{\nabla} \times \vec{J}_s = -\frac{n_s e^2}{m_e}\vec{B}. \tag{3.31}$$

Here $\vec{J}_s$ is the supercurrent density, n_s the superfluid density, e the electron charge, m_e the electron mass and $\vec{B}$ the magnetic flux field. Making use of the Maxwell equation

$$\vec{\nabla} \times \vec{B} = \mu_0 \vec{J}_s \tag{3.32}$$

and the triple vector product, equation 3.31 can be rewritten to:

$$\begin{aligned} \vec{\nabla}^2 \vec{B} &= \frac{\mu_0 n_s e^2}{m_e}\vec{B}, \\ \vec{J}_s &= -\frac{n_s e^2}{m_e}\vec{A}, \end{aligned} \tag{3.33}$$

where $\vec{A}$ is the vector potential. From the first equation in 3.33 it follows, for simplicity in one dimension, that

$$B = \exp\left[-\sqrt{\frac{\mu_0 n_s e^2}{m_e}}x \right] = \exp\left(-\frac{x}{\lambda_L} \right) \tag{3.34}$$

where x, is the distance in the superconductor from the surface. In equation 3.34 the characteristic length over which a magnetic field decays is the London penetration depth λ_L:

$$\lambda_L = \sqrt{\frac{m_e}{\mu_0 n_s e^2}}. \tag{3.35}$$

It should be noted that the London model is based on local electrodynamics. For superconductors with a low value of the Ginzburg-Landau parameter κ nonlocal corrections have to be made in the derivation of the penetration depth.

3.3 Ginzurg Landau formalism

The Ginzburg-Landau (GL) [75] formalism describes the behaviour of superconductors in a phenomenological manner with local electrodynamics. The GL formalism is based on the description of second-order phase transitions [76]. Here the two phases are compared using the Gibbs free energy. This is accomplished by writing the Gibbs free energy of the phases in terms of an order parameter ψ, which is a complex macroscopic coherent wave function that is finite in the ordered phase and zero outside:

$$\begin{aligned} \psi &= 0, \qquad T > T_c, \\ \psi &\neq 0, \qquad T < T_c. \end{aligned} \tag{3.36}$$

Here T_c is the critical temperature separating the phases. The free energy F_s, a real quantity, is assumed to depend smoothly on $|\psi|$. The free energy density in the superconducting state f_s can be written as a function of the free energy density of the normal state f_n and of the order parameter:

$$f_s = f_n + a(T)|\psi|^2 + b(T)|\psi|^4 \tag{3.37}$$

where $a(T) \approx \dot{a}(T - T_c)$ and $b(T) \approx b > 0$ are phenomenological parameters that are smooth functions of temperature, with $\dot{a}$ and b constants. With the thermodynamic description of the normal and superconducting state Gibbs free energies $G_s = -\frac{1}{2}\mu_0 H^2$ and $G_n = 0$, the parameters a and b are further defined such that

$$G_s - G_n = -\frac{1}{2}\frac{a^2}{b} = -\frac{B_c^2}{2\mu_0}, \tag{3.38}$$

where $\frac{B_c^2}{2\mu_0}$ is known as the condensation energy, and B_c the thermodynamic critical field. From equation 3.13 it is clear that

$$C_s - C_n = -T\frac{\dot{a}^2}{b}, \tag{3.39}$$

where C_s (C_n) is the heat capacity in the superconducting (normal) state. Furthermore, at the transition temperature

$$\Delta C|_{T_c} = 4B_c(0)^2/\mu_0 T_c. \tag{3.40}$$

Here $\Delta C = C_s - C_n$. From equation 3.38 it is possible to show that the temperature dependence of B_c becomes

$$B_c(T) = B_c(0)\left[1 - \left(\frac{T}{T_c}\right)^2\right]. \tag{3.41}$$

While equation 3.41 is technically derivable from the GL formalism, it should be mentioned that this formula is an empirical result and that it is well suited

to describe the temperature behaviour of $B_c(T)$ of type-I superconductors.

The full GL equation for an inhomogeneous (ψ varies over r) superconductor in a magnetic field is given by

$$F_s(T) = F_n(T) + \int \left(\frac{1}{2m^*} \left| \left(\frac{\hbar}{i} \vec{\nabla} + 2e\vec{A} \right) \psi(r) \right|^2 + a|\psi(r)|^2 + \frac{b}{2}|\psi(r)|^4 \right) d^3r + \frac{1}{2\mu_0} \int \vec{B(r)}^2 d^3r. \quad (3.42)$$

Here $F_s(T)$ and $F_n(T)$ are the total free energies in the superconducting state and normal state respectively, $m^* = 2m_0$ which is the Cooper pair mass, $\vec{A}$ the magnetic vector potential, μ_0 the vacuum permeability and B the magnetic flux density field. This can be minimized with respect to $\psi(r)$ to yield

$$-\frac{\hbar^2}{2m^*} \left(\vec{\nabla} + \frac{2ei}{\hbar} \vec{A} \right)^2 \psi(r) + \left(a(T) + b(T)|\psi(r)|^2 \right) \psi(r) = 0. \quad (3.43)$$

From equation 3.43 the Meissner effect can be derived. The order parameter varies in position in the superconductor according to the coherence length ξ, while the Meissner effect subsists up to a distance λ from the surface. Both λ and ξ are characteristic healing lengths, i.e. they describe the distance over which a quantity attains the value present in the bulk. For the penetration depth λ and the coherence length ξ these are the decay of the magnetic field and the increase of the order parameter, respectively, as measured by the distance from the surface of the material into the interior. $\psi(x)$ for a distance x from the surface is given by

$$\psi(x) = \tanh\left(\frac{x}{\sqrt{2}\xi(T)} \right). \quad (3.44)$$

The GL coherence length is the same function for any interface a superconductor may have and can be written as

$$\xi(T) = \sqrt{\frac{\hbar^2}{2m^*|a(T - T_c)|}} = \xi(0) \left| \frac{T - T_c}{T_c} \right|^{-\frac{1}{2}}. \quad (3.45)$$

Applying the local gauge transformation in which

$$\psi(r) \to \psi(r) e^{\theta(r)}, \qquad \vec{A(r)} \to \vec{A(r)} + \frac{\hbar}{2e} \vec{\nabla}\theta, \quad (3.46)$$

the supercurrent density for a superconductor satisfying equation 3.43 in the ground state can be shown to be

$$\vec{J_s} = -\frac{2e}{\hbar} \rho_s \left(\vec{\nabla}\theta + \frac{2e}{\hbar} \vec{A} \right) = -\rho_s \frac{(2e)^2}{\hbar^2} \vec{A}, \quad (3.47)$$

with J_s the supercurrent density, e the electron charge, $\rho_s = \frac{\hbar^2}{2m^*}|\psi(r)|^2$ the phase stiffness, *i.e.,* the energy necessary to alter the condensate phase. Substituting the definition of ρ_s in equation 3.47, it is evident this equation is similar to equation 3.33, the London equation. Substituting further that $m^* = 2m_e$ (the mass of two superconducting electrons or one Cooper pair) and $2|\psi|^2 = n_s$ (the superfluid density), equation 3.33 is recovered. The GL penetration depth can then be derived in a similar manner as in the previous section, which leads to

$$\lambda(T) = \sqrt{\frac{m_e b}{2\mu_0 e^2 \dot{a}(T_c - T)}} = \lambda(0)\left|\frac{T - T_c}{T_c}\right|^{-\frac{1}{2}}. \tag{3.48}$$

An important distinction to be made is that the GL penetration depth is temperature dependent as opposed to the London penetration depth. Nevertheless, at zero temperature the GL penetration depth is equal to the London penetration depth.

3.3.1 Boundary surface energy

As a consequence of these two characteristic healing lengths, the superconducting order parameter has to vanish near the surface of the superconductor over a characteristic distance ξ and the magnetic field penetrates a characteristic distance λ into the superconductor. This leads to a small area in which the superconducting volumes and normal volumes are in competition with each other generating mixed phase volumes. The ordering of this competition can be analysed by conceptualizing a surface tension with an associated surface energy σ_{ns} between homogeneous phase volumes and mixed phase volumes. Defining σ_{ns} as the difference in free energy between a homogeneous phase and a mixed phase, then its value can be derived. Considering a superconductor at $r > 0$ with an interface at $r = 0$ to a normal phase at $r < 0$ with $B = B_c$, then from equation 3.42 one can derive for σ_{ns} [77]:

$$\sigma_{ns} = \int dr\big[-\frac{1}{2}b|\psi(r)|^4 + \frac{1}{2}\mu_0 M^2\big]. \tag{3.49}$$

Deep inside the superconductor ($r \gg 0$) the integral vanishes meaning the surface boundary is the contributor to σ_{ns}. If $\sigma_{ns} > 0$ the homogeneous phase has a lower free energy than the mixed phase and the system will remain in a fully superconducting state until the magnetic field exceeds the critical field value. This leads to type-I superconductivity in which an intermediate state appears at high fields which is mediated by a different mechanism than the σ_{ns} based ordering of the system. For $\sigma_{ns} < 0$, the mixed phase has a lower free energy which leads to type-II superconductivity. In this regime the superconducting system can lower the free energy by the nucleation of normal state regions in which a nonzero amount of flux is

present. The maximum lowering of the free energy is realized by maximizing the surface area of the boundary between the mixed phase and the superconducting phase. The first term in equation 3.49 gives the condensation energy for entering the superconducting state and the second term describes the cost of expelling the magnetic flux. An approximate and intuitive result for σ_{ns} is given by [78]

$$\sigma_{ns} = \frac{B_c^2}{2\mu_0}(\xi - \lambda_L). \tag{3.50}$$

Imagining the radius of normal state volumes in a type-II superconductor as λ_L with $B = B_c$ at the center and the distance ξ as the recovery distance of the superconducting order parameter, then it becomes evident why the formation of a mixed phase is inhibited for type-I superconductors. With a ξ that is larger than λ_L, the superconducting order parameter rises too slowly over the distance λ_L to form an adequate shielding current to contain the flux in the normal state region. Ginzburg and Landau showed that the exact point at which σ_{ns} equals zero is $\lambda_L/\xi = 1/\sqrt{2}$. Noticing that the GL coherence length and the GL penetration depth have the same temperature dependence, the GL parameter κ can be introduced:

$$\kappa = \frac{\lambda(T)}{\xi(T)} = \frac{\lambda(0)}{\xi(0)}. \tag{3.51}$$

This parameter serves to distinguish type-I and type-II superconductors:

$$\begin{aligned} \kappa &< \frac{1}{\sqrt{2}}, \qquad \text{type-I}, \\ \kappa &> \frac{1}{\sqrt{2}}, \qquad \text{type-II}. \end{aligned} \tag{3.52}$$

By accounting for σ_{ns}, the distribution of volumes will be governed by the minimisation of the three energies associated with the superconducting volume V_{sc}, mixed state boundary surface A_{ns} and the normal state volume V_n:

$$F = F_{sc}V_{sc} + \sigma_{ns}A_{ns} + F_nV_n. \tag{3.53}$$

3.4 Type-I superconductivity

The magnetic field inside a superconductor is described by the following equation

$$B = \mu_0(H + M), \tag{3.54}$$

where B is the magnetic flux density field, M the magnetisation and H the applied magnetic field. Because of the Meissner effect the magnetic field is expelled. Therefore one can write

$$B = 0, \qquad M = -H, \qquad \mu_0 H < B_c \tag{3.55}$$

for an ideal type-I superconductor. In this case a perfect diamagnetic response is generated in presence of an applied magnetic field up to the critical field B_c at which the system reverts to the normal state. Depending on the shape of a type-I superconductor, there can be a (strong) demagnetisation field induced by the screening currents of the superconductor. The magnetisation inside a superconductor is $M = -H$ as to cancel out H. As a consequence, M generates a north and south pole with an accompanying field distribution H_D in and adjacent to the superconductor. In this configuration the direction of H_D is opposite to the $M = -H$ direction. Thus H_D is in the same direction as the applied field H. Therefore a superconductor will experience a greater effective field $H_{eff} = H + H_D$ inside and at the surface. At a certain value of H, $\mu_0 H_{eff}$ experienced by the superconductor will exceed B_c before the applied field reaches B_c. To resolve this occurrence in a type-I superconductor, the superconductor reorders to a state governed by minimalisation of its free energy including the surface area and surface energy σ_{ns}. In this reordered state there are normal state volumes in which the flux penetrates the superconductor with $B = B_c$. This state is described as the intermediate state of a type-I superconductor. A schematic of this phenomenon is given in figure 3.2. The appearance of H_D due to the Meissner effect and the geometry of the superconductor can be described by introducing the demagnetisation factor N,

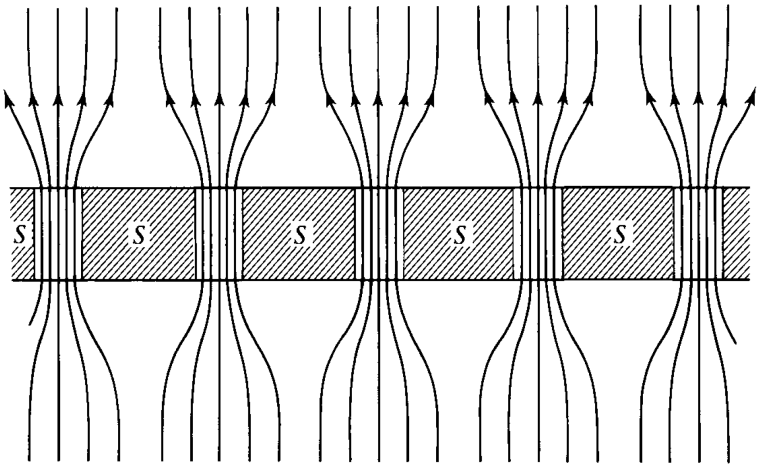

Figure 3.2: Schematic figure of the magnetic field configuration for a superconducting slab in the intermediate phase. The superconducting and normal state volumes are given by shaded and non-shaded areas, respectively. The distribution of the magnetic field lines shows an increase in flux density implying an increased magnetic field strength inside the normal state volumes of the superconductor compared to the magnetic field outside the superconductor *i.e.,* $B_{in} > B_{out}$. Figure adopted from [77].

$$B_{eff} = \frac{B_{app}}{1-N} \tag{3.56}$$

where B_{eff} is the increased magnetic field due to the demagnetisation effect and $B_{app} = \mu_0 H$.

It follows that for the superconducting volumes in a type-I superconductor for $B_c > B_{app} > B_c/(1-N)$

$$B = \mu_0(M+H) = 0, \qquad \mu_0 H = \frac{B_{app}}{1-N}, \tag{3.57}$$

$$\mu_0 M = -\frac{B_{app}}{1-N}, \qquad \chi = -1. \tag{3.58}$$

For the normal state volumes in the intermediate state for $B_c > B_{app} > B_c/(1-N)$ one has

$$B_{in} = \mu_0(H_{in}+M) = B_c, \qquad H_{in} = \frac{B_c}{\mu_0} \tag{3.59}$$

$$M = 0, \qquad \chi = 0. \tag{3.60}$$

Evidently, when approaching the intermediate state with increasing fields $\chi = -1$ and once the intermediate state is reached the susceptibility should slowly approach the normal state value $\chi = 0$ at $B = B_c$. This implies that for a type-I superconductor $-1 > \chi > 0$. However, often reported in the literature is a χ that is determined according to

$$\chi = \frac{-1}{1-N} = \frac{\partial M}{\partial H} \tag{3.61}$$

when measuring χ of the Meissner state. This is due to choosing $H = \frac{B_{app}}{\mu_0}$ in equation 3.61 rather than choosing $H = H_{in}$ with H_{in} the average over all normal and superconducting volumes in the superconductor. This *modus operandi* allows for a simple determination of the demagnetisation factor. One assumes that $\chi = -1$ for the measured superconductor if there is no demagnetisation field present, and the χ value measured that is larger than -1 can be uncovered by assuming equation 3.61. Naturally the volume fraction of the superconductor should be taken into account when making this assumption.

3.4.1 Differential paramagnetic effect

The differential paramagnetic effect (DPE) is commonly defined as the positive $\partial M/\partial H$ that can be measured in ac susceptibility measurements for a range of magnetic fields and temperatures preceding the superconducting to normal state transition in the intermediate state of a type-I superconductor. An example of this phenomenon is given in figure 3.3, where by using

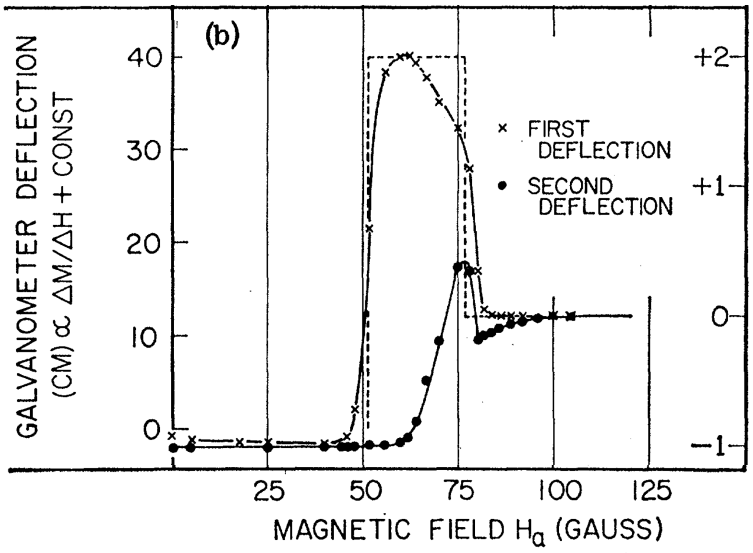

Figure 3.3: Galvanometric measurements of the magnetic susceptibility of a superconducting tantalum sphere ($N = 1/3$). The first and second deflection data-sets have been acquired by passing a current through the coil in which the sample is situated during the experiment. After the first deflection is recorded, the current is removed and reapplied to allow for the second deflection measurement. Figure adopted from [79].

a mutual inductance coil setup connected to a galvanometer the magnetic response of a type-I superconductor at the transition is recorded.

In principle a peak in the ac susceptibility can be observed for both type-I and type-II superconductors due to a finite demagnetisation factor. However, for a type-II superconductor the peak cannot exceed the diamagnetic signal of the superconducting volumes [80]. This is due to the field inside the vortex cores being equal to the applied field in contrast to the $H = H_c$ found in the normal state volumes of type-I superconductors. The excess field produced in the normal state volumes exceeding the applied field allows for a measurement that exceeds the diamagnetic signal of the superconducting volumes. The DPE can only be observed for materials that have a strong Meissner effect and a large superconducting volume fraction.

3.5 Type-II superconductivity

Type-II superconductors are distinguished from type-I superconductors by virtue of having $\kappa > \frac{1}{\sqrt{2}}$. Due to a positive σ_{ns} the ordering of the volumes with different phases differs from that of a type-I superconductor. In this regime there is a net energy benefit in maximising the surface area inside a superconductor occupied by the phase boundary. This is achieved by letting

the magnetic flux penetrate the superconductor in the form of individual flux lines carrying exactly one flux quantum $\Phi = \Phi_0 = h/2e \approx 2 \cdot 10^{-15}$ Wb. The penetration of flux in a type-II superconductor occurs for $B_{c1} < B_{app} < B_{c2}$ where B_{c2} (B_{c1}) is known as the upper (lower) critical field. It is at B_{c2} where all vortices overlap and the normal state is completely recovered. The upper critical field is given by

$$B_{c2} = \frac{\Phi_0}{2\pi\xi^2}. \tag{3.62}$$

B_{c2} is thus an indirect measure of the coherence length ξ. ξ can also be rewritten as [78]

$$\xi = \frac{\Phi_0}{2\sqrt{2}\pi B_c \lambda_L}, \tag{3.63}$$

where it is related to the thermodynamic critical field B_c. For type-II superconductors nothing of interest happens when $B = B_c$. However, B_c is still a measure of the condensation energy. B_c can be related to B_{c2} as

$$\kappa = B_{c2}/\sqrt{2}B_c, \tag{3.64}$$

which recovers the condition of $\kappa > \frac{1}{\sqrt{2}}$ for a type-II superconductor. B_{c1} can be written as

$$B_{c1} = \frac{\Phi_0 \ln(\kappa)}{4\pi\xi^2} \tag{3.65}$$

The destruction of superconductivity by increasing the applied magnetic field value to above the upper critical field B_{c2} has been thoroughly investigated. Generally, there are two distinct mechanisms by which the superconductivity is suppressed at B_{c2} [81, 82]. The more common occurring effect is the orbital pair breaking effect. Here the overlapping of the vortex lines at B_{c2} cause a decrease in the condensation energy of the superconductor. The magnetic field in the superconductor generates a Lorentz force on the Cooper pairs, which exceeds the binding force, thus suppressing superconductivity. The second less-common occurrence is the spin-paramagnetic effect. Here a Zeeman splitting of the energy levels of the electrons that form the Cooper-pairs is mediated by the magnetic field. This energy difference due to the splitting in the normal state exceeds that of the condensation energy and superconductivity is suppressed [83, 84]:

$$\frac{1}{2}\chi_N B_c^p/\mu_0 = \frac{1}{2}N(E_F)\Delta^2, \qquad B_c^p(0)/\mu_0 = g^{-1/2}\frac{\Delta}{\mu_B}. \tag{3.66}$$

Here χ_N is the normal state susceptibility, B_c^p the Pauli limited field, $N(E_F)$ the density of states at the Fermi energy, g the Landé g factor, Δ the BCS superconducting gap and μ_B the Bohr magneton. For a BCS superconductor B_c^p at zero temperature becomes [83]

$$B_c^p(0) = 1.86 T_c. \tag{3.67}$$

Both effects are usually affecting B_{c2} in a superconductor. The dominance of one effect over the other can be expressed using the Maki parameter. The Pauli limited field can be related to the orbital limited field with the Maki parameter [85]:

$$\alpha = \sqrt{2}\frac{B_c^{orb}}{B_c^p}. \tag{3.68}$$

Since the Maki parameter is of the order $\Delta(0)/N(E_F)$, it is usually quite small. This allows for B_{c2} to be dominated by the orbital pair breaking effect in most superconductors.

$$B_{c2}(0) = \frac{B_c^{orb}}{\sqrt{1+\alpha^2}} \tag{3.69}$$

To also account for strong scattering the full Werthamer-Helfand-Hohenberg (WHH) formalism in the dirty limit ($l \gg \xi_0$) can be used to numerically calculate B_{c2} [81, 82]:

$$\ln\frac{1}{t} = \sum_{\nu=-\infty}^{\infty}\left[\frac{1}{|2\nu+1|} - \left(|2\nu+1| + \frac{h^-}{t} + \frac{(\alpha h^-/t)^2}{|2\nu+1| + (h^- + \lambda_{so})/t}\right)^{-1}\right], \tag{3.70}$$

where $h^- = (4/\pi^2)[B_{c2}(T)/|dB_{c2}/dt|_{t=1}]$, $t = T/T_c$ and λ_{so} the spin-orbit scattering parameter which is a measure of the purity of the system. When $\lambda_{so} = 0$ equation 3.69 is recovered. The upper critical field limited by the orbital pair-breaking effect can be written as:

$$B_c^{orb}(0) = -\zeta\left(\frac{dB_{c2}}{dT}\right)_{T_c}, \tag{3.71}$$

where $\zeta = 0.69$ in the clean limit and $\zeta = 0.72$ in the dirty limit.

Anisotropy in the upper critical field with respect to the field direction is present in some superconductors. These systems are typically layered systems. The anisotropy in the upper critical field is usually described by either the 3D Ginzburg-Landau effective mass anisotropy model or the 2D Tinkham model. The formula for the 3D Ginzburg-Landau model is given as [86]:

$$\left(\frac{B_{c2}(\theta)\cos(\theta)}{B_{c2}^{\perp}}\right)^2 + \left(\frac{B_{c2}(\theta)\sin(\theta)}{B_{c2}^{||}}\right)^2 = 1. \tag{3.72}$$

Here $B_{c2}^{\perp}$ is the upper critical field with the field perpendicular to the layers and $B_{c2}^{||}$ is the upper critical field with the magnetic field applied parallel to the layers. The 3D anisotropic Ginzburg-Landau equation describes systems with a large anisotropy in the effective mass that are not 2D systems. To

accurately catch the anisotropic behaviour of 2D superconductors one can use the 2D model given by Tinkham [87]:

$$\left|\frac{B_{c2}(\theta)\cos(\theta)}{B_{c2}^{\perp}}\right| + \left(\frac{B_{c2}(\theta)\sin(\theta)}{B_{c2}^{||}}\right)^2 = 1. \tag{3.73}$$

This model is a solution of the 2D Ginzburg-Landau equations and is usually found to accurately capture the behavior in thin film superconductors.

3.6 Bardeen-Cooper-Schrieffer model

The Bardeen-Cooper-Schrieffer description of superconductivity is of microscopic origin with nonlocal electrodynamics applied [1]. The basic theory assumes a system in which the electrons are weakly coupled to the phonons and form spin-singlet Cooper pairs. The basis of BCS theory lies in the effective attractive interaction between electrons near the Fermi surface overcoming the Coulomb repulsion. One electron slightly deforms the lattice in the proximity resulting in a phonon. This phonon interacts with another electron on a small timescale and effectively lowers the energy of the second electron. In response, the second electron generates a phonon in the lattice, which is left to interact with other electrons in the proximity. Two of these electrons indirectly interacting with each other is known as a Cooper pair [88]. Perpetual repetition of these steps leads to an effective attractive interaction between electrons, with a negative potential:

$$V_{eff}(q,\omega) = |g_{eff}|^2 \frac{1}{\omega^2 - \omega_T^2}, \tag{3.74}$$

where g_{eff} is a simplification of a matrix element for scattering electrons near the Fermi surface from one momentum state to another in the energy range of k_BT [1, 88]. ω_T is a typical phonon frequency such as the Debye frequency ω_D and ω the frequency of the phonon in the effective interaction. This negative potential causes the attractive interaction between the electrons, lowering their potential energy, resulting in a lower ground state energy and a gap in the order of k_BT_c (T_c is the transition temperature). In the effective attraction, only electrons with opposite momenta and spin states are considered since these dominate the interaction, leading to s-wave superconductivity. The gap can be described with the BCS gap equation [1]:

$$1 = \lambda \int_0^{\hbar\omega_D} d\xi \frac{1}{\sqrt{\xi^2 + \Delta^2}} \tanh\left(\frac{\sqrt{\xi^2 + \Delta^2}}{2k_BT}\right), \tag{3.75}$$

where λ is the electron-phonon coupling parameter ($\lambda \ll 1$ for BCS) and Δ is the superconducting gap. At zero temperature the gap is given by

$$\Delta(0) = 1.74 k_B T_c. \tag{3.76}$$

The jump in the specific heat present at a normal-superconducting phase transition in BCS theory is given by

$$\frac{\Delta C}{\gamma T_c} = 1.43, \tag{3.77}$$

where γ is the Sommerfeld coefficient. The temperature dependence of the specific heat for an isotropic s-wave superconductor is given by [89]

$$C_s = 2N_0 \int_{-\infty}^{\infty} d\xi \sqrt{\xi^2 + \Delta^2} \frac{\partial}{\partial T} \left(\frac{1}{e^{\sqrt{\xi^2+\Delta^2}/T} + 1} \right), \tag{3.78}$$

where N_0 is the density of states in the normal state. Notably at low temperatures ($T < 0.3T_c$), the temperature dependence becomes exponential

$$C_s \approx \frac{2N_0\Delta^2}{T^2} e^{\Delta/T} \int_{-\infty}^{\infty} d\xi e^{-\xi^2/2\Delta T} \approx N_0 \left(\frac{\Delta(0)}{T} \right)^2 \sqrt{2\pi T \Delta_0} e^{-\Delta_0/T}. \tag{3.79}$$

The exponential dependence with respect to temperature is due to the reduced presence of quasiparticle excitations at low temperatures, which is always the case for an isotropic superconducting gap.

3.7 Low-temperature superconducting heat capacity

To investigate the low-temperature heat capacity of unconventional superconductors it is fruitful to introduce the mechanisms by which different symmetries lead to different temperature dependencies. To do so it is sufficient to treat the symmetries of a single wavefunction which is commensurate with Δ. Since the Cooper pairs that comprise the superconducting condensate are composed of spin 1/2 electrons, the order parameter symmetry must obey the imposed symmetries of the electrons *i.e.,* have a symmetric and anti-symmetric component. Writing the pair wavefunction Ψ_C of an electron pair in terms of spin and orbital angular momentum parts one obtains

$$\Psi_c = \psi_l(k)\psi_s(s1, s2). \tag{3.80}$$

The spin component is constructed with single particle wavefunctions

$$|\uparrow\rangle = \begin{pmatrix} 1 \\ 0 \end{pmatrix} \qquad |\downarrow\rangle = \begin{pmatrix} 0 \\ 1 \end{pmatrix} \tag{3.81}$$

which are eigenstates of the operators s^2 and s_z:

$$s_z = \frac{\hbar}{2} \begin{pmatrix} 1 & 0 \\ 0 & -1 \end{pmatrix}, \qquad s_z |\uparrow\rangle = |\uparrow\rangle, \qquad s_z |\downarrow\rangle = -|\downarrow\rangle. \tag{3.82}$$

For a spin singlet pair state which is antisymmetric under particle exchange and where the total spin $S = 0$ and the projection along the quantisation axis z $S_z = 0$, the eigenfunction can be written as

$$|\uparrow\downarrow\rangle - |\downarrow\uparrow\rangle = \begin{pmatrix} 0 & 1 \\ -1 & 0 \end{pmatrix} = i\sigma_y, \tag{3.83}$$

with σ_y one of the Pauli matrices

$$\sigma_x = \begin{pmatrix} 0 & 1 \\ 1 & 0 \end{pmatrix}, \qquad \sigma_y = \begin{pmatrix} 0 & -i \\ i & 0 \end{pmatrix}, \qquad \sigma_z = \begin{pmatrix} 1 & 0 \\ 0 & -1 \end{pmatrix}. \tag{3.84}$$

The total wavefunction of a spin singlet superconductor can be written as

$$\Psi_c = ig(k)\sigma_y = \sum_{m=-l}^{l} a_{lm} Y_{lm}(\hat{k}) i\sigma_y, \tag{3.85}$$

where $g(k)$ is the orbital part of the wavefunction, l is the orbital angular momentum, m the projection of l along the quantisation axis, Y_{lm} the spherical harmonics and a_{lm} complex coefficients representing the order parameter amplitude. a_{lm} has 1 and 5 coefficients for s-wave and d-wave superconductors, respectively. Since the spin component of a spin-singlet state is antisymmetric, the orbital component has to be symmetric:

$$g(k) = g(-k) \tag{3.86}$$

A spin triplet eigenstate projected on the quantisation axis can be written as

$$S_z = \begin{cases} 1, & |\uparrow\uparrow\rangle = \begin{pmatrix} 1 & 0 \\ 0 & 0 \end{pmatrix}, \\ 0, & |\uparrow\downarrow\rangle + |\downarrow\uparrow\rangle = \begin{pmatrix} 0 & 1 \\ 1 & 0 \end{pmatrix}, \\ -1, & |\downarrow\downarrow\rangle = \begin{pmatrix} 0 & 0 \\ 0 & 1 \end{pmatrix}. \end{cases} \tag{3.87}$$

The full wavefunction can be written in terms of the above parts

$$\Psi_{sc} = g_1(k)\,|\uparrow\uparrow\rangle + g_2(k)(|\uparrow\downarrow\rangle + |\downarrow\uparrow\rangle) + g_3(k)\,|\downarrow\downarrow\rangle\,, \tag{3.88}$$

where the states $S_z = 1, 0, -1$ can be written as

$$g_i(k) = \sum_{m=-l}^{l} a_{lm}^{\alpha} Y_{lm}(\hat{k}). \tag{3.89}$$

Here α denotes the spin state on the quantisation axis. For p-wave there are 9 complex coefficients constituting the order parameter. Usually another basis is used to describe a spin triplet wavefunction of a Cooper pair:

$$\Psi_c = i(\vec{d}(k) \cdot \vec{\sigma})\sigma_y = \begin{pmatrix} -d_x(k) + id_y(k) & d_z(k) \\ d_z(k) & d_x(k) + id_y(k), \end{pmatrix} \tag{3.90}$$

where $\vec{d}(k)$ is related to the OP amplitude as

$$g_1(k) = -d_x(k) + id_y(k), \qquad g_2(k) = d_z(k), \qquad g_3(k) = d_x(k) + id_y(k). \tag{3.91}$$

Since for spin-triplets wavefunctions the spin component is symmetric, the orbital component has to be antisymmetric:

$$\vec{d}(-k) = -\vec{d}(k) \tag{3.92}$$

As stated previously, the superconducting gap Δ is subject to the same symmetries as the single pair wavefunction. Δ can therefore be written as

$$\begin{aligned} \Delta &= \Delta_0 g(k) i\sigma_y, && \text{Singlet case} \\ \Delta &= \Delta_0 (\vec{d}(k) \cdot \vec{\sigma}) i\sigma_y, && \text{Triplet case.} \end{aligned} \tag{3.93}$$

Here Δ_0 is the k independent amplitude of the superconducting gap. The superconducting gap can be related to the single quasiparticle excitation spectrum by

$$E_k = \sqrt{\xi_k^2 + \Delta_k^2}, \tag{3.94}$$

which for spin singlets becomes

$$E_k = \sqrt{\xi_k^2 + \Delta_0 |g(k)|^2}, \tag{3.95}$$

and for spin triplets

$$E_k = \sqrt{\xi_k^2 + \Delta_0 |\vec{d}(k)|^2}, \tag{3.96}$$

or, if $\vec{d}(k)$ is not unitary for spin triplets

$$E_k = \sqrt{\xi_k^2 + \Delta_0 (|\vec{d}(k)|^2 \pm |\vec{d}(k) \times \vec{d}^*(k)|)}. \tag{3.97}$$

Equation 3.79 can be generalized to the form [89]:

$$C_s = 2N_0 \int_{-\infty}^{+\infty} d\xi \int \frac{d\Omega}{4\pi} E_k \frac{\partial}{\partial T} \frac{1}{e^{E_k/T} + 1}. \tag{3.98}$$

Here Ω is the solid angle. Depending on the structure of the superconducting gap, the low-temperature heat capacity can have different temperature dependencies which can be calculated according to equation 3.98.

$$C_s(T \ll T_c) \sim \begin{cases} \left(\frac{T_c}{T}\right)^{5/2} e^{-\Delta_0/T}, & \text{isotropic gap structure} \\ \left(\frac{T}{T_c}\right)^3, & \text{point node structure in the gap} \\ \left(\frac{T}{T_c}\right)^2, & \text{line node structure in the gap} \end{cases} \tag{3.99}$$

Care should be taken when analysing experimental results on the low-temperature temperature dependence of the heat capacity in view of the effects of non-magnetic impurities. Whereas isotropic s-wave superconductors are robust against non-magnetic impurities [90], superconductors with exotic anisotropic pairing symmetries are sensitive to these effects and the low-temperature temperature dependence can be altered by the effects of these impurities [91]. On the other hand, actively adding non-magnetic impurities to candidate unconventional superconductors is a strong tool to exclude the possibility of an isotropic s-wave symmetry.

Chapter 4

Heat capacity of type-I superconductivity in the Dirac semimetal $PdTe_2$

Type-I superconductivity was recently reported for the Dirac semimetal $PdTe_2$ ($T_c \approx 1.6$ K) with, remarkably, multiple critical fields and a complex phase diagram. Here, measurements of the specific heat utilizing a thermal relaxation technique are presented. Conventional weak-coupling BCS superconductivity is confirmed by examining the temperature dependence of the specific heat in zero field. By probing the latent heat accompanying the superconducting transition, thermodynamic evidence for type-I superconductivity is attained. The presence of the intermediate state is observed as a significant broadening of the superconducting transition onto lower temperatures at high fields as well as irreversibility in the specific heat in zero field cooled data at 8.5 mT.

4.1 Introduction

Recently, layered transition metal dichalcogenides have sparked great interest by virtue of their exotic electronic properties, especially the possibility of realizing novel quantum states stemming from the topological non-trivial band structure as uncovered by density functional theory [21, 92, 40, 39]. A generic coexistence of type-I and type-II three-dimensional Dirac cones has been proposed to be at play in these materials [39]. $PdTe_2$ is interesting in particular because of the appearance of superconductivity at $T_c \approx 1.6$ K [93, 44], as well as its classification as a type-II Dirac semimetal. The latter is extracted from a combination of *ab initio* electronic structure calculations and angle resolved photoemission spectroscopy [94, 41, 42, 39, 43]. A Dirac cone with a tilt parameter $k > 1$ breaking Lorentz invariance is the hallmark of a type-II Dirac semimetal [21]. The Dirac point then forms the touching point of the electron and hole pockets, possibly resulting in a nearly flat band adjacent to the Fermi level. This prompts the question of whether superconductivity is bolstered by the presence of the nearly flat band [95].

The superconducting properties of $PdTe_2$ have been extensively investigated. Transport and magnetic measurements carried out on single crystals of $PdTe_2$ revealed the existence of bulk type-I superconductivity, an uncommon feature for a binary compound [44]. The dc magnetization data showed the appearance of the intermediate state, the hallmark of type-I superconductivity in an applied magnetic field. This was further corroborated by the differential paramagnetic effect observed in ac magnetization measurements. A bulk critical field $B_c = 13.6$ mT was determined. A puzzling aspect is the detection of surface superconductivity with a critical field $B_c^{surf} = 34.9$ mT and a temperature dependence that does not follow the standard Saint-James-de Gennes model [96]. This led the authors of Ref. [44] to suggest surface superconductivity has a topological nature. Moreover, an even higher critical field of 0.3 T was observed in resistance data. The theoretical possibility of type-I superconductivity in $PdTe_2$ was analyzed within a microscopic pairing theory exploring the tilt parameter k of the Dirac cone [97]. The realization of type-I superconductivity was established for $k = 2$.

Evidence of the weak-coupling BCS nature of superconductivity in $PdTe_2$ was obtained through measurements of the specific heat [47], penetration depth [46, 45], scanning tunneling microscopy and spectroscopy (STM and STS) [43, 49, 50] and tunneling spectroscopy on side junctions [98]. Surprisingly, distinct and fairly large critical fields were observed in STM/STS measurements [49, 50], and their spatial distribution on the surface was attributed to a mixture of type-I and type-II superconductivity. This provided the motivation of further experimental work to unravel the nature of the su-

perconducting phase. Additional evidence for type-I superconductivity was inferred from the local electronic behaviour necessary to properly analyze the magnetic penetration depth data [46]. Evidence on the microscopic scale was obtained from transverse muon spin relaxation measurements in an applied magnetic field that unambiguously demonstrated the presence of the intermediate state [99]. Similarly, scanning SQUID magnetometry provided evidence of type-I superconductivity on the macroscopic scale [100]. Finally, it has been established that type-I superconductivity is robust under pressure [101].

Although the specific heat of $PdTe_2$ has been reported before, the focus was on elucidating the symmetry of the gap structure [47]. Heat capacity techniques can also be utilised to ascertain whether superconductors are type-I or type-II. Unlike type-II superconductors, type-I superconductors, when subjected to a magnetic field, will undergo a first-order phase transition. This can be verified by measuring the heat capacity in a magnetic field, which involves the latent heat associated with the transition. In this case the latent heat appears as an extra contribution to the jump in the specific heat at T_c, such that the jump size exceeds the value in zero magnetic field. Furthermore, for type-I superconducting samples that have a shape resulting in a nonzero demagnetization factor, the intermediate state emerges. The intermediate state contribution broadens the superconducting transition towards lower temperatures due to the gradual transformation of normal domains to superconducting domains. Hitherto, no thermodynamic evidence in favor of type-I or type-II superconductivity has been reported. This warrants a second specific heat study focusing on these aspects.

In this chapter heat capacity measurements of $PdTe_2$ in zero and applied magnetic fields are reported. The data in field show the presence of latent heat associated with a first-order transition and thus type-I superconductivity. The temperature variation of the critical field $B_c(T)$ follows the expected quadratic temperature variation up to 9.5 mT. The data at higher applied fields reveal the presence of a second, minority superconducting phase in the $PdTe_2$ crystal.

4.2 Experiment

$PdTe_2$ crystallises in the trigonal CdI_2 structure (space group $P\bar{3}m1$) [102]. The single crystal investigated in this study was taken from a batch grown with the modified Bridgman technique [103] as reported in Ref. [44]. The proper 1:2 stoichiometry within the 0.5% experimental resolution was inferred from scanning electron microscopy (SEM) with energy dispersive x-ray spectroscopy. Magnetization measurements showed a bulk T_c of 1.64 K

and B_c = 13.6 mT for a crystal cut from the same crystalline boule [44]. The rectangular-shaped single-crystalline sample used in this study has a size of 3 × 3 × 0.3 mm^3 along the a, a^* and c axis, respectively, and a mass of 39.66(2) mg.

Heat capacity measurements were carried out in an Oxford Instruments Heliox ^{3}He refrigerator down to 0.3 K by use of the dual slope thermal relaxation calorimetry technique [104]. In this technique the sample is kept at a stable temperature T_1. Heat is then applied to heat the sample from T_1 by $\Delta T/T$ to T_2, which is recorded. The data recorded represents the heating curve. Subsequently the heat is removed, and the sample cools back to a stable temperature T_1, which is recorded as well. This represents the cooling curve. The increase in temperature $\Delta T/T \approx 1.5$ %. Both the heating and cooling curves at each temperature point are used in the analysis. The curves together form one relaxation measurement. Each specific heat data point in this study presents the average of four relaxation measurements at the same temperature, totalling eight fitted curves.

The sample was attached to the sample platform with Apiezon N grease with the c axis perpendicular to the applied magnetic field. This configuration results in a demagnetizing factor N = 0.14 [105], sufficiently large to probe the intermediate state. All measurements in a magnetic field have been carried out with the sample first cooled down in field from the normal state to the base temperature. The data points are collected by step-wise heating to the desired temperature T_1.

4.3 Results

The as-measured total specific heat, consisting of the electronic and phononic contributions, is reported in figure 4.5, see Appendix. At low temperatures, the specific heat of a simple metal in the normal state is given by $C = \gamma T + \beta T^3$, where γ is the Sommerfeld coefficient and β is the phonon coefficient. We have determined γ and β by the usual procedure *i.e.,* by using the above mentioned relation and obtained values of 4.4 mJ/mol K^2 and 0.70 mJ/mol K^4, respectively. This γ value compares reasonably well to the 6.0 mJ/mol K^2 derived in previous work [47, 106]. The value β = 0.70 mJ/mol K^4 compares well to 0.66 mJ/mol K^4 of the previous heat capacity study [47]. The Debye temperature Θ_D can be calculated using $\Theta_D = \left(\frac{S12\pi^4 R}{5\beta}\right)^{\frac{1}{3}}$, where S is the number of atoms per formula unit and R is the gas constant. We obtain Θ_D = 202 K, which agrees well with the previously reported value of 207 K [106] and the calculated value of 211 K [47]. After subtracting the phononic contribution, the electronic specific

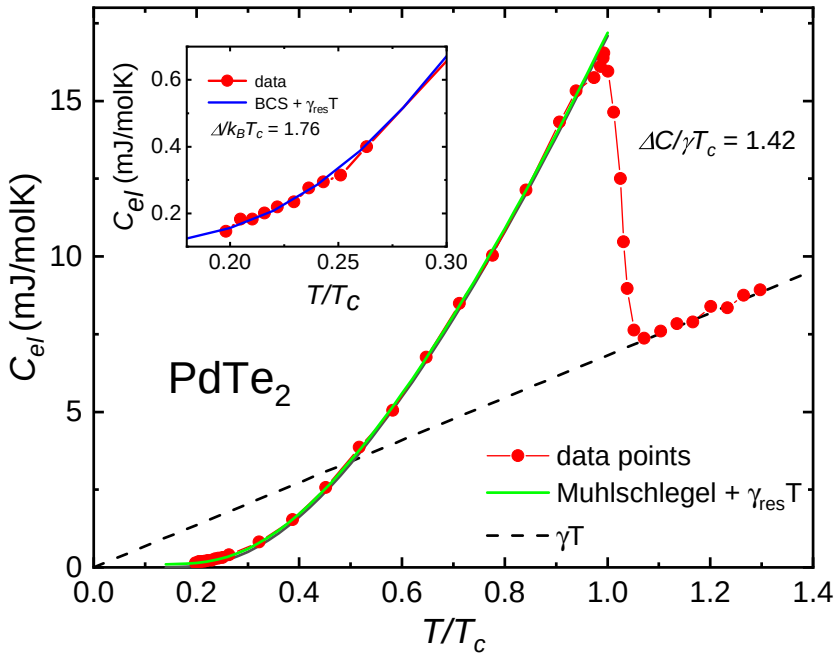

Figure 4.1: Reduced temperature (T/T_c) dependence of the electronic specific heat C_{el} of $PdTe_2$ in zero field. Red dots and line: experimental data; green solid line: BCS temperature dependence according to Mühlschlegel with a small residual term $\gamma_{res}T$ added; black dashed line: extrapolation to zero of the linear electronic specific heat in the normal state. The jump in the specific heat quantified with the BCS relation $\Delta C/\gamma T_c$ is equal to 1.42. Inset: Specific heat at low temperatures compared with the low-temperature BCS behaviour with a small residual term $\gamma_{res}T$ (see text).

heat, C_{el}, results.

The overall temperature variation of the electronic specific heat is presented in figure 4.1 in reduced temperature (T/T_c) with $T_c = 1.54$ K. Here, T_c is taken as the temperature where C_{el} has its maximum value.

The jump at T_c quantified with the BCS relation $\Delta C/\gamma T_c$, where ΔC is the jump in the specific heat, equals 1.42, which is close to the textbook value of 1.43, confirming the weak-coupling BCS nature of superconductivity in $PdTe_2$. The full-range temperature dependence of a weak-coupling BCS superconductor as tabulated by Mühlschlegel [107] is given by the green line in figure 4.1. In order to better match the experimental data, a small residual linear term with $\gamma_{res} = 0.10$ mJ/mol K^2 is added. This accounts for 2.2% of the sample that apparently remains in the normal state. At low temperatures the superconducting specific heat is described by the relation

$C = C_n 3.5T^{-1.5}e^{-1.76/T}$ (Ref. [107]), where C_n is the specific heat of the electronic normal state at $T = T_c$. Here, the BCS gap relation $\frac{\Delta}{k_B T_c} = 1.76$ is incorporated. The low-temperature behaviour is in full accordance with the weak-coupling BCS relation as shown in the inset of figure 4.1, further corroborating a conventional superconducting state in this $PdTe_2$ crystal.

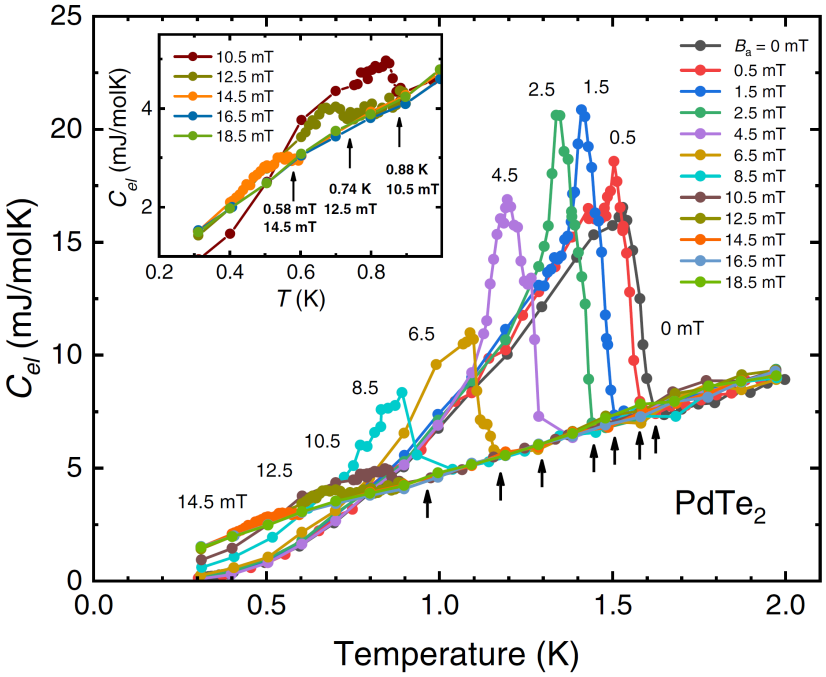

Figure 4.2: Temperature dependence of the electronic specific heat C_{el} of $PdTe_2$ in zero field and in magnetic fields up to 18.5 mT as indicated. An increase in the size of the specific heat jump at T_c is observed in field. T_c's are indicated by arrows. For $B \geq 10.5$ mT the jump size is strongly reduced. Inset: Zoom of the data in the low-temperature range for 10.5 mT $\leq B \leq$ 18.5 mT.

Figure 4.2 shows the temperature dependence of the electronic specific heat $C_{el}(T)$ in zero field and magnetic fields ranging up to 18.5 mT. The same data plotted as C_{el}/T versus T are presented in figure 4.6. An increase in the height of the transition peak for fields up to 4.5 mT compared to the peak at 0 mT is observed. This implies extra energy is necessary to complete the transformation into the normal phase in small fields. At higher fields, especially at 6.5 and 8.5 mT, a broadening of the transition temperature towards lower temperatures is visible. In the experimental configuration used, the crystal has a demagnetization factor of 0.14, causing the intermediate state to form. It is likely that the superconducting transition is considerably broadened at higher fields due to the intermediate state. The region

in the $B - T$ phase diagram occupied by the intermediate phase is shown in figure 4.3. At even higher magnetic fields, up to 16.5 mT, the transition broadens further and is no longer observed above this field. Remarkably, for $B \geq 10.5$ mT the step size ΔC abruptly decreases.

In figure 4.3 the B - T phase diagram is mapped out by tracing the onset temperatures of superconductivity in applied magnetic fields, indicated by the arrows in figure 4.2. In previous research [44] the phase diagram for bulk superconductivity probed by different techniques was found to follow the textbook relation

$$B_c(T) = B_c(0)\big[1 - (T/T_c)^2\big], \tag{4.1}$$

where $B_c(0) = 13.6$ mT and $T_c = 1.64$ K. The new data are in good agreement with the previous result with $T_c = 1.60$ K (solid blue line in figure 4.3). For fields $B \geq 10.5$ mT, however, we observe a somewhat higher T_c than expected, which presents the onset temperature of the transition with a reduced specific heat step (see the inset in figure 4.2). We attribute the reduced ΔC to a second, minority superconducting phase. The Meissner-to-intermediate phase line is given by the thin solid blue line. Its position is calculated by assuming that a type-I superconductor is in the intermediate state for $B_c(1 - N) < B_{app} < B_c$ where B_{app} is the applied magnetic field and $N = 0.14$ is the demagnetization factor.

Figure 4.4 depicts the zero-field cooled (ZFC) and field cooled (FC) specific heat data as a function of temperature at 4.5 mT and 8.5 mT. All measurements here were carried out by cooling down to base temperature either in field or without field. At the base temperature the field was applied (ZFC) or kept constant (FC). Next, the sample was heated to different temperatures while keeping the field constant. The measurements carried out at 4.5 mT are given by black and red symbols, respectively, and no difference between the FC and ZFC data is found. This shows the phase transformation is the same for FC and ZFC at this particular field strength. In the case of 8.5 mT, however, an odd feature is observed in the ZFC data in the temperature range of $0.75-0.87$ K. The heating curve of the first thermal relaxation measurement results in a much larger specific heat as presented in figure 4.7. This is shown by the blue symbols. All subsequent data points (cyan symbols), including those derived from the cooling curve of the first relaxation measurement, fall on top of the FC data-set (green symbols). This effect is observed only in the temperature range of the intermediate phase.

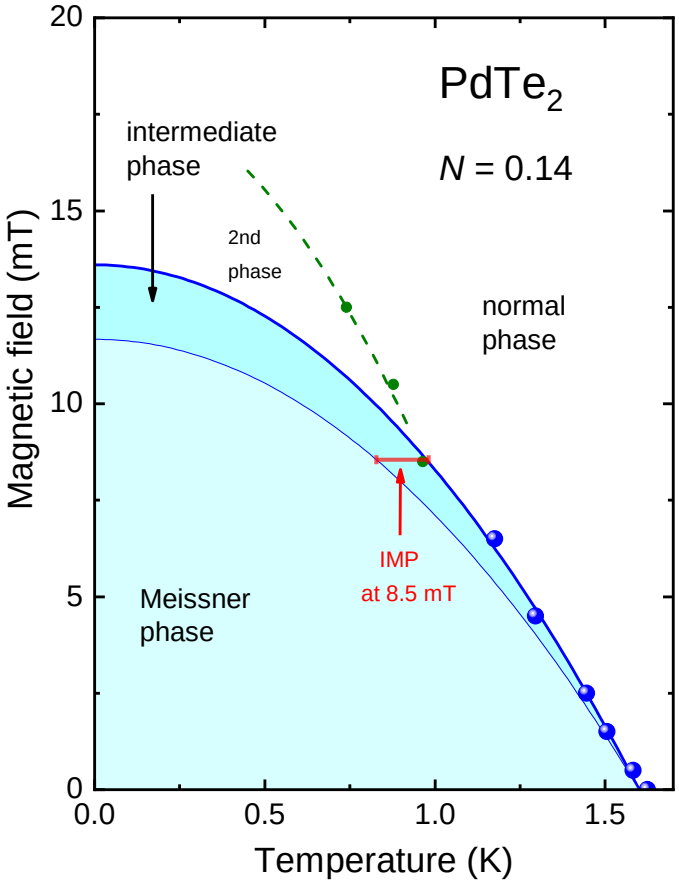

Figure 4.3: The $B-T$ phase diagram of $PdTe_2$ obtained by plotting the onset superconducting transition temperature for different magnetic fields. Blue symbols: data points; thick solid blue line: $B_c(T) = B_c(0)\left[1-(T/T_c)^2\right]$, with $B_c(0) = 13.6$ mT and $T_c = 1.60$ K; thin solid blue line: Meissner-to-intermediate phase (IMP) transition line $B_{IMP}(T) = B_c(T)(1-N)$, with $N = 0.14$; green symbols: T_c of a second, minority phase; dashed green line: guide to the eye; red solid bar: temperature range of the intermediate state at 8.5 mT (see text).

4.4 Discussion

The overall temperature variation of the superconducting contribution to the specific heat is in very good agreement with the tabulated Mühlschlegel values. At the same time the low-temperature data $T/T_c < 0.3$ obey the exponential expression for BCS superconductivity with $\frac{\Delta}{k_B T_c} = 1.76$ [107]. The jump size $\Delta C/\gamma T_c = 1.42$ conforms with the weak-coupling BCS expectation of 1.43. These results compare well to previous work where a weakly to moderately coupled superconducting state and a conventional isotropic

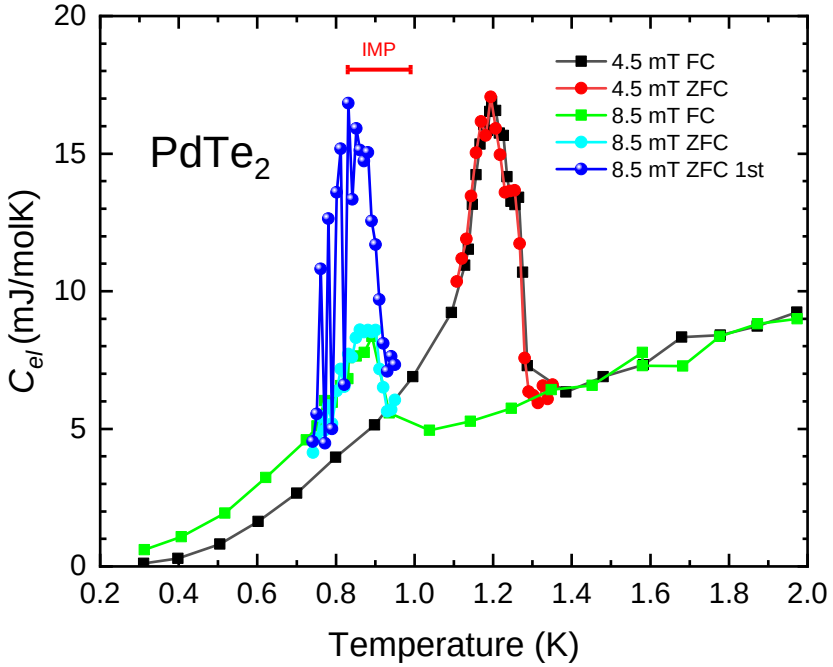

Figure 4.4: Temperature dependence of the electronic specific heat C_{el} of $PdTe_2$ measured FC and ZFC at $B = 4.5$ and 8.5 mT. The squares depict FC data, whereas the dots depict ZFC data. No difference between FC data and ZFC data is observed at $B = 4.5$ mT. In the ZFC data taken at 8.5 mT a large specific heat is observed, but only when derived from the heating part of the first relaxation curve (see text). No difference is observed with respect to FC data for subsequent measurements. The red bar depicts the temperature interval where the intermediate phase in 8.5 mT is expected according to figure 4.3.

gap are reported [47, 46, 45, 50, 49, 98]. Compared to the previous specific heat study [47], the γ value of 4.4 mJ/mol K^2 is nearly 20 % lower. This is possibly related to a different carrier density n considering the semimetallic properties of $PdTe_2$. Differences in carrier density are also inferred from penetration depth measurements. In a previous study using single crystals from the same batch, values for the penetration depth $\lambda(0)$ were obtained that ranged from 377 to 482 nm [46]. There $\lambda(0)$ was directly related to n in an extended London model used to analyze the data where the assumption $n_s = n$ was made, with n_s being the superfluid density. The difference in the value of $\Delta C/\gamma T_c$ between the previous heat capacity study (1.52[47]) and this work (1.42) is understood as a difference in coupling strength. This is in line with the results of penetration depth studies [46, 45], where similar differences in $\Delta/k_B T_c$, ranging from 1.77 to 1.83, were found. The γ value

can be related to the critical field [78]:

$$\Delta C = \frac{4B_c(0)^2}{\mu_0 T_c} = 1.43\gamma T_c, \tag{4.2}$$

where ΔC and γ are per unit volume. With the values $\gamma = 4.46$ mJ/molK^2, $T_c = 1.62$ K, $\Delta C/\gamma T_c = 1.42$ and the molar volume 4.34×10^{-5} m^3/mol, we calculate $B_c(0) = 10.9$ mT. This value is smaller than the measured value $B_c(0) = 13.6$ mT. Examining the previous specific heat study [47], where $\gamma = 6.01$ mJ/mol K, $T_c = 1.8$ K and $\Delta C/\gamma T_c = 1.52$ were reported, equation 4.2 gives $B_c(0) = 14.6$ mT, while $B_c(0) = 19.5$ mT is the measured value. Again, a similar sizeable difference is observed. As such we suspect equation 4.2 does not hold precisely for $PdTe_2$.

The temperature dependence of the electronic specific heat C_{el} in magnetic fields shown in figure 4.2 is consistent with that of a first-order phase transition. The latent heat appearing with a first-order phase transition is visible as the increased peak height in the specific heat in small fields relative to zero field. Consequently, we conclude that the type-I nature of $PdTe_2$ is successfully probed via the presence of latent heat near the superconducting transition in field. Further evidence for the existence of type-I superconductivity can be obtained by probing the intermediate state. In this study the sample and field geometry results in a demagnetization factor $N = 0.14$. From figure 4.3 it is clear that for $B \geq 6.5$ mT the intermediate state spans more than 0.1 K at fixed fields, a sufficiently large interval to probe the broadening of the transition towards lower temperatures. In the specific heat data in field the broadening towards lower temperatures is visible given the changes in the range of 0.5 to 8.5 mT. Especially for $B \geq 6.5$ mT, the broadening is very clear as the specific heat is raised considerably above the zero-field value in a larger temperature range.

The $B_c(T)$ data points traced in figure 4.3 closely follow the results probed by dc and ac magnetization measurements in previous work [44] up to $B = 8.5$ mT. Here the phase line is the boundary for bulk superconductivity and is represented by equation4.1 with $B_c(0) = 13.6$ mT and $T_c = 1.60$ K. However, above 8.5 mT, where ΔC is suddenly reduced, superconductivity is observed above the expected $B_c(T)$-curve. It is of importance to investigate whether this can be caused by the intermediate phase. The temperature dependence of the normal-state volume fraction F_N in the intermediate state in fixed fields for $B_c(1-N) < B_{app} < B_c$ is given by

$$F_n = \frac{1-t^2}{t_c^2-1}\frac{1-N}{N} + \frac{1}{N}, \tag{4.3}$$

where t is the reduced temperature T/T_c, t_c is the reduced critical temperature $T_c(B_{app})/T_c(0)$ and $N = 0.14$ is the demagnetization factor [108].

Equation 4.3 shows F_n has a smooth temperature variation and cannot suddenly collapse. The reduced critical temperature t_c in equation 4.3 can be rewritten using equation (4.1): $t_c = \sqrt{1 - \frac{B_c(T)}{B_c(0)}}$. From this, no sudden decrease in F_n is possible either. We therefore exclude the intermediate phase as a possible cause for the elevated T_c and reduced specific heat step. A more likely explanation is that superconductivity survives in a small volume fraction (10%) of the crystal with a slightly different $PdTe_{2+x}$ stoichiometry [93]. We remark a similar additional phase line was obtained in a previous study [44] by analyzing the screening signal in the ac susceptibility for small driving fields. Since the screening signal persisted above B_c, it was attributed to superconductivity of the surface sheath with a critical field $B_c^s \approx 35$ mT.

In the heating curves of the first relaxation measurements of the ZFC data detailed in figure 4.4 an increase of the specific heat at 8.5 mT appears, whereas no such increase was found at 4.5 mT. Given the temperature range in which it appears, between 0.75-0.87 K, it can be attributed to the intermediate phase. We remark this range is a little lower than the expected range 0.83-0.98 K (red bar) calculated from the phase diagram in figure 4.3. The spatial arrangement and size of the normal and superconducting domains will depend on the field and temperature history because of pinning effects. This may cause hysteretic behaviour. Such a history dependence was also reported by probing the intermediate phase in $PdTe_2$ by scanning squid magnetometry [100]. The absence of irreversibility in the relaxation curves at 4.5 mT shows the phenomenon is much weaker at this field. Moreover, the increase in specific heat in the first measurement point is more difficult to observe at 4.5 mT due to the smaller temperature range in which the intermediate phase is present. A closer examination of the irreversibility in ZFC calorimetry should be possible with ac calorimetry, as long as the change in the specific heat does not exceed the amplitude of the ac heat pulse.

4.5 Conclusion

The temperature dependence of the specific heat of $PdTe_2$ in zero field and magnetic fields was measured in order to produce thermodynamic evidence of the type-I nature of superconductivity. From the zero-field data a weak-coupling BCS superconducting state is inferred to conform with the literature. The data in small magnetic fields show the presence of latent heat at the superconducting transition, where the step in the specific heat ΔC exceeds the zero-field value. The intermediate state was probed by (i) a significant broadening of the transition onto lower temperatures for $B > 6.5$ mT and (ii) the appearance of irreversibility in the specific heat at 8.5 mT in ZFC data. The critical field for bulk superconductivity extracted from

the data follows the standard temperature dependence with $B_c = 13.6$ mT and $T_c = 1.60$ K for $B \leq 8.5$ mT. In fields $B \geq 10.5$ mT the data reveal the presence of a second, minority phase, with a volume fraction of 10%, possibly due to off-stoichiometric $PdTe_{2+x}$ regions.

4.6 Appendix

The as-measured specific heat of $PdTe_2$ in zero field is given in figure 4.5. The dashed line is a fit to the data above the transition temperature according to $C = \gamma T + \beta T^3$. This fit is attained from the C/T data presented in the insert where the slope of the data above T_c is the phononic contribution and the intersect at zero gives the γ value. Clear metallic behaviour is observed above T_c allowing for a good fit.

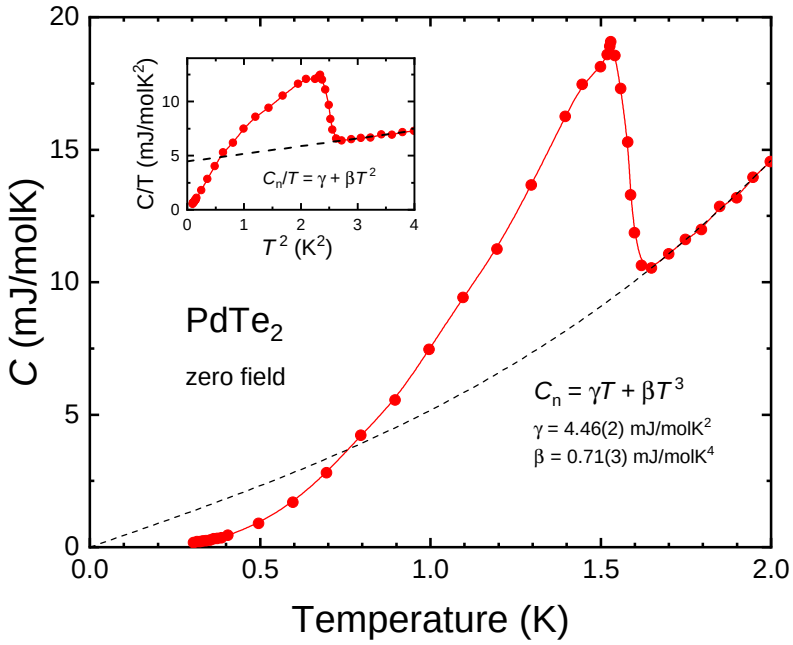

Figure 4.5: As-measured specific heat of $PdTe_2$ in zero field in a plot of C versus T. The dashed line shows the normal state contribution $C_n = \gamma T + \beta T^3$, with the fitted values of γ and β listed in the graph. Inset: Same data in a plot of C/T versus T^2.

In figure 4.6 the electronic specific heat in a plot of C_{el}/T versus T in zero and in applied magnetic fields up to 18.5 mT is given. The increase in the jump size of the superconducting transition with respect to increasing magnetic field strength between 0 (black) and 6.5 mT (dark yellow) is

due to the present latent heat in the transition, a hallmark of type-I superconductivity. The jump at the transition collapses for $B \geq 10.5mT$ and superconductivity is no longer observable in the specific heat at $B = 16.5$ mT.

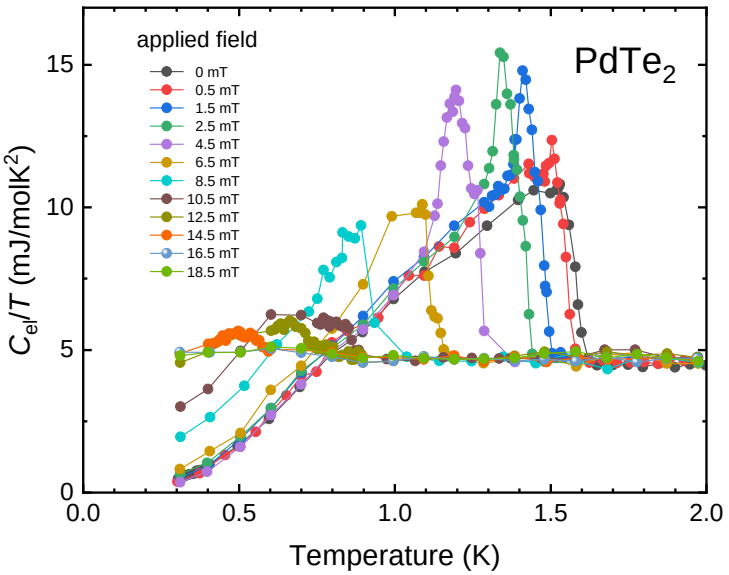

Figure 4.6: Temperature variation of C_{el}/T of $PdTe_2$ in zero field and in magnetic fields up to 18.5 mT, as indicated. The increase of the step size of the specific heat at the superconducting transition temperature measured in magnetic field is clearly observed. This is due to the first-order nature of the transition which involves latent heat. For $B \geq 10.5$ mT the specific heat peak collapses.

Figure 4.7 depicts the relaxation curves of the heat capacity measurements at $T = 0.8$ K and $B = 8.5$ mT. The first heating curve which is the increasing part of the red curve is longer than the subsequently measured curves, indicating a longer relaxation constant and thus a larger heat capacity. The cooling component of all curves overlap in shape and length indicating the determined relaxation constants and heat capacities are equal. The larger heating curve observed in the first heating curve is attributed to a change in the flux structure of the intermediate phase. This should be a regular observation since hysteresis effects are commonly observed in measurements of quantities affected by the intermediate state. However, the occurrence and observation of hysteretic effects are difficult to reproduce consistently due to imperfections of the crystals [79]. Further investigation into the effect of the changing magnetic structure of the material in the

intermediate should be carried out with ac heat capacity. Ac heat capacity would allow for measuring smaller minute changes in the heat capacity with the sacrifice of measuring the absolute value of the heat capacity. To explore the occurrence of hysteresis in the heat capacity in the intermediate state of $PdTe_2$, absolute value measurements are not necessary making ac heat capacity measurements the best option.

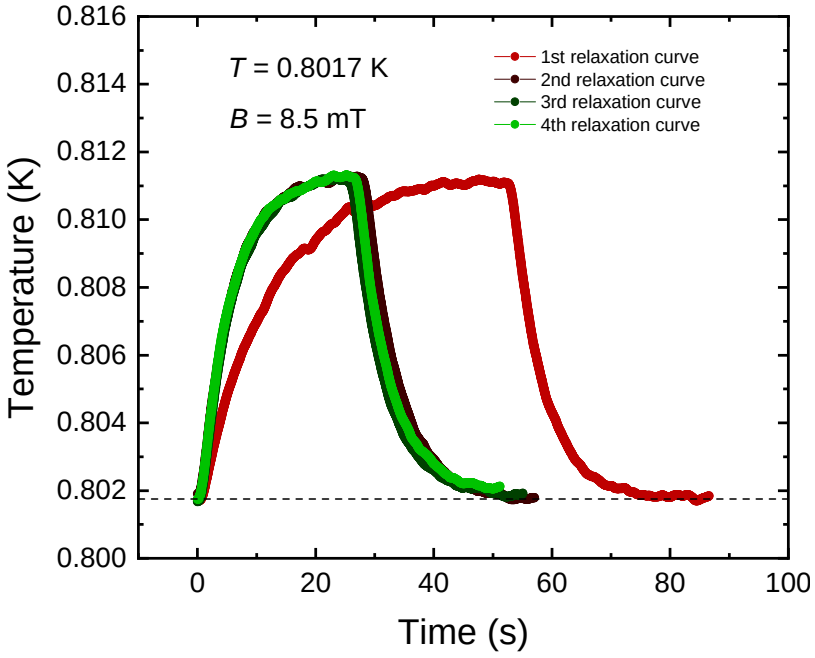

Figure 4.7: Four subsequent relaxation curves at $T = 0.802$ K and $B = 8.5$ mT (applied after zero field cooling). The first heating curve (first part of the red solid line) reveals a longer relaxation time, implying a larger heat capacity. The cooling curve (second part of the red solid line) and all other heating and cooling curves show the same, shorter relaxation time. The effect is attributed to a change in the flux structure in the intermediate state in the first heating cycle.

Chapter 5

Disorder-induced transition from type-I to type-II superconductivity in the Dirac semimetal $PdTe_2$

We report a doping study directed at intentionally inducing disorder in $PdTe_2$ by the isoelectronic substitution of Pt. Two single-crystalline batches $Pd_{1-x}Pt_xTe_2$ have been prepared with nominal doping concentrations $x = 0.05$ and $x = 0.10$. Sample characterization by energy dispersive x-ray spectroscopy revealed Pt did not dissolve homogeneously in the crystals. For the nominal value $x = 0.10$, small single crystals cut from the batch appeared to have $x = 0.09$, as well as the non-stoichiometric composition $Pd_{0.97}Pt_{<0.004}Te_{2.03}$. Magnetic and heat capacity measurements demonstrate a transition from type-I to type-II superconducting behaviour upon increasing disorder. From transport measurements we calculate that a residual resistivity $\rho_0 = 1.4$ $\mu\Omega$cm suffices to turn $PdTe_2$ into a superconductor of the second kind.

5.1 Introduction

Recently, interest in transition metal dichalcogenides has increased significantly due to their extraordinary electronic properties. Notably, the opportunity to realise novel quantum states arising from the topologically nontrivial band structure, as found by density functional theory [21, 92, 40, 39], attracts much attention. The formation of both type-I and type-II bulk Dirac cones has been predicted [39]. Of special interest in this family is the semimetal $PdTe_2$, since it undergoes a superconducting transition at $T_c \sim 1.7$ K [93]. Furthermore, $PdTe_2$ is classified as a type-II Dirac semimetal, as uncovered by angle-resolved photoemission spectroscopy and *ab initio* electronic structure calculations [39, 94, 41, 42, 43]. A type-II Dirac semimetal is characterised by a Dirac cone with a tilt parameter $k > 1$ leading to broken Lorentz invariance [21]. It is predicted that for Dirac semimetals with $k \approx 1$, meaning close to the topological transition at $k = 1$, superconductivity is generally of the second type (type-II) [95]. For $k > 1$, superconductivity becomes of the first kind (type-I). Interestingly, $PdTe_2$ [44, 48] is a type-I superconductor and based on its T_c Shapiro *et al.* [97] estimated $k \approx 2$. In view of the effect topology has on superconductivity in these systems, it is of interest to investigate whether the superconductivity type can be altered by, for instance, doping.

Superconductivity in $PdTe_2$ has been explored in great detail. Type-I superconductivity was uncovered with the help of magnetic and transport measurements on single crystals [44]. The intermediate state, a hallmark of type-I behaviour, was observed through the dc magnetization curves and the differential paramagnetic effect in the ac susceptibility data. Here, a bulk critical field $B_c(0) = 13.6$ mT was determined in conjunction with a surface critical field $B_c^S(0) = 34.9$ mT. Moreover, the temperature dependence of the surface superconductivity did not follow the Saint-James-de Gennes model [96]. Peculiarly, from resistance measurements a critical field $B_c^R(0) = 0.32$ T was deduced. Weak-coupling conventional superconductivity in $PdTe_2$ was demonstrated via measurements of the heat capacity [47, 48], penetration depth [45, 46], scanning tunneling microscopy and spectroscopy (STM/STS) [43, 49, 50], and side junction tunneling spectroscopy [98]. Superconductivity is partly attributed to a van Hove singularity situated at ~ 30 meV above the Fermi level [109, 110].

On the other hand, a mixed type-I and type-II superconducting state was concluded from STM/STS [49, 50] and point contact spectroscopy (PCS) [111] measurements. In a magnetic field a range of critical fields was observed at the surface, which was explained by spatially separated type-I and type-II regions. However, later muon spin rotation measurements [99] and scanning squid magnetometry [100] provide solid evidence for bulk type-I supercon-

ductivity probed on the microscopic and macroscopic scale, respectively. Finally, evidence for bulk type-I superconductivity was attained through heat capacity measurements by demonstrating the presence of latent heat [48]. Measurements under hydrostatic pressure show that superconductivity is still present at 5.5 GPa [38] and remains of the first kind at least until 2.5 GPa [101].

Substitution or doping studies using $PdTe_2$ are scarce. Kudo *et al.* [106] examined Pd substitution in $AuTe_2$ by preparing a series of $Au_{1-x}Pd_xTe_2$ samples. Bulk superconductivity emerges at $x \approx 0.55$ with $T_c \approx 4.0$ K as evidenced by heat capacity measurements. At lower x values the Te-Te dimer connections stabilise a monoclinic crystal structure in which superconductivity is absent [106]. The strong-coupled nature of superconductivity near $x \approx 0.55$ is attributed to a large density of states (DOS) at the Fermi level. Further increasing the Pd content results in weak-coupling superconductivity with lower transition temperatures, as expected from approaching the stoichiometric end compound $PdTe_2$. Ryu investigated Cu doping in $PdTe_2$ by preparing a series of Cu_xPdTe_2 samples [112]. Optimal doping was found near $x = 0.05$ with bulk superconductivity at $T_c \approx 2.6$ K [112, 113]. The increase of T_c is attributed to an increase in the DOS at the Fermi level due to the hybridization of Te p and Cu d orbitals along the c axis, effectively reducing the two-dimensional nature of this layered material. This is in line with the Cu atoms being intercalated in the van der Waals gaps. STM/STS measurements provide evidence that $Cu_{0.05}PdTe_2$ is a homogeneous type-II superconductor [114]. This change, compared to the STM/STS data on $PdTe_2$ [49, 50] that revealed a mixed type-I/II behaviour, is explained by Cu intercalation inducing disorder. This effectively reduces the electron mean free path l_e and the coherence length ξ, thus increasing the Ginzburg Landau (GL) parameter $\kappa = \frac{\lambda}{\xi}$ to larger than the $1/\sqrt{2}$ threshold for type-I behaviour.

Here we report the results of a doping study, directed to intentionally induce disorder in $PdTe_2$ by substituting Pd by isoelectronic Pt. We have prepared $Pd_{1-x}Pt_xTe_2$ crystals with nominal doping concentrations $x = 0.05$ and $x = 0.10$. Sample characterization by energy dispersive x-ray spectroscopy (EDX) revealed that Pt did not dissolve homogeneously in the crystals. Notably, small crystals cut from the nominal $x = 0.10$ batch appeared to have $x = 0.09$, or the non-stoichiometric composition $Pd_{0.97}Pt_{<0.004}Te_{2.03}$. Transport, magnetic and heat capacity measurements demonstrate a transition from type-I to type-II superconducting behaviour upon increasing disorder.

5.2 Experiment

$PdTe_2$ crystallises in the trigonal CdI_2 structure (space group $P\bar{3}m1$). Two single-crystalline batches $Pd_{1-x}Pt_xTe_2$ were prepared with $x = 0.05$ and $x = 0.10$ using a modified Bridgman technique [103]. The same technique was previously used to prepare $PdTe_2$ single crystals [44]. Small flat crystals were cut from the prepared batches by a scalpel. The crystals have an area of 2×3 mm^2 and a thickness of about 0.3 mm. Scanning electron microscopy with energy dispersive x-ray spectroscopy (SEM/EDX) was carried out with the help of a Hitachi table top microscope TM3000. For details of the SEM/EDX results see the appendix. SEM micrographs taken on cut crystals and other sample pieces revealed the final composition can deviate from the nominal one and that Pt did not dissolve in the same amount in all pieces. In fact for the cut crystal with a nominal Pt content of 5 at.% no Pt was detected. This crystal has a stoichiometric composition with a Pd:Te ratio of 1:2 (the error in these numbers is 1%). Transport, ac susceptibility and heat capacity measurements were carried out on this sample, which we labeled #ptnom5. For the experiments on the 10 at.%Pt concentration we used two crystals. One sample had a composition close to the nominal $x = 0.10$ composition $Pd_{0.91}Pt_{0.09}Te_2$. This sample, labeled #ptnom10res, was used for transport experiments only. EDX on the second sample showed a small Te excess and a very small Pt content ($< 0.4\%$). Its composition is $Pd_{0.97}Pt_{<0.004}Te_{2.03}$. This sample was used for transport, ac susceptibility and heat capacity measurements and it is labeled #ptnom10. We remark that the EDX determined compositions above each yield the average over a large part of the sample surface and are thus representative for the specific sample. The experimental results on the doped samples are compared with previous resistance, ac susceptibility and heat capacity data taken on a crystal with the stoichiometric 1:2 composition to within 0.5% as determined by EDX [44, 48]. In the following this sample is labelled #pdte2.

Resistance measurements were performed using the standard four point method in a Quantum Design Physical Property Measurement System (PPMS) down to 2.0 K. Data at lower temperatures were collected in a 3-He refrigerator (Heliox, Oxford Instruments) down to 0.3 K using a low frequency (16 Hz) ac-resistance bridge (Linear Research LR700). The ac susceptibility was measured in the Heliox with a custom-made coil set. Data were also taken with the LR700 bridge, operated at a driving field of 0.026 mT. The heat capacity was measured using the dual slope thermal relaxation calorimetry technique [104], using a home-built set-up, see Chapters 2 and 4, where each data point is the average of four dual slope measurements. The increase in temperature ΔT in the measurement of the heat capacity is always in between 1% and 1.6% of the bath temperature of the particular measurement. In the ac susceptibility and specific heat experiment the dc

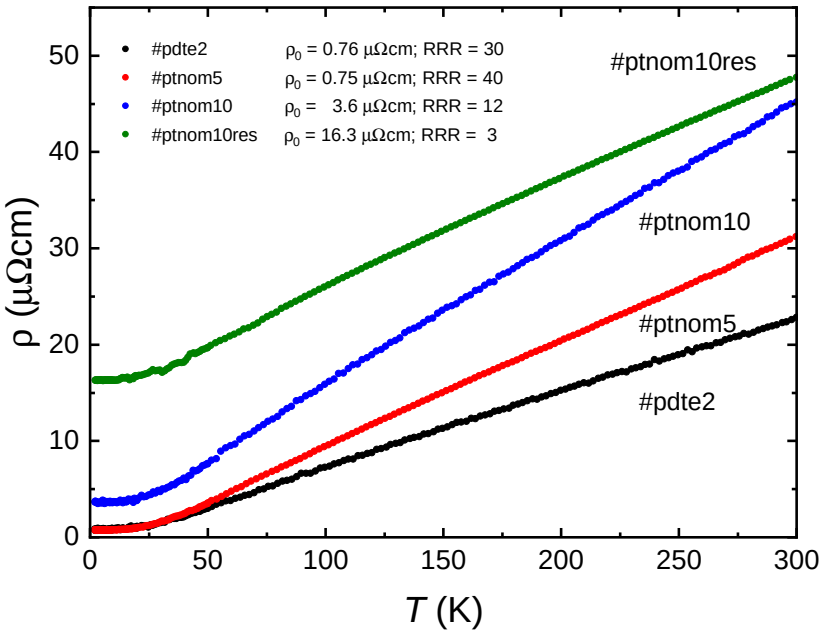

Figure 5.1: Temperature dependence of the resistivity of crystals #ptnom5 (red circles), #ptnom10 (blue circles) and #ptnom10res (green circles). The data for #pdte2 (black circles) are taken from Ref. [44].

magnetic field was applied in the ab plane. The demagnetization factor of the crystals is $N \simeq 0.1$, which implies the intermediate state is formed between $(1-N)H_c \simeq 0.9H_c$ and H_c in the case of type-I superconductivity. The resistance and ac susceptibility measurements in field have been carried out by applying the field above T_c and subsequently cooling in field, while the specific heat data in field were taken after zero field cooling and then applying the field.

5.3 Results

The resistivity of samples #ptnom5, #ptnom10 and #ptnom10res in the temperature range 2−300 K is shown in figure 5.1, where we have also traced the data for crystal #pdte2 reported in Ref. [44]. The curves for #ptnom5 and #pdte2 are very similar with a residual resistivity value, ρ_0, taken at 2 K, of 0.75 and 0.76 $\mu\Omega$cm, respectively. This is in agreement with both samples having the same stoichiometric 1:2 composition. The residual resistance ratio, RRR= $\rho(300\text{K})/\rho_0$, amounts to 40 and 30, respectively. For the non-stoichiometric sample #ptnom10 ρ_0 has increased to 3.6 $\mu\Omega$cm and RRR = 12. The ρ_0 value of the substituted sample #ptnom10res is considerably higher as expected, and equals 16.3 $\mu\Omega$cm. Its RRR is 3.

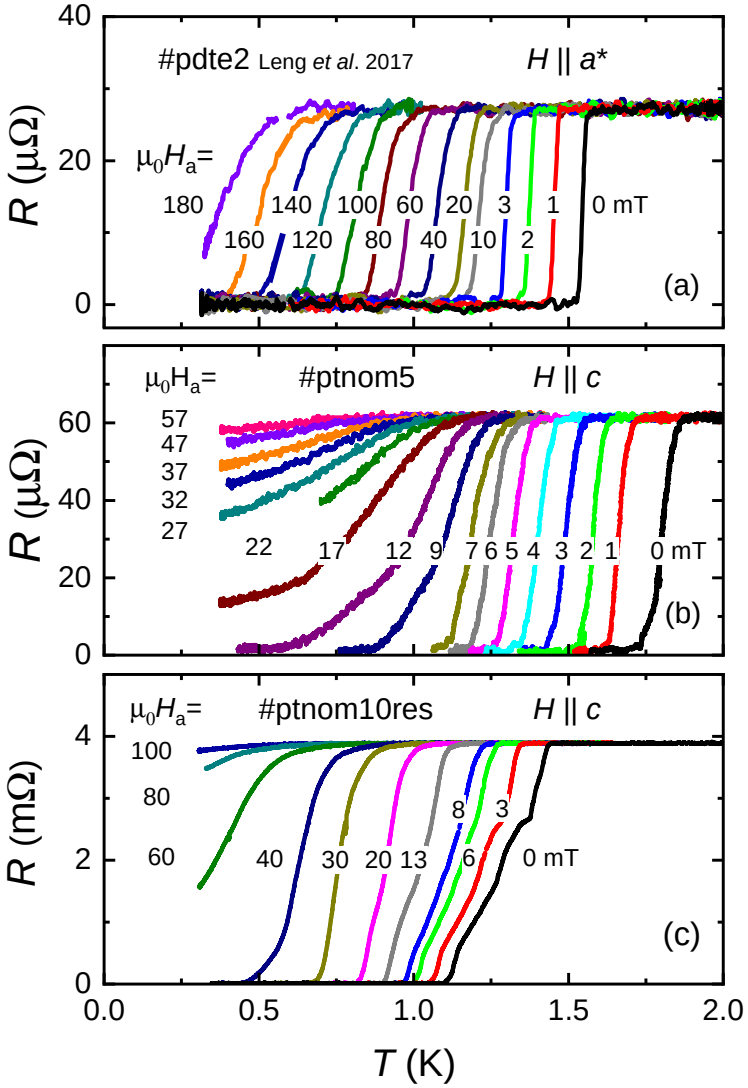

Figure 5.2: Resistance as a function of temperature around the superconducting transition for crystal #ptnom5 (panel (b)) and #ptnom10res (panel (c)) in zero field (black curves) and small applied fields, $\mu_0 H_a$, as indicated. The data in panel (a) for #pdte2 are taken from Ref. [44].

The resistance as a function of temperature around the superconducting transition in zero field and applied magnetic fields of crystals #ptnom5 and #ptnom10res is depicted in figure 5.2. Again, the data for #pdte2, shown in panel (a), are taken from Ref. [44]. The critical temperature in zero field, $T_c(0)$, here defined by the onset of the transition, is 1.87 K and 1.56 K for the stoichiometric samples #ptnom5 and #pdte2, respectively. Surprisingly, the higher T_c and RRR for #ptnom5 indicate it has a some-

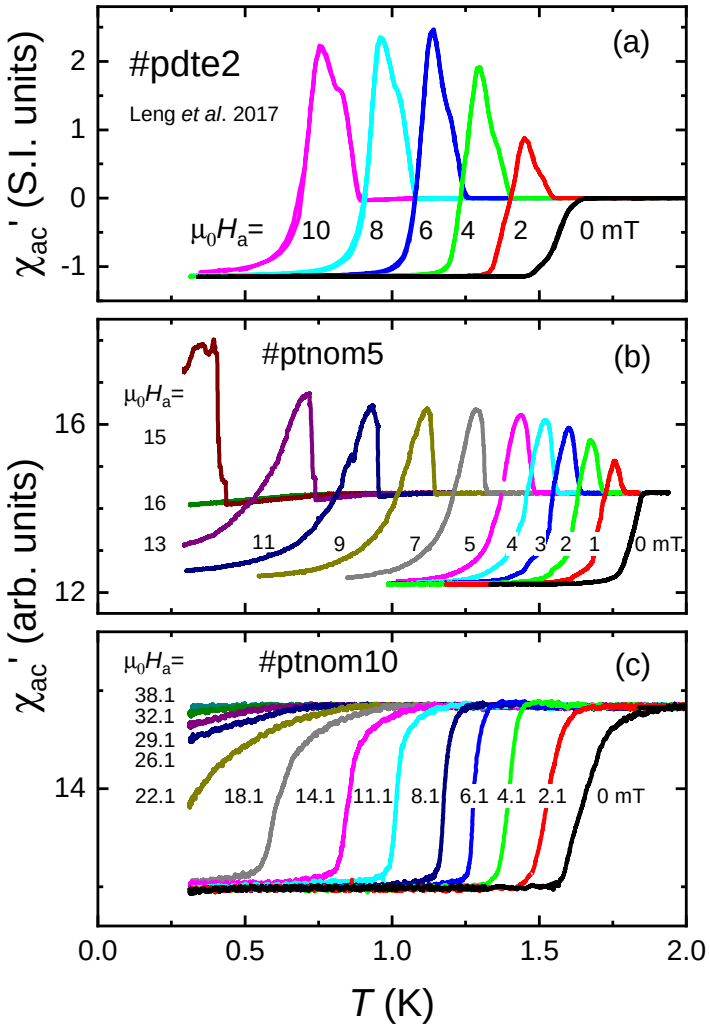

Figure 5.3: Ac susceptibility of crystals #ptnom5 (panel (b)) and #ptnom10 (panel (c)) measured in zero field (black curves) and small applied dc fields as indicated. The field is applied in the *ab* plane. The data of #pdte2 are taken from Ref. [44]. Note the ac driving field applied to take the data in panels (b) and (c) is a factor 10 smaller than in panel (a).

what higher purity than sample #pdte2. For the substituted sample the superconducting transition shows several steps and T_c is lower. It ranges from 1.44 to 1.12 K. In a magnetic field superconductivity is rapidly suppressed. The data in panels (b) and (c) of figure 5.2 show these crystals also have superconducting resistance paths in fields above the critical field $B_c(0)$ determined by ac susceptibility and heat capacity (see below and fig-

ure 5.5). The $B_c^R(0)$ values that can be deduced are however not as large as the value $B_c^R(0) \approx 0.3$ T for $H \parallel c$ reported for $PdTe_2$ (see figure S6 in the Supplemental Material file of Ref. [44]).

In figure 5.3 we show the in-phase component of the ac susceptibility, χ'_{ac}, in arbitrary units measured on crystals #ptnom5 and #ptnom10 in the temperature range 0.3−2.0 K. Again the data are compared with those of #pdte2 (data in SI units taken from Ref. [44]). The onset T_c values are 1.64 K and 1.85 K for #pdte2 and #ptnom5 and compare well to the values determined above from the resistivity. The onset T_c value for #ptnom10 is 1.91 K, but the transition is rather broad (the width is 0.3 K) with a slow decrease below T_c. The resistance of this sample was only measured in the PPMS down to 2.0 K. The RRR-value of 12 tells us the disorder is enhanced, which is also reflected in the broad transition. The $\chi'_{ac}(T)$ data measured in applied magnetic fields for #pdte2 and #ptnom5 show pronounced peaks below T_c that are due to the differential paramagnetic effect (DPE). The DPE is due to the positive dM/dH (M is the magnetization) in the intermediate state [79]. The intermediate phase is due to the sample shape and is present when the demagnetization factor, N, is finite. Observation of a DPE that largely exceeds the Meissner signal can therefore be used as solid proof for type-I superconductivity. Most importantly, the DPE is absent for crystal #ptnom10, which provides the first piece of evidence it is a type-II superconductor.

In figure 5.4 we show the electronic specific heat, C_{el}, of crystals #ptnom5 and #ptnom10 in the temperature range 0.3−2.0 K. The $C_{el}(T)$ curves are obtained by subtracting the phononic contribution from the measured C in the standard way, *i.e.,* by using the relation $C = \gamma T + \beta T^3$, where γ is the Sommerfeld coefficient and β the phonon coefficient. The data are compared with C_{el} of $PdTe_2$ reported in Ref. [48] and Chapter 4 of this thesis (panel (a) of figure 5.4). This $PdTe_2$ crystal was cut from the same batch as the samples studied in Ref. [44] and we also label it #pdte2. The onset T_c values of crystals #pdte2 and #ptnom5 are 1.62 K and 1.75 K and compare well to the values determined above. The onset $T_c = 1.60$ K for #ptnom10 is however lower than the value 1.91 K determined by $\chi'_{ac}(T)$.

The γ values of the three crystals in panels (a), (b) and (c) of figure 5.4 amount to 4.4, 4.5 and 4.7 mJ/mol K^2 and the β values are 0.7, 1.1 and 1.0 mJ/mol K^4, respectively. These γ values are very similar, which indicates the density of states near the Fermi level is not affected much by doping. The β values do show some variation, which is not correlated with the amount of disorder and likely related to an experimental uncertainty because of the small temperature interval in which β is obtained. To examine the strength of the electron-phonon coupling, the step size $\Delta C|_{T_c}$ is analysed

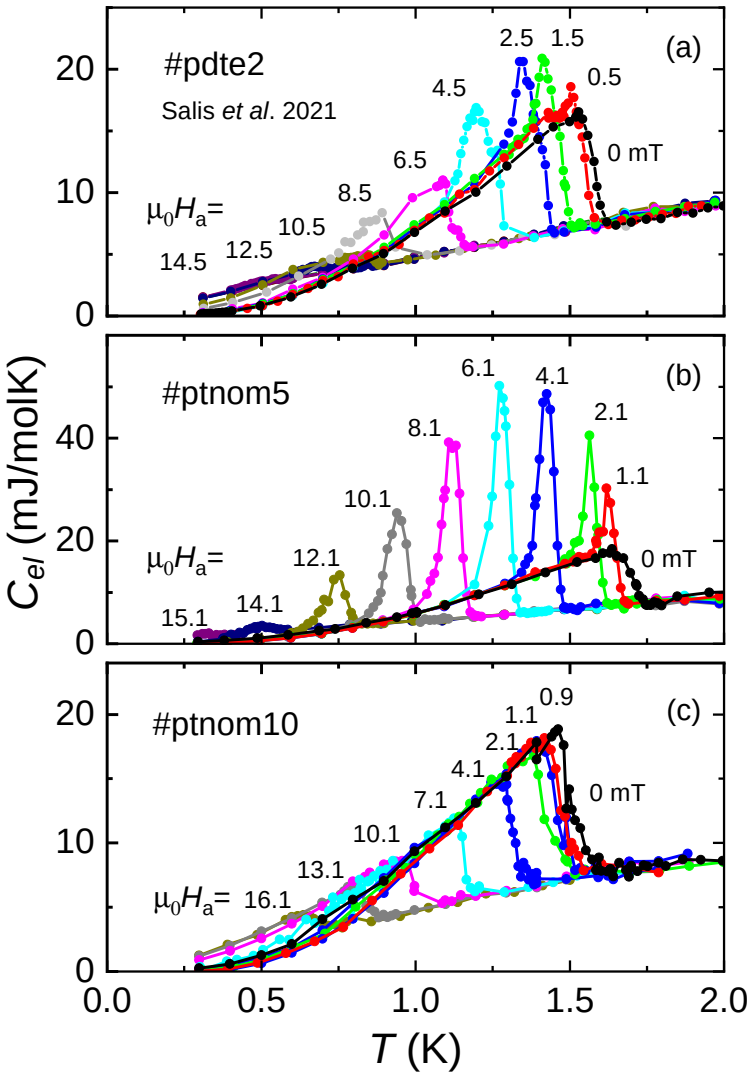

Figure 5.4: Electronic specific heat, C_{el}, of crystals #ptnom5 (panel (b)) and #ptnom10 (panel (c)) measured in zero field (black curves) and small applied dc fields as indicated. The field is directed in the *ab* plane. The data of #pdte2 are taken from Chapter 4.

using the BCS relation $\Delta C|_{T_c}/\gamma T_c = 1.43$, where T_c is the superconducting transition temperature, here taken as the onset of superconductivity. For crystal #pdte2 a ratio $\Delta C|_{T_c}/\gamma T_c = 1.42$ is found [48], which is close to the textbook value of 1.43 for a weakly coupled BCS superconductor. For crystal #ptnom5 a ratio of 1.41 is found, which presents a minute change from the textbook value. However, for crystal #ptnom10 we determine a ratio of 1.48, suggesting that superconductivity is slightly more than weakly coupled.

Next we discuss the electronic specific heat measured in applied magnetic fields (figure 5.4). Distinguishing between type-I and type-II superconductivity via heat capacity can be achieved by observing the presence or absence of latent heat. The extra energy necessary to facilitate a first-order phase transition is reflected in the heat capacity as an increased value of C at the transition. A type-I superconductor has a second-order phase transition in zero field, but a first-order one in field, while for a type-II superconductor the transition remains second-order in an applied field. The excess C_{el} above the standard BCS heat capacity in panel (a) provided solid thermodynamic evidence $PdTe_2$ is a type-I superconductor [48]. Surprisingly, for crystal #ptnom5 (panel b) the excess specific heat becomes more pronounced as illustrated by the sharp peaks below $T_c(B)$. Thus the contribution of the latent heat to C_{el} is much larger, which indicates the transition has a stronger first-order character than observed for crystal #pdte2. On the other hand, for crystal #ptnom10 the data in panel (c) show latent heat is absent, which provides the second piece of evidence of type-II superconductivity, in line with the χ'_{ac} data.

Finally, we trace the temperature variation of the critical field, $B_c(T)$, extracted from the ac susceptibility (figure 5.3) and specific heat data (figure 5.4). The $B-T$ phase diagram is reported in figure 5.5. For crystals #pdte2 and #ptnom5 we identify $T_c(B)$ by the onset in C_{el} and the onset of the DPE in $\chi'_{ac}(T)$. $B_c(T)$ follows the standard BCS quadratic temperature variation $B_c(T) = B_c(0)[1-(T/T_c)^2]$, with $B_c(0) = 14.2$ mT and $T_c = 1.63$ K for #ptpde2 [44, 48], and $B_c(0) = 15.9$ mT and $T_c = 1.77$ K for #ptnom5. For crystal #ptnom10 the transition in $\chi'_{ac}(T)$ is rather broad. Here we identify T_c by the onset temperature in C_{el}, which corresponds to the temperature where the magnetic transition is complete in $\chi'_{ac}(T)$. The $B-T$ phase line provides further evidence for type-II superconductivity. It compares well to the Werthamer-Helfand-Hohenberg (WHH) model curve [115] for an orbital-limited weak-coupling spin-singlet superconductor with an upper critical field $B_{c2}(0) = 21.8$ mT.

5.4 Discussion

From the sample preparation side our goal was to prepare $Pd_{1-x}Pt_xTe_2$ crystals with $x = 0.05$ and $x = 0.10$. The SEM/EDX micrographs showed that Pt did not dissolve as expected in these crystals and that the single-crystalline batches are inhomogeneous. Crystals cut from the nominal $x = 0.05$ batch appeared to be undoped and have the 1:2 stoichiometry. From the nominal $x = 0.10$ batch we managed to obtain a crystal with $x = 0.09$ and a non-stoichiometric crystal $Pd_{0.97}Pt_{<0.004}Te_{2.03}$. Specific heat and ac-

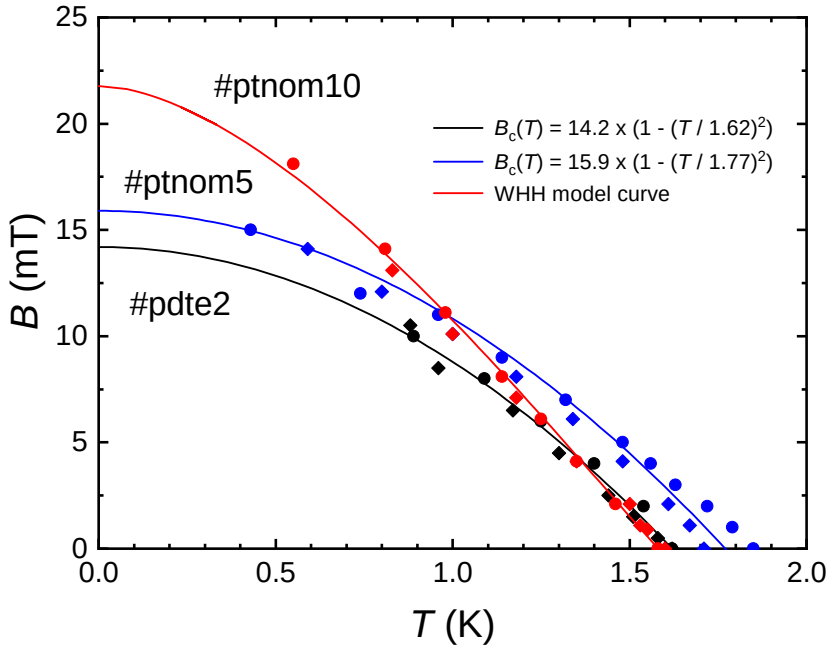

Figure 5.5: Critical field $B_c(T)$ of crystal #pdte2 and #ptnom5 and upper critical field $B_{c2}(T)$ of crystal #ptnom10 extracted from the specific heat (closed squares) and ac susceptibility (closed circles) data.

susceptibility measurements on this last crystal #ptnom10 demonstrated we could make a doping-induced transition to type-II superconductivity.

To observe type-II superconductivity the disorder should be large enough such that the threshold $\kappa = 1/\sqrt{2}$ can be overcome. The effect of controlled non-magnetic disorder on the normal and superconducting properties of $PdTe_2$ was recently studied by electron irradiation by Timmons *et al.* [116]. The residual resistivity was found to increase from a pristine crystal value of 0.6 $\mu\Omega$cm to 2.4 $\mu\Omega$cm for an irradiation dose of 2.4 C/cm^2, while at the same time T_c decreased from 1.76 K to 1.65 K as identified by reaching the zero resistance state $R = 0$. Assuming a linear relation between ρ_0 and T_c, T_c decreases at a rate of 0.046 K/$\mu\Omega$cm. With this rate we estimate for crystal #ptnom10res ($\Delta\rho_0 = 15.5$ $\mu\Omega$cm) $T_c = 0.9$ K, which compares favorably to the measured $T_c = 1.1$ K ($R = 0$), given the crude approximation. In this electron irradiation work no discussion was made whether disorder is strong enough to induce type-II behaviour.

For crystal #ptnom10 the coherence length ξ can be calculated from the relation $B_{c2}(0) = \Phi_0/2\pi\xi^2$, where Φ_0 is the flux quantum. From figure 5.5 we determine $B_{c2}(0) = 21.8$ mT and obtain $\xi = 123$ nm. The coherence

length can be related to the electron mean free path, l_e, via Pippard's relation $1/\xi = 1/\xi_0 + 1/l_e$, where ξ_0 is the intrinsic coherence length given by the BCS value [117]. With $\xi_0 = 1.8$ μm [46] and $\xi =$ 123 nm we obtain $l_e = 132$ nm. As expected, this value is reduced compared to $l_e = 531$ nm calculated from the residual resistivity value $\rho_0 = 0.76$ $\mu\Omega$cm [46] of nominally pure $PdTe_2$. Reversely, using the experimental value $\rho_0 = 3.6$ $\mu\Omega$cm (figure 5.1) we calculate $l_e = 112$ nm for crystal #ptnom10, which is close to the value $l_e = 132$ nm derived from Pippard's relation.

Next we calculate $\kappa = \lambda/\xi$ of crystal #ptnom10. In their controlled disorder study Timmons *et al.* [116] measured the penetration depth and found that upon increasing the disorder λ stays nearly constant [116] at a value of 220 nm. This is in line with the minute change in the γ value reported above. With $\xi = 123$ nm we calculate $\kappa = 1.8$, which is in agreement with superconductivity being of the second kind. For crystals #pdte2 and #ptnom5 we calculate $\kappa \simeq 0.5$-0.6 [44]. Here $\xi \simeq 440$-370 nm is estimated from the GL relation $\xi = \Phi_0/(2\sqrt{2}\pi B_c \lambda_L)$ [117], where $\lambda_L \propto (m_e/n_s)^{1/2}$ is the London penetration depth with m_e the effective electron mass and n_s the superfluid density.

Another way to provide an estimate of κ of crystal #ptnom10 is from the GL relation $\kappa = B_{c2}/\sqrt{2}B_c$. The thermodynamic critical field, B_c, can be determined from the specific heat by the relation $\Delta C|_{T_c} = 4B_c(0)^2/\mu_0 T_c$ [78], where C is in units of J/m^3. From $\Delta C|_{T_c}$ in figure 5.4 (panel (c)) we calculate $B_c(0) = 11.1$ mT. We remark this value is close to the calculated value $B_c(0) = 12.6$ mT reported for $PdTe_2$ [44]. Using $B_c(0) = 11.1$ mT and $B_{c2} = 21.8$ mT in the expression above, we calculate $\kappa = 1.4$, which is similar to the value of 1.8 directly estimated from the ratio λ/ξ. We remark that for type-I superconductivity $B_c(0)$ can also be obtained from the latent heat with help of the Clausius-Clapeyron relation. We calculate $B_c(0) =$ 11.2 mT and 11.1 mT as shown in the appendix for #pdte2 and #ptnom5, respectively, in good agreement with the values obtained from $\Delta C|_{T_c}$ in zero field.

Our results are of relevance for the observation of a mixed type-I and type-II superconducting state in $PdTe_2$ probed by surface sensitive techniques [49, 50, 111]. Our doping study shows that nominal pure $PdTe_2$ crystals can already be close to the type-I/II border. Using the value $\lambda = 230$ nm [116], we calculate $\xi = 310$ nm at the threshold value $\kappa = 1/\sqrt{2}$. This implies l_e should be smaller than 375 nm for type-II superconductivity, or $\rho_0 > 1.4$ $\mu\Omega$cm. From the resistivity graph reported in Ref. [49] we deduce $\rho_0 \simeq 1$ $\mu\Omega$cm, which indeed is not far from the type-I/II border. Thus it is plausible inhomogeneities give rise to the mixed phase observation reported in Refs. [49, 50, 111].

An unsolved aspect of superconductivity in $PdTe_2$ is the observation of surface superconductivity detected in the screening signal $\chi'_{ac}(T)$ measured in small applied dc fields [44, 101]. The extracted surface critical field $B_c^S(0) = 34.9$ mT exceeds the value predicted by the Saint-James-de Gennes model [96] $B_{c3} = 2.39 \times \kappa B_c = 16.3$ mT. Recently, the Ginzburg-Landau model at the superconducting-insulator boundary was revisited [118] and it was shown that T_c and the third critical field B_{c3} can be enhanced to exceed the Saint-James-de Gennes value, which is worth exploring further. On the other hand, it is tempting to attribute the surface superconductivity in $PdTe_2$ to superconductivity of the topological surface state detected by ARPES [39, 94, 41, 42, 43]. We remark that the $\chi'_{ac}(T)$ data for the doped crystals, reported in figures 5.3 (b) and 5.3(c), also show superconducting screening signals above the $B_c(0)$ and $B_{c2}(0)$ values reported in figure 5.5. Likewise, the resistance traces in figure 5.2 reveal $B_c^R(0)$ is similarly enhanced. These screening signals of enhanced superconductivity are however not as pronounced as reported for $PdTe_2$ in Ref. [44]. Nonetheless, the robustness of superconducting screening signals above $B_c(0)$ or $B_{c2}(0)$ upon doping, as well as under high pressure [101], calls for further experiments.

5.5 Conclusion

The Dirac semimetal $PdTe_2$ is a type-I superconductor with $T_c = 1.7$ K. We have carried out a doping study directed to intentionally increase the disorder and induce type-II superconductivity. Two single-crystalline batches $Pd_{1-x}Pt_xTe_2$ have been prepared with nominal doping concentrations $x = 0.05$ and $x = 0.10$. Sample characterization by energy dispersive x-ray spectroscopy (EDX) on small crystals cut from the batches revealed that Pt did not dissolve homogeneously in the crystals. In fact the nominal $x = 0.05$ crystal appeared to be undoped and have the stoichiometric 1:2 composition. From the nominal $x = 0.10$ batch we obtained a small single crystal with $x = 0.09$, as well as a crystal with the non stoichiometric composition $Pd_{0.97}Pt_{<0.004}Te_{2.03}$. The presence of the differential paramagnetic effect in the ac susceptibility and latent heat in the heat capacity demonstrate the nominal $x = 0.05$ crystal is a type-I superconductor, just like $PdTe_2$. The absence of these effects for $Pd_{0.97}Pt_{<0.004}Te_{2.03}$ revealed it is a type-II superconductor with an upper critical field $B_{c2} = 21.8$ mT. The analysis of B_{c2} and resistance data using Pippard's model convincingly show $PdTe_2$ can be turned into a superconductor of the second kind when the residual resistivity $\rho_0 > 1.4$ $\mu\Omega$cm.

5.6 Appendix

5.6.1 SEM-EDX microscopy

Scanning electron microscopy with energy dispersive x-ray spectroscopy (SEM/EDX) was carried out with help of a Hitachi table top microscope TM3000. The acceleration voltage in all measurements is 15 kV. Of each single-crystalline boule prepared with a certain nominal Pt content small thin crystals were isolated with typical size 2×3 mm^2. On each of these crystals we have investigated the composition by EDX in several areas of typically 200×200 μm^2. Overall the composition in the selected and measured crystals was found to be homogeneous. The table below gives the labels of the doped crystals, the nominal Pt content and the EDX determined composition.

Crystal	Nominal Pt cotent	EDX compostion
#ptnom5	5 at. %	$PdTe_2$
#ptnom10	10 at. %	$Pd_{0.97}Pt_{<0.004}Te_{2.03}$
#ptnom10res	10 at.%	$Pd_{0.91}Pt_{0.09}Te_2$

Typical SEM/EDX results for crystals #ptnom5, #ptnom10 and #ptnom10res are given in figures 5.6, 5.7 and 5.8 respectively. Shown are:

Top panel: The SEM spectrum in cps/eV (counts per second per electronvolt) with Pd, Pt and Te peaks labelled.
Middle panel: Table with quantitative results of the composition analysis.
Lower left panel: SEM picture of the crystal with scanned area for the composition analysis indicated.
Lower right panel: Pd, Pt and Te element distribution in the scanned area.

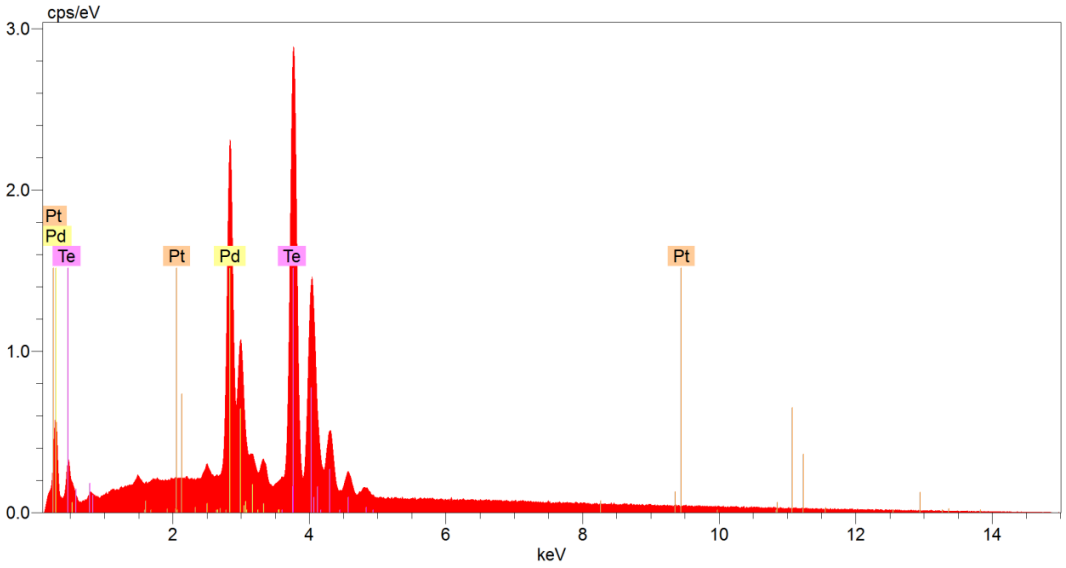

Map Date:23/06/2021 17:08:53 HV:15.0kV Puls th.:2.55kcps

El	AN	Series	unn. C [wt.%]	norm. C [wt.%]	Atom. C [at.%]	Error [%]
Te	52	L-series	69.25	70.63	66.73	2.1
Pd	46	L-series	28.80	29.37	33.27	0.9
Pt	78	M-series	0.00	0.00	0.00	0.0
		Total:	98.05	100.00	100.00	

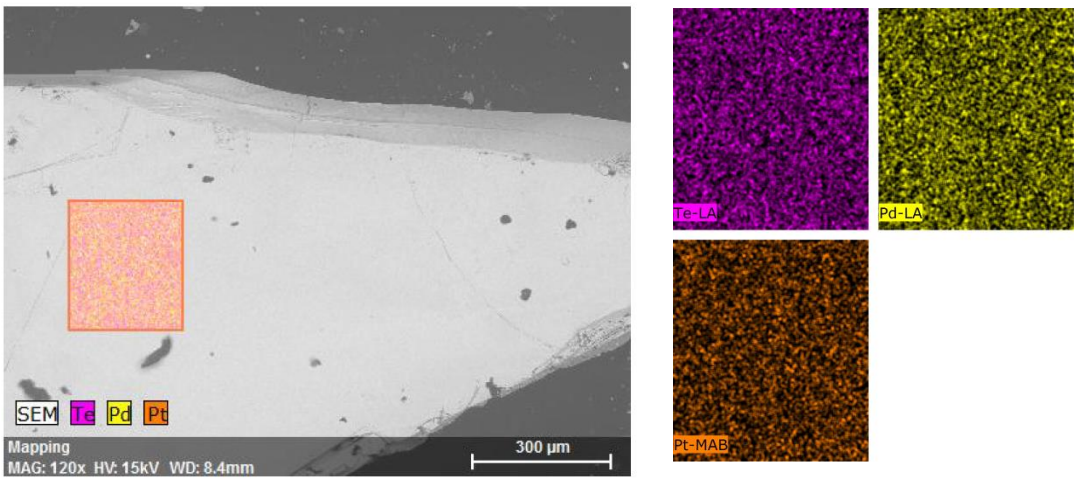

Figure 5.6: SEM/EDX mapping of crystal #ptnom5.

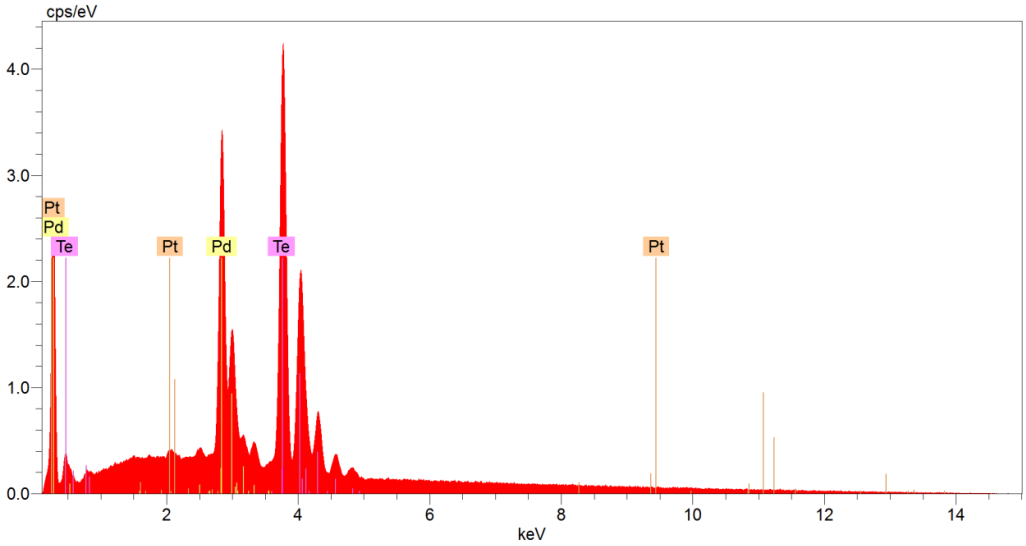

Map Date:23/06/2021 17:19:51 HV:15.0kV Puls th.:3.98kcps

El	AN	Series	unn. C [wt.%]	norm. C [wt.%]	Atom. C [at.%]	Error [%]
Te	52	L-series	61.08	71.18	67.39	1.8
Pd	46	L-series	24.54	28.60	32.47	0.8
Pt	78	M-series	0.19	0.22	0.14	0.0
		Total:	85.81	100.00	100.00	

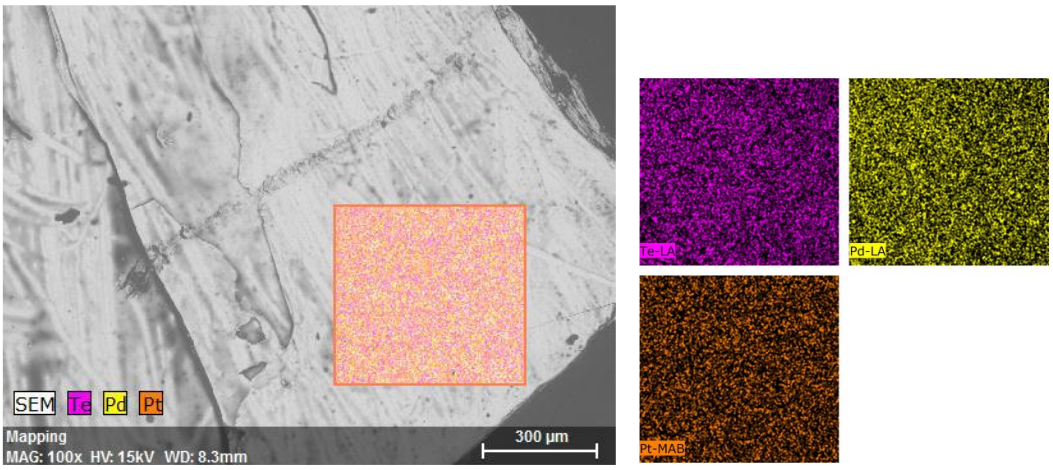

Figure 5.7: SEM/EDX mapping of crystal #ptnom10.

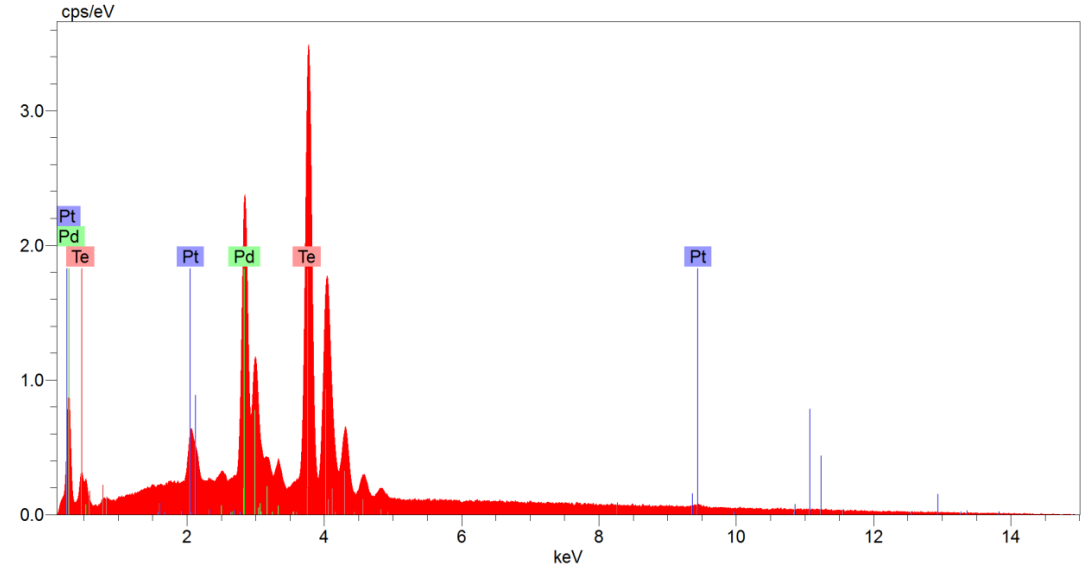

Map Date:29/06/2021 17:20:08 HV:15.0kV Puls th.:3.44kcps

El	AN	Series	unn. C [wt.%]	norm. C [wt.%]	Atom. C [at.%]	Error [%]
Te	52	L-series	63.72	70.01	68.02	1.9
Pd	46	L-series	22.22	24.42	28.44	0.7
Pt	78	M-series	5.07	5.58	3.54	0.2
		Total:	91.01	100.00	100.00	

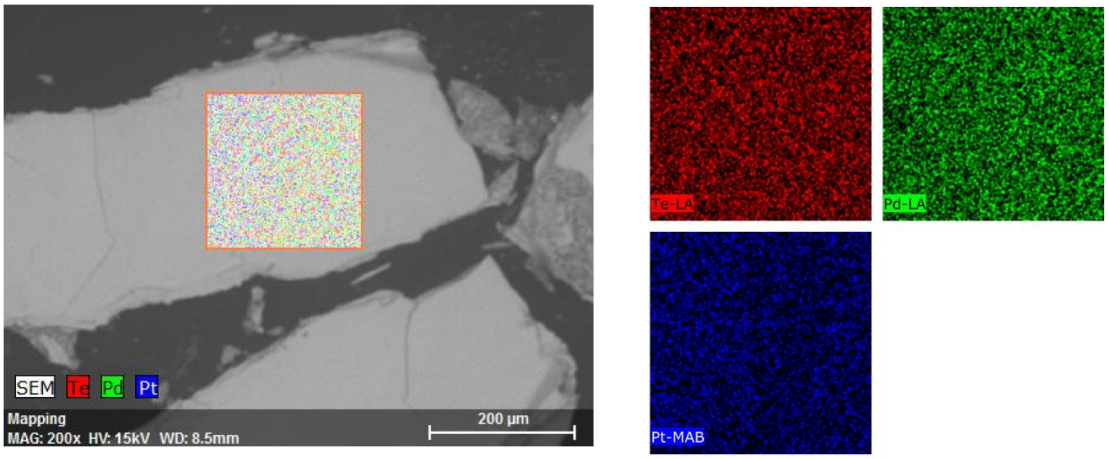

Figure 5.8: SEM/EDX mapping of crystal #ptnom10res.

5.6.2 Latent heat

As mentioned in the Discussion section an estimate for the thermodynamic critical field $B_c(0)$ can be obtained by evaluating the relation $\Delta C = 4B_c(0)^2/\mu_0 T_c$, where ΔC is the step at T_c in the specific heat at $B = 0$. Alternatively, for a type-I superconductor in a magnetic field $B_c(0)$ can be calculated from the latent heat, L. Using the Clausius-Clapeyron equation the entropy change is given by $\Delta S = L(T)/T = -2\mu_0 B_c(T)\frac{dB_c(T)}{dT}$, with $B_c(T) = B_c(0)(1-(T/T_c)^2)$. ΔS was calculated by graphically integrating the C/T data in field and subtracting the data taken at $B = 0$. This procedure is carried out for all applied field values, and from $\Delta S(B)$ we obtain $B_c(0)$ as a fit parameter. For crystals #pdte2 and #ptnom5, that exhibit type-I superconductivity we obtain $B_c(0) = 11.2$ mT and 11.1 mT, respectively. We remark these values are close to the $B_c(0)$ values evaluated at $B = 0$. On the other hand, the $B_c(0)$ values derived from ΔC and ΔS are smaller than the value derived directly from the experiment. In the table below we compare the $B_c(0)$ values obtained in different ways.

Crystal	$B_c(0)$ from ΔC	$B_c(0)$ from ΔS	$B_c(0)$ experiment
#pdte2	10.9 mT	11.2 mT	14.2 mT
#ptnom5	11.8 mT	11.1 mT	15.9 mT
#ptnom10	11.1 mT	-	-

Chapter 6

Anisotropic upper critical field of the layered superconductor $\mathbf{LaO_{0.8}F_{0.2}BiS_{2-}}_x\mathbf{Se}_x$ ($x = 0.5$ and 1.0)

The breaking of local inversion symmetry in $BiCh_2$ compounds leads to exotic physical properties that attract considerable interest. Here, the focus is on the effects of the Rashba-type spin-orbit coupling manifested in the superconducting properties of these systems. We report the results of a study on the angular variation of the upper critical field $B_{c2}(\theta)$ of $LaO_{0.8}F_{0.2}BiS_{2-x}Se_x$ ($x = 0.5$ and 1.0) at temperatures down to 0.3 K. The upper critical field is strongly anisotropic and attains exceptionally large value when the field is applied parallel to the layers. This value significantly exceeds the orbital and paramagnetic pair breaking limits. This suggests a strong enhancement of superconductivity that is mediated by the unique effects of the local inversion symmetry breaking.

6.1 Introduction

Superconductivity in $REOBiCh_2$ (RE = rare earth, Ch = chalcogenide) layered compounds was first uncovered and reported in 2012 [119, 120, 121, 122, 123]. The parent phase is a semiconductor with a direct bandgap of 0.84 eV [124]. By substituting F on the O sites metallicity and superconductivity at low temperatures are induced. The structure consists of $BiCh_2$ conducting bi-layers vertically enclosed by REO blocking layers. Due to the resemblance of the structure to that of cuprate [125] and iron-pnictide [126] systems, speculation on and predictions of double-digit superconducting transition temperatures and unconventional superconductivity in $BiCh_2$ based systems followed [127, 128]. These developments resulted in a concerted effort in the synthesis of materials and experimental and theoretical work on uncovering the mechanism mediating superconductivity in $REOBiCh_2$ materials. Notably, the case of conventional s-wave paring has been investigated in detail. From theoretical predictions the pairing mechanism can be fully electron-phonon mediated [129, 130]. Results from penetration depth measurements carried out with the tunnel diode oscillator technique [131] suggest strongly coupled s-wave superconductivity as reported for a single crystal of $NdO_{1-x}F_xBiS_2$ with a superconducting gap $\Delta_0 = 2.15\ k_BT_c$ [132]. Thermal conductivity data taken on a single crystal of $NdO_{0.71}F_{0.29}BiS_2$ indicate a conventional fully gapped state which is further corroborated by the observation of the robustness of the superconducting state to non-magnetic impurities [133, 90]. Measurements of the low-temperature heat capacity [134] of single-crystalline $LaO_{0.5}F_{0.5}BiSSe$ indicate strongly coupled full-gap superconductivity with $\Delta_0 = 2.25\ k_BT_c$. To induce an isotope effect which should alter T_c according to $T_c^{-\alpha}$ with $\alpha \sim 0.5$ [135] if the system is of conventional nature, multiple isotope studies have been carried out. The high pressure phase of $Sr_{1-x}La_xFBiS_2$ with $x = 0.36 - 0.38$ was investigated by substituting S isotopes [136]. Here $\alpha \sim 0.7$ was found indicative of phonon mediated superconductivity. An unchanging T_c was found for $LaO_{0.6}F_{0.4}BiS_{2-x}Se_x$ with $x = 1.09 - 1.14$ with ^{76}Se and ^{80}Se isotopes giving $\alpha \sim 0$ possibily indicating superconductivity is not mediated by phonons [137].

Another interesting observation in $REOBiCh_2$ systems is the breaking of the rotational symmetry in the upper critical field B_{c2} [138]. Similar to the observations of electronic nematicity in high-temperature superconductors [139, 140, 141] and nematic superconductivity in the candidate topological superconductor family of doped Bi_2Se_3 compounds [30, 28, 31, 54, 142, 143], an unforeseen anisotropy in B_{c2} has been detected. In some of the $REOBiCh_2$ systems the four-fold symmetry expected from the tetragonal lattice symmetry is not represented in the two-fold symmetry of the superconducting state. In this situation the maximum of $B_{c2}(\theta)$ exceeds the

Pauli-limit by a considerable degree [138, 144, 145], reminiscent of triplet superconductivity in uranium compounds [146, 147, 148]. In the case of $REOBiCh_2$ systems a possible explanation for the extremely large B_{c2} comes from Rashba-type spin-orbit coupling. In these systems the $BiCh_2$ layers are proposed to have a local inversion symmetry breaking allowing for the generation of Rashba-type spin-orbit coupling [149]. This unique Rashba-type spin-orbit coupling could lead to an enhancement of B_{c2} [150]. While the $REOBiCh_2$ systems do posses global inversion symmetry, it is the local inversion symmetry breaking that induces a spin polarisation. This has been confirmed by the observation of Rashba spin polarisation in spin angle resolved photoemission spectroscopy (S-ARPES) [151]. This unique spin texture would suppress the orbital pair breaking effect and the Pauli-paramagnetic pair breaking effect by locking the spin polarisation onto the *ab*-plane. In this manner a large B_{c2} can be manifested for configurations with $B \parallel ab$. The confirmation of a B_{c2} that is significantly larger than what is expected from the two aforementioned pair breaking effects [138, 145] makes systems in the $REOBiCh_2$ family a fruitful playground for the investigation of the effects of local inversion symmetry breaking on superconductivity.

In this chapter the results of a rotational study of the upper critical field $B_{c2}(\theta)$ of $LaO_{0.8}F_{0.2}BiS_{2-x}Se_x$ ($x = 0.5$ and 1.0) are presented. This study is an extension of the work reported in Ref. [145] where single crystals of $LaO_{0.8}F_{0.2}BiS_{2-x}Se_x$ ($x = 0.22$ and 0.69) were investigated at temperatures down to 1.8 K. The angular variation of B_{c2} with respect to the magnetic field confirms a strong anisotropy. Furthermore, the maximum in B_{c2} significantly exceeds the expected value from the Pauli limit and the orbital limit from the Werthamer-Helfland-Hohenberg (WHH) formalism.

6.2 Experimental

$LaO_{0.8}F_{0.2}BiS_{2-x}Se_x$ crystallises in the tetragonal ZrCuSiAs structure with space group P4/nmm with the exception of F-free systems [152]. The crystal structure is comprised of $BiCh_2$ conducting bilayers that are vertically enclosed by REO blocking layers resembling the cuprate and iron-pnictide structures, see figure 6.1. The single crystals of $LaO_{0.8}F_{0.2}BiS_{2-x}Se_x$ ($x = 0.5$ and 1.0) that were used in this study originate from two batches synthesised using the flux method [145]. The stoichiometric composition was confirmed to be consistent with the nominal composition by energy dispersive X-ray spectroscopy. Samples used in the experiments were chosen from the two batches and have a typical size of $1 \times 1 \times 0.1$ mm^3.

Resistance measurements were performed using the standard four-terminal method. All measurements have been carried out with the current flowing

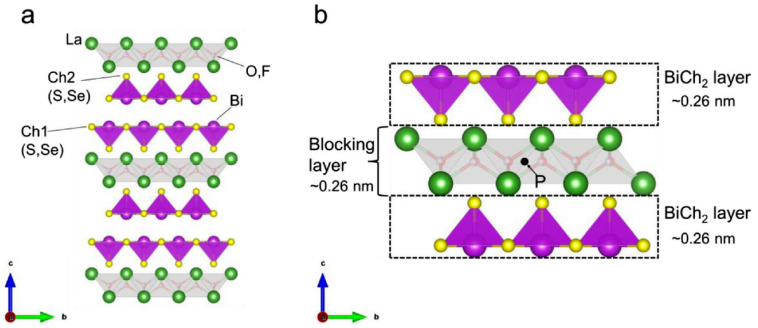

Figure 6.1: Crystal structure of $LaO_{0.8}F_{0.2}BiS_{2-x}Se_x$. (a) Crystal structure with space group P4/nmm. (b) LaO blocking layer surrounded by $BiCh_2$ conduction layers. Image adopted from [145].

in the *ab*-plane giving the in-plane resistance. Measurements down to 2.0 K have been carried out in a Quantum Design Physical Property Measurement System (PPMS). Temperatures down to 0.3 K were reached using a 3-He refrigerator (Heliox, Oxford Instruments). The resistance was measured using an ac-resistance bridge (Linear Research LR700) with an excitation frequency of 16 Hz. Magnetic fields up to 12 T were applied. To study the rotational anisotropy of the upper critical field below 2 K the sample was placed on a rotator platform attached to an Attocube ANRv51 stepper-motor rotator controlled by an ANC350 motion controller. Rotations cause a large energy dissipation, such that during each rotation the sample warms up to $T > T_c$. Furthermore, the readout-value of the platform angle becomes dependent on temperature below 2.5 K. We therefore calibrated the angle to a set of data obtained previously on the same sample in the PPMS at higher temperatures, using the known anisotropic behaviour of B_{c2}.

6.3 Results and discussion

The resistance of $LaO_{0.8}F_{0.2}BiSSe$ and $LaO_{0.8}F_{0.2}BiS_{1.5}Se_{0.5}$ around the superconducting transition is presented in figure 6.2. A smooth transition is observed for $LaO_{0.8}F_{0.2}BiS_{1.5}Se_{0.5}$ as opposed to that of $LaO_{0.8}F_{0.2}BiSSe$. The transition temperature T_c is determined by the $R = 0$ criterion. This is done by extrapolating $R(T)$ in the superconducting transition linearly to the $R = 0$ value on the x axis as shown in figure 6.2. This gives $T_c = 2.7$ K and 2.9 K for $LaO_{0.8}F_{0.2}BiSSe$ and $LaO_{0.8}F_{0.2}BiS_{1.5}Se_{0.5}$, respectively. Taking either the onset of superconductivity or the 50 % resistance value a higher T_c can be deduced for $LaO_{0.8}F_{0.2}BiSSe$ than for $LaO_{0.8}F_{0.2}BiS_{1.5}Se_{0.5}$. This higher T_c does correlate with the higher Se content as expected [153].

Figure 6.3 shows the in-plane resistance as a function of magnetic field

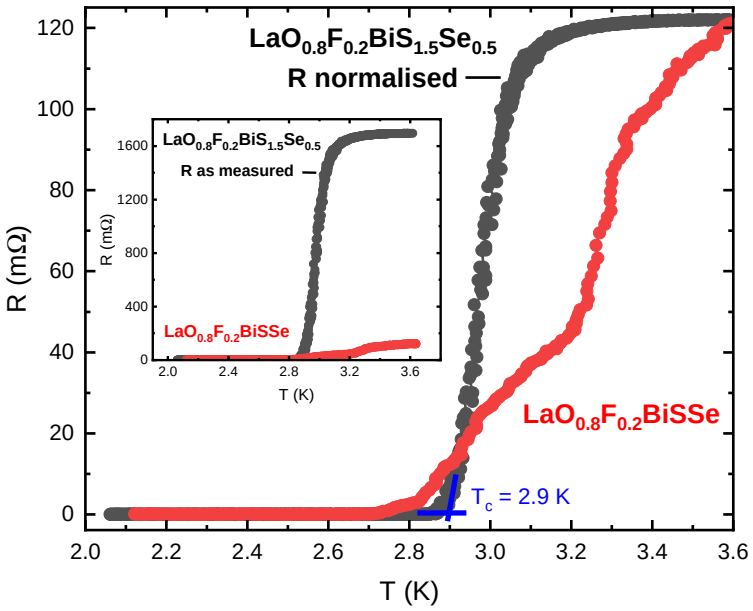

Figure 6.2: Superconducting transition in zero field of $LaO_{0.8}F_{0.2}BiSSe$ and $LaO_{0.8}F_{0.2}BiS_{1.5}Se_{0.5}$. The resistance of $LaO_{0.8}F_{0.2}BiS_{1.5}Se_{0.5}$ is normalised against the resistance of $LaO_{0.8}F_{0.2}BiSSe$ for comparative purposes. The determination of the $R = 0$ criterion is shown by the solid blue lines. Inset: Zero field resistance as measured.

strength at temperatures of 0.3, 0.9 and 1.4 K for $LaO_{0.8}F_{0.2}BiSSe$ and $LaO_{0.8}F_{0.2}BiS_{1.5}Se_{0.5}$. Here θ is the angle between the ab-plane of the crystal and the magnetic field direction and is defined such that $\theta = 0°$ and $90°$ for $B \perp ab$ and $B \parallel ab$, respectively. The electrical current is directed parallel to the field for $B \parallel ab$ and perpendicular for $B \perp ab$, respectively. Data at $T = 0.4$ K, 0.9 K and 1.4 K are shown for $LaO_{0.8}F_{0.2}BiSSe$ in figure 6.3 (a), (b) and (c), respectively, for angles between $-4.5°$ and $111.3°$. Pronounced differences in the suppression of the superconducting state for different angles are observed. For angles close to $B \perp ab$, the superconducting state is readily suppressed for $B < 2$ T, whereas the superconducting state persists above 12 T for angles close to $B \parallel ab$. The presence of several steps in the superconducting transition resembling multiple transitions is puzzling. Rather than due to an impurity phase, it is more likely related to a small angle mismatch between the layers of the crystal. This possibility is reflected in the data by the consistent variation of the transitions with the angle. For angles close to $B \perp ab$ the field strength difference between the superconducting steps is small, while the field strength difference between the steps is the greatest near $B \parallel ab$ where slight changes in the angle drastically alter B_{c2}. Instead of the midpoint transition criterion used to determine T_c [145], we have opted to use the $R = 0$ criterion to mitigate the

ambiguity caused by the presence of multiple superconducting transitions. Taking the $R = 0$ point as T_c also improves consistency due to the lack of large enough fields to suppress superconductivity enough to reach the mid-point value in the low-temperature range for angles near $B \parallel ab$.

Figures 6.3 (d), (e) and (f) depict the angular variation of the resistance of $LaO_{0.8}F_{0.2}BiS_{1.5}Se_{0.5}$ between $-10.5°$ and $100.0°$ at 0.3 K, 0.9 K and 1.4 K, respectively. The angular variation in B_{c2} of $LaO_{0.8}F_{0.2}BiS_{1.5}Se_{0.5}$ shows a similar trend as that of $LaO_{0.8}F_{0.2}BiSSe$ where relatively easily suppressible superconductivity is observed for angles close to $B \perp ab$ and more robust superconductivity is observed for angles close to $B \parallel ab$. Here the angle mismatch between layers resulting in the appearance of multiple superconducting phases is absent.

To further analyse the angular dependence of $LaO_{0.8}F_{0.2}BiSSe$ and $LaO_{0.8}F_{0.2}BiS_{1.5}Se_{0.5}$, B_{c2} has been determined according to the $R = 0$ criterium for all measured angles. The B_{c2} data of $LaO_{0.8}F_{0.2}BiSSe$ and $LaO_{0.8}F_{0.2}BiS_{1.5}Se_{0.5}$ at T = 0.3 K, 0.9 K and 1.4 K are given in figures 6.4 (a) - (f). In the insets the angular variation between 80° and 100° is presented.

To determine the nature of the anisotropy in B_{c2} we have opted to compare the data to the 3D anisotropic mass Ginzburg-Landau (GL) model and the 2D Tinkham model. Whereas the 3D GL model describes 3D superconductors with strong anisotropy originating from the effective mass, the 2D Tinkham is used to describe 2D (thin film) superconductors. The angle variation of $B_{c2}(\theta)$ in the 3D GL model [86] and in the 2D Tinkham model [87] is given by:

$$\text{3D GL:} \quad \left(\frac{B_{c2}(\theta)\cos(\theta)}{B_{c2}^{\perp}}\right)^2 + \left(\frac{B_{c2}(\theta)\sin(\theta)}{B_{c2}^{||}}\right)^2 = 1$$

$$\text{2D Tinkham:} \quad \left|\frac{B_{c2}(\theta)\cos(\theta)}{B_{c2}^{\perp}}\right| + \left(\frac{B_{c2}(\theta)\sin(\theta)}{B_{c2}^{||}}\right)^2 = 1.$$

Here $B_{c2}^{\perp}$ is the magnetic field perpendicular to the layers (*i.e.,* the *ab*-plane) and $B_{c2}^{||}$ is the magnetic field parallel to the layer. The blue dots in the insets of figure 6.4 represent the data, the green dashed lines represent the 2D Tinkham model and the red solid lines represent the 3D GL model. The 2D Tinkham model curve slightly better follows the data. However, the difference is too small to conclude which model captures the rotational variation of B_{c2} more accurately. The maximum in $B_{c2}(\theta)$ at T = 0.3 and 0.9 K can not be reached using the magnetic field available in the Heliox.

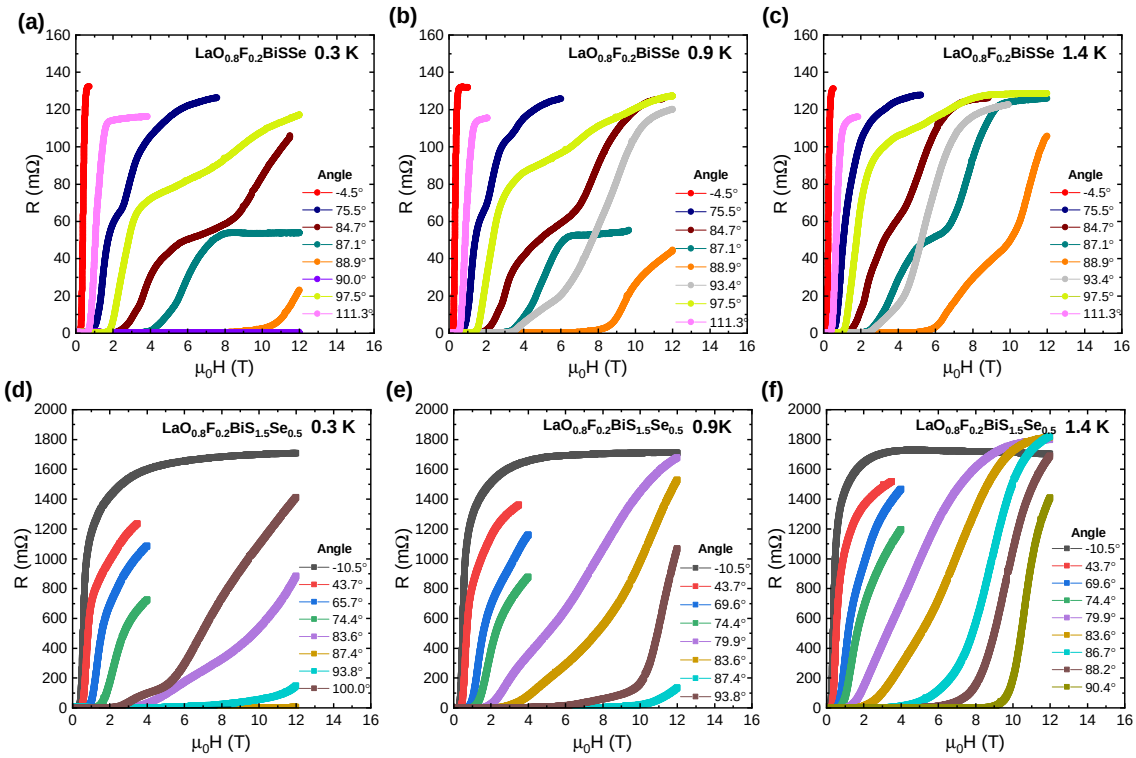

Figure 6.3: In-plane resistance as a function of the magnetic field for angles in between $-10.5°$ and $111.3°$. The angle is defined such that $H \perp ab$ for $0°$ and $H \,||\, ab$ for $90°$ (a),(d): Magnetic field dependence at T = 0.3 K at several angles for $LaO_{0.8}F_{0.2}BiSSe$ (a) and $LaO_{0.8}F_{0.2}BiS_{1.5}Se_{0.5}$ (d). (b),(e): Magnetic field dependence at T = 0.9 K at several angles for $LaO_{0.8}F_{0.2}BiSSe$ (b) and $LaO_{0.8}F_{0.2}BiS_{1.5}Se_{0.5}$ (e). (c),(f) Magnetic field dependence at T = 1.4 K at several angles for $LaO_{0.8}F_{0.2}BiSSe$ (c) and $LaO_{0.8}F_{0.2}BiS_{1.5}Se_{0.5}$ (f).

The $B-T$ phase diagrams are shown in figures 6.5 and 6.6. In figure 6.5 the data attained from measurements in the Heliox system and the PPMS are shown for $LaO_{0.8}F_{0.2}BiS_{1.5}Se_{0.5}$. The PPMS data has been taken by K. Hoshi. While all data shown in this figure are from measurements on the same crystal, the blue squares and black dots representing the $B \,||\, ab$ data are from two different data-sets taken in the PPMS and Heliox system, respectively. The green hexagons are taken from the maxima in B_{c2} determined by the 3D GL and 2D Tinkham model curves. The insets show the $R(B)$ data from which the superconducting transitions up to 12 T (black and red dots) are obtained.

Evidently $B_{c2}^{||}$ greatly exceeds the Pauli limit of $B_c^P = 5.34$ T determined

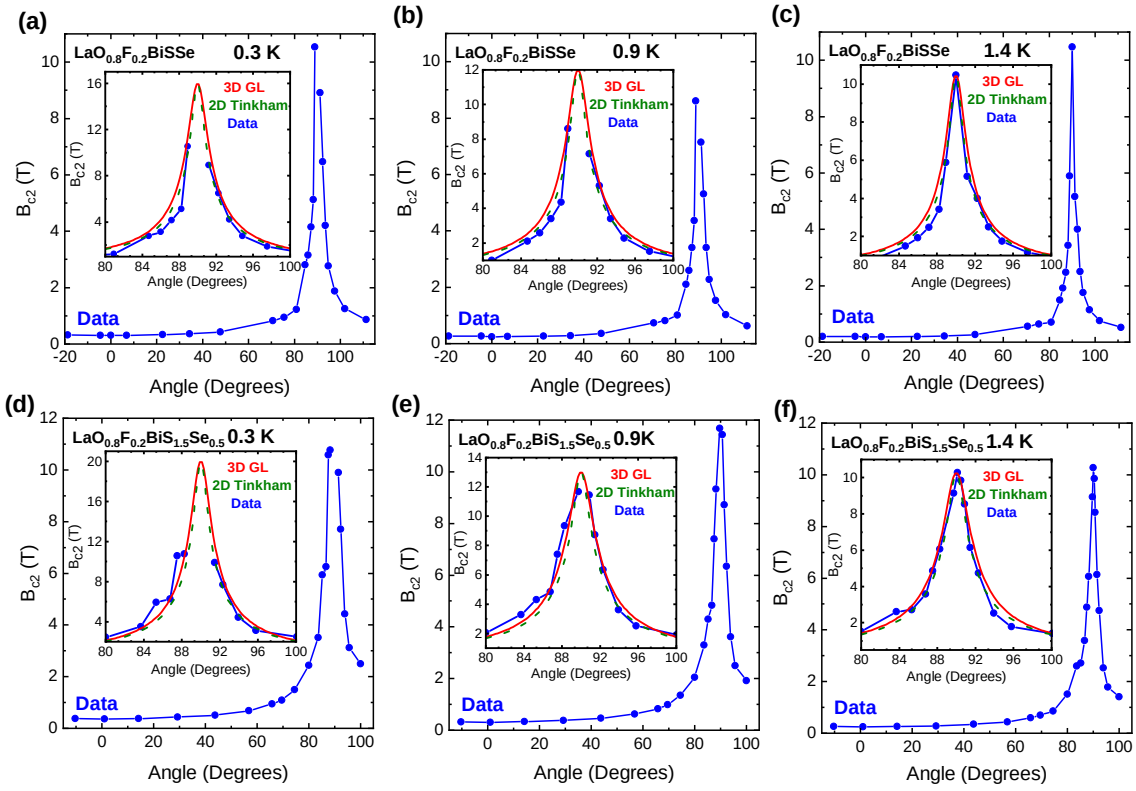

Figure 6.4: Angular variation of B_{c2} ($\theta = 0°$: $B \perp ab$, $\theta = 90°$: $B \parallel ab$). B_{c2} is determined from $R = 0$ points in the data of figure 6.3 and given here in blue. Inset: Data between 80° and 100°. The data is given in blue dots. Fits for the 3D GL mass anisotropy model and 2D Tinkham model are given as a solid red line and a green dashed line, respectively. (a),(b),(c): Data of $LaO_{0.8}F_{0.2}BiSSe$ at 0.3 K, 0.9 K and 1.4 K. (d),(e),(f): data of $LaO_{0.8}F_{0.2}BiS_{1.5}Se_{0.5}$ at 0.3 K, 0.9 K and 1.4 K.

by $B_c^P = 1.86T_c$. To estimate the orbital limit for B_{c2} one may use the relation $B_{c2}^{orb} = 0.69T_c\left(dB_{c2}/dT\right)_{T_c}$ in the WHH formalism [82]. However, using the PPMS dataset for $LaO_{0.8}F_{0.2}BiS_{1.5}Se_{0.5}$ we calculate $B_c^{orb} \sim 3$ T, which is irreconcilable with the data taken in the Heliox at lower temperatures.

In figure 6.6 the $B - T$ phase diagram of $LaO_{0.8}F_{0.2}BiS_{1.5}Se_{0.5}$ is depicted. Similar data-sets are shown as in figure 6.5. The $B \parallel ab$ data is compared to the WHH model. A small discrepancy is found at T = 1.4 K between the measured $B_{c2}^{||}$ and the value attained from the 3D GL and 2D Tinkham model curves. The $B_{c2}^{||}$ points at the lowest temperatures attained from the model curves (green hexagons) are in good agreement with the measured $B_{c2}^{||}$ data at higher temperatures (black dots). Here, the Pauli

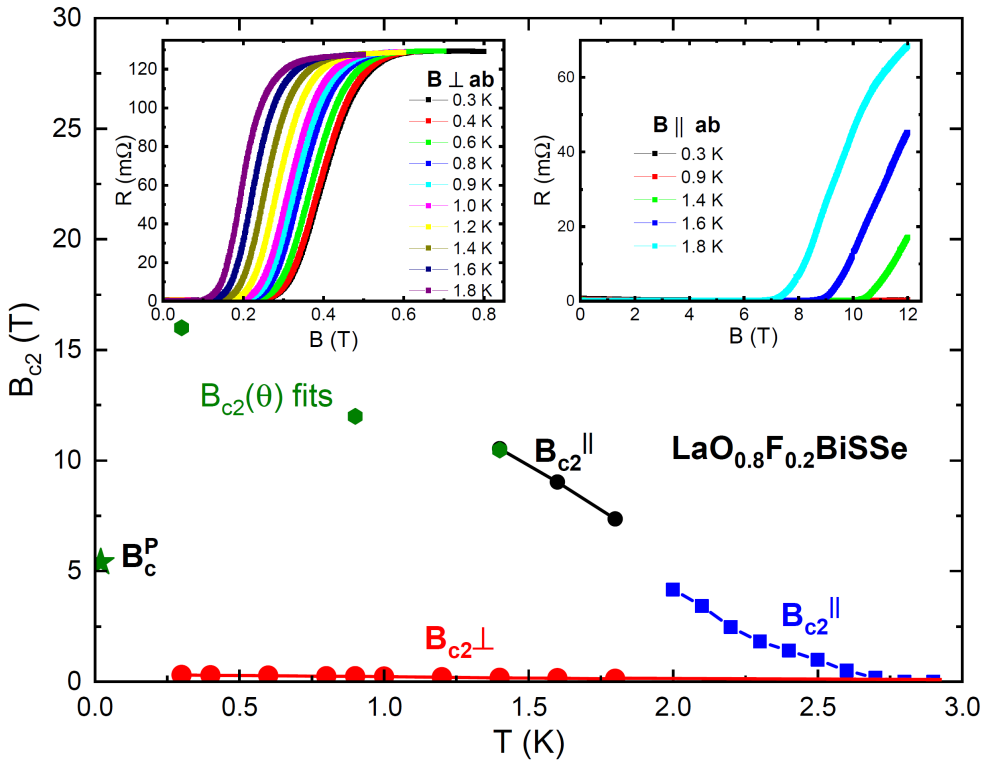

Figure 6.5: B-T phase diagram of $LaO_{0.8}F_{0.2}BiSSe$. Blue squares are B || ab data taken from PPMS measurements (data taken by K. Hoshi). The B || ab data given in black dots and B ⊥ ab data given in red dots are taken from measurements in the Heliox system. The green hexagons represent the field values attained from the 3D GL anisotropic fits and 2D Tinkham fits on the angular variation given in figures 6.4 (a), (b) and (c). The Pauli-limit is given as a green star with $B_c^P = 5.39$ T. Left inset: B ⊥ ab resistance data at temperatures between 0.3 K and 1.8 K. Right inset: B || ab data at temperatures between 0.3 K and 1.8 K

limit is given by $B_c^P = 5.01$ T which is greatly exceeded by the actual $B_{c2}^{||}$. The orbital limit is determined as $B_c^{orb} = 12.7$ T which is also exceeded by $B_{c2}^{||}$.

Linear fits have been applied to the data-sets to give a rough estimate of $B_{c2}^{||}(0)$ and $B_{c2}^{\perp}(0)$ for both compounds. This results in $B_{c2}^{||}(0) = 18.8$ T and 21.4 T, as well as $B_{c2}^{\perp}(0) = 0.36$ T and 0.53 T, for $LaO_{0.8}F_{0.2}BiSSe$ and $LaO_{0.8}F_{0.2}BiS_{1.5}Se_{0.5}$, respectively. Using the relations $B_{c2}^{\perp} = \Phi_0/2\pi\xi_{||}^2$ and $B_{c2}^{||} = \Phi_0/2\pi\xi_{||}\xi_{\perp}$, the in-plane and out of plain coherence lengths are estimated giving $\xi_{||} = 30$ nm and 25 nm as well as $\xi_{\perp} = 0.58$ nm and 0.62 nm for $LaO_{0.8}F_{0.2}BiSSe$ and $LaO_{0.8}F_{0.2}BiS_{1.5}Se_{0.5}$, respectively.

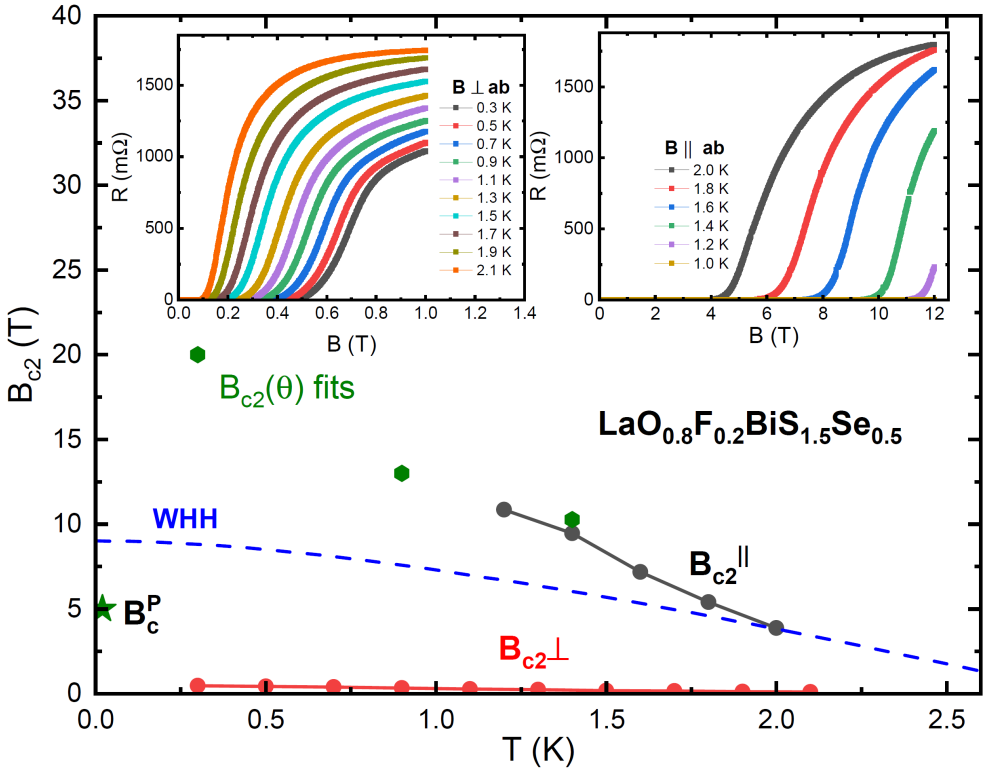

Figure 6.6: B-T phase diagram of $LaO_{0.8}F_{0.2}BiS_{1.5}Se_{0.5}$. The B || ab data given in black dots and B ⊥ ab data given in red dots are taken from measurements in the Heliox system. The green hexagons represent the field values attained from the 3D GL anisotropic fits and 2D Tinkham fits on the angular variation given in figures 6.4 (d), (e) and (f). The Pauli-limit is given as a green star with $B_c^P = 5.0$ T. The WHH-model in the clean limit for the B || ab data is presented as a blue dashed line. Note both the Pauli-limit and the WHH-model fall short in predicting the maximum value of B_{c2}. Left inset: B ⊥ ab resistance data at temperatures between 0.3 K and 2.1 K. Right inset: B || ab resistance data at temperatures between 1.0 K and 2.0 K.

The enhanced superconductivity observed for B || ab greatly exceeds the limits set by the orbital pair breaking effect and the paramagnetic pair breaking effect. In calculating these values the assumption of weak-coupling superconductivity was made. The likelihood of strong-coupling is large in these systems as reported previously [154]. This leads to a larger limit for B_{c2} from the pair breaking effects that are weakened by the strong-coupling [155]. However, even the strong-coupling corrected values are greatly exceeded. The paramagnetic limit could be absent if the superconductivity in

this system is of a triplet nature or at least dominated by triplets in a singlet-triplet mixture. Considering the numerous reports on the $BiCh_2$ systems indicating fully gapped s-wave superconductivity [156, 132, 133, 134, 157, 158], this scenario is unlikely.

The orbital pair breaking effect for B_{c2} can be significantly suppressed by a layered structure with a small out of plane coherence length $\xi_\perp$. If the interlayer distance is significantly larger than $\xi_\perp$, the system should become of a 2D-nature. It follows that the 2D behaviour should be accurately captured by the description of $B_{c2}(\theta)$ in the 2D Tinkham model. The contrast in accuracy of the 2D model and 3D model for $B_{c2}(\theta)$ is too small to conclude a favorable view for either. Noting that $\xi_\perp = 0.58$ and 0.62 nm for $LaO_{0.8}F_{0.2}BiSSe$ and $LaO_{0.8}F_{0.2}BiS_{1.5}Se_{0.5}$, respectively, the blocking layer thickness of 0.26 nm as shown in figure 6.1 is easily overcome by the out of plane coherence length. This suggest the behaviour of the system should be captured by the anisotropic 3D GL model. For $LaO_{0.5}F_{0.5}BiS_{2-x}Se_x$ (x = 0.22 and 0.69) $\xi_\perp = 0.22$ and 0.23 nm for x = 0.22 and 0.69, respectively [145]. There the authors compared the $B_{c2}(\theta)$ data to the 2D Tinkham and 3D GL model and concluded that the 2D Tinkham model was not favorable to describe the $B_{c2}(\theta)$ data, whereas the 3D GL model was not contradictory to the $B_{c2}(\theta)$ data. One would expect a more accurate capture of the data by the 3D GL model for larger $\xi_\perp$ in a similar system. We attribute the lack of greater convergence to the 3D model to the small angle mismatch in the crystals, which significantly influences the expected symmetrical behaviour of B_{c2} for angles close to $B \parallel ab$. It should be noted that in Ref. [145] the midpoint transition has been taken to determine B_{c2}. To elucidate the dimensional nature of superconductivity in this system it is conducive to measure at greater magnetic field strengths to further map out the angular variation of B_{c2} at low temperatures. It is imperative to conduct these experiments with crystals with minimum angle mismatch between layers.

The breaking of the local inversion symmetry in the conduction layers and the consequently manifested Rashba-type spin-orbit coupling that was observed by S-ARPES [151] could be the key to untangle the origin of the anisotropy and enormous value of the $B_{c2}(\theta)$. The interlayer coupling should be diminished by the Rashba-type spin-orbit coupling [150], converting the system closer to 2D superconductivity. In this manner the orbital pair breaking effect is suppressed. The paramagnetic pair breaking effect should be diminished due to the Rashba-spin polarisation locking the spin direction onto the *ab*-plane. Furthermore, local inversion symmetry breaking also allows for a singlet-triplet mixture [159], possibly further circumventing the Pauli-limit, but this possibility is not strongly suggested from experimental results on $BiCh_2$ systems. A lack of clarity on the dimensional nature of the system complicates attributing the anisotropy in $B_{c2}(\theta)$ to Rashba-type

spin-orbit coupling, as a conversion to 2D superconductivity is expected in this case.

6.4 Conclusion

A large anisotropy in the angular variation of B_{c2} in $LaO_{0.8}F_{0.2}BiS_{2-x}Se_x$ ($x = 0.5$ and 1.0) with a high maximum value for $B \parallel ab$ that exceeds the expected limits from orbital pair breaking and paramagnetic pair breaking effects is observed. Results indicate that the anisotropy is continued onto lower temperatures. Neither 2D behaviour or 3D behaviour can be confirmed with the current data, likely due to the anglular mismatch between layers in the crystals. Rashba-type spin-orbit coupling should manifest in the systems due to local inversion symmetry breaking. This possibly leads to a significant suppression of the orbital and paramagnetic limits for B_{c2} and the mediation of the large B_{c2} observed. This study extends the research on the observed anisotropy in $B_{c2}(\theta)$ and the extremely large B_{c2} onto lower temperatures. To elucidate the dimensional nature of these systems, it is conducive to extend this study onto lower temperatures and higher magnetic field strength to further map out $B_{c2}(\theta)$. This contributes further towards understanding the effects of local inversion symmetry breaking on superconductivity.

Chapter 7

Pressure dependence of superconductivity in the Dirac semimetal $PdTe_2$

In this chapter the data collected from the high-pressure study of $PdTe_2$ are presented. It is a continuation of the work of Ref. [101] at higher pressures. The results are incorporated and previously published in Ref. [38]. The main goal of these measurements was to uncover the behaviour of superconductivity at a higher pressure range, specifically in view of the predicted change in electronic properties. Supposedly at 4.7 GPa a pair of Dirac points emerge, and at 6.1 GPa the disappearance of the type-II Dirac cone is predicted to take place [160].

7.1 Introduction

$PdTe_2$ is simultaneously a type-I superconductor and a type-II Dirac semimetal at ambient pressure [44, 39, 41, 42]. The prospect of superconductivity combined with a type-II Dirac cone is especially interesting due to the enhanced possibility of topological states entering the superconducting condensate. Topological transitions are predicted to occur in $PdTe_2$ between 4.7 GPa and 6.1 GPa. At 4.7 GPa a type-I Dirac point is suggested to appear and the type-II Dirac cone is suggested to disappears near 6.1 GPa [160]. Furthermore, it has been shown that type-I superconductivity is feasible for a tilt parameter of $k = 2$ [97]. This prompts the question how the superconducting properties are affected by pressure, especially in view of the topological changes predicted to occur. To this end a pressure study up to 8 GPa has been carried out to investigate the superconducting and structural properties of $PdTe_2$. The results of this study have been published in Ref. [38]. In figure 7.1 the resulting $T - P$ phase diagram is shown. Here T_c^{R1}, T_c^{R2}, and T_c^{R3} denote resistance data taken in a Quantum Design Physical Property Measurement System (PPMS), an Iwatani Industrial Gases ^{3}He-circulation–Joule-Thomson type Gifford-McMahon cryogenic refrigerator and the Heliox system, respectively. T_c^R and T_c^χ denote resistance and ac susceptibility data, respectively, adopted from Ref. [101]. The T_c^{R1} is in stark difference to the other data-sets and therefore assumed not to be intrinsic behaviour of $PdTe_2$ under pressure. Instead it is attributed to pressure-induced superconductivity of Te. A monotonic decrease in T_c is predicted under pressure which is found above 1 GPa [160] for all curves except T_c^{R1}. No indication of changes to the superconductivity stemming from the predicted topological transitions between 4.7 and 6.1 GPa is observed. The remainder of this chapter is a description of the research carried out in the Heliox system.

7.2 Experimental

The resistance as a function of temperature and magnetic field of $PdTe_2$ was investigated under pressure. The resistance measurements were carried out using the four-terminal method. An excitation current of 120 μA was applied using a Linear Research 700 ac resistance bridge. Temperatures down to 0.3 K were reached using the Heliox system. The sample was situated inside the sample space of a Cu-Be modified Bridgman anvil cell described at the end of Chapter 2 of this thesis. The pressure in the cell was generated by use of a hand press (Laboratory Hydraulic Press: LCP20 Unipress).

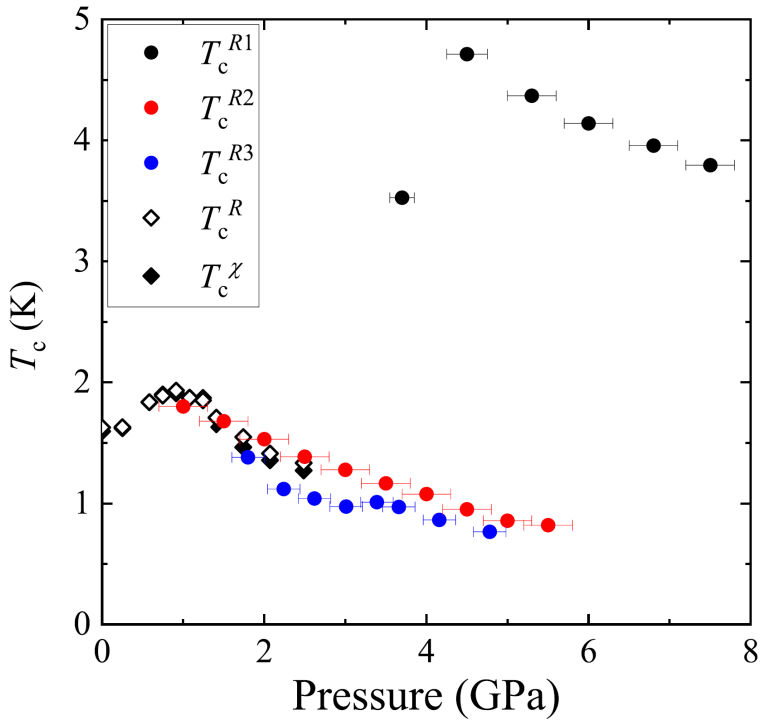

Figure 7.1: $T - P$ phase diagram of $PdTe_2$. T_c is taken as the onset of superconductivity. The black (T_c^{R1}), red (T_c^{R2}), and blue (T_c^{R3}) dots denote data taken in a Quantum Design PPMS, an Iwatani Industrial Gases ^{3}He-circulation–Joule-Thomson type Gifford-McMahon cryogenic refrigerator and the Heliox system, respectively. Open (T_c^{R}) and closed (T_c^{χ}) black diamonds indicate previous results of resistivity and ac susceptibility measurements [101]. Figure adopted from Ref. [38].

7.3 Results and discussion

In figure 7.2 the resistance as a function of temperature is depicted at pressures between 2.24 and 6.82 GPa from room temperature (RT) down to 2 K. The expected metallic behaviour is seen at lower temperatures. The nearly linear temperature dependence above 50 K as previously reported on samples from the same batch [38, 44] is not reproduced. The temperature data of the ^{3}He pot thermometer was chosen here since the sample thermometer is not calibrated at high temperatures. The temperature curves having some curvature as opposed to a nearly linear temperature dependence is probably due to a temperature gradient between the ^{3}He pot and the sample during cooldown. The resistance curves that are normalised to their respective RT values (R(T)/R(RT)) for comparison are presented in figure 7.3. Here a definitive trend is not observed between the resistance curves of the different pressures. The decrease in RT resistance with respect to pressure observed

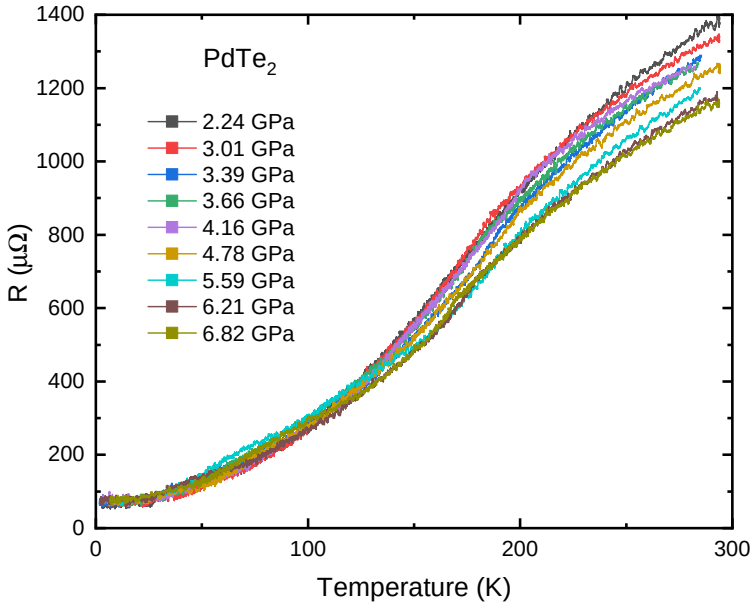

Figure 7.2: Temperature dependence of the resistance of $PdTe_2$ at 0 mT between 0.3 and 300 K at pressures between 2.24 and 6.82 GPa.

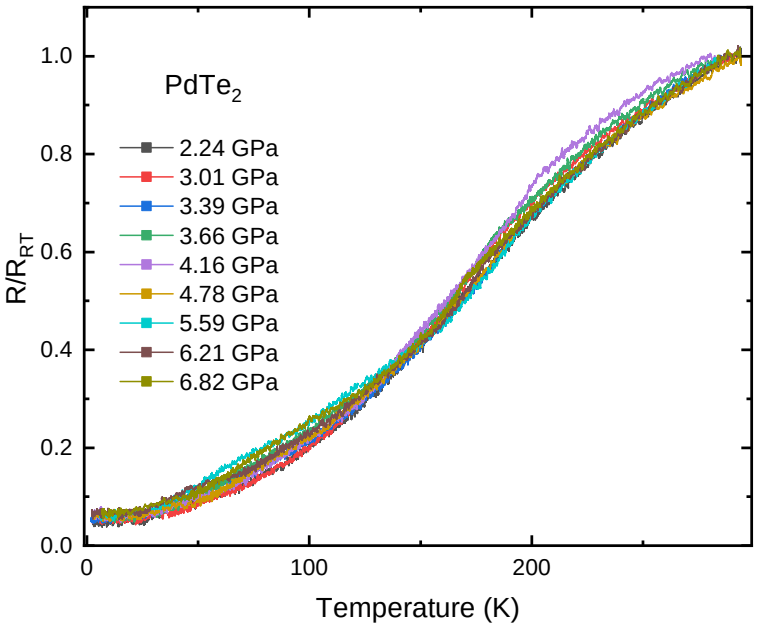

Figure 7.3: Temperature dependence of the resistance of $PdTe_2$ at 0 mT between 0.3 and 300 K at pressures between 2.24 and 6.82 GPa. The resistance is normalised to the room temperature value for each curve.

in figure 7.2 is not reflected at lower temperatures in figure 7.3, likely due to the large noise present in the data.

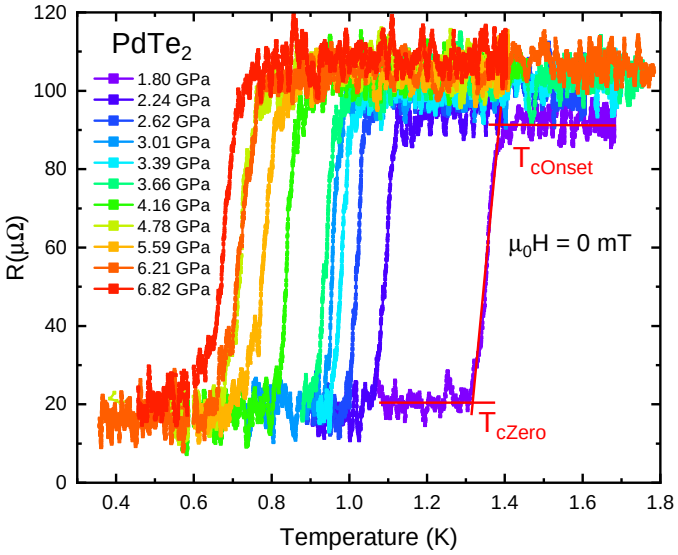

Figure 7.4: Resistance against temperature curves of the superconducting transition of $PdTe_2$ at $\mu_0 H = 0$ mT for pressures between 1.80 and 6.82 GPa. Red lines indicate the determination of the transition temperature as the onset (T_{cOnset}) and $R = 0$ (T_{cZero}).

The zero-field superconducting transition data at pressures between 1.80 and 6.82 GPa are depicted in figure 7.4. The manner of determination for the onset temperature (T_{cOnset}) and $R = 0$ temperature (T_{cZero}) is depicted with red lines. The intersection of the slopes of the normal state resistance and the resistance in the superconducting transition is taken as the onset temperature. Similarly, extrapolating $R(T)$ in the superconducting transition linearly to the $R = 0$ value on the x axis is taken as the T_{cZero} temperature. The small nonzero resistance is likely due to the added resistance of the contacts on the sample. The decrease in T_c with respect to pressure is observed as expected and is depicted in figure 7.9, and also reported in figure 7.1.

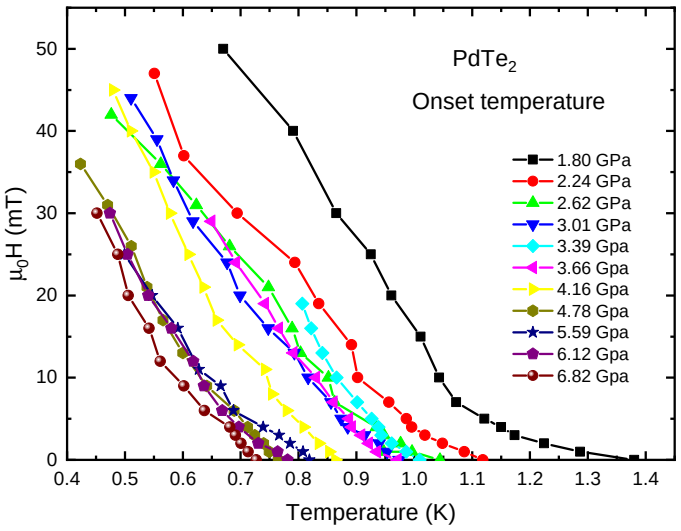

Figure 7.5: Phase diagram of magnetic field strength against temperature of the T_{cOnset} of $PdTe_2$ at pressures between 1.80 and 6.82 GPa.

The $B - T$ phase diagrams of $PdTe_2$ determined by the T_{cOnset} and the T_{cZero} are presented in figures 7.5 and 7.6, respectively. Data were taken for each pressure up to fields where T_{cOnset} could no longer be determined. The decrease in T_c with respect to pressure is visible in both phase diagrams. An upturn near 5 mT is present for the T_{cOnset} phase diagram at lower pressures, whereas it is absent for the T_{cZero} phase diagram. This is expected if one takes superconductivity of the surface sheath into account. In this manner the phase diagram given in figure 4 of Ref. [44] is reproduced with the upturn at 5 mT indicating the higher T_c of the superconductivity of the surface sheath from 5 mT onwards. The overall trend of a decreasing T_c with respect to pressure is the same for both methods. No particular observation in the superconducting transition by either determination of the transition is present indicative of the topological changes in the 4.7 - 6.1 GPa range

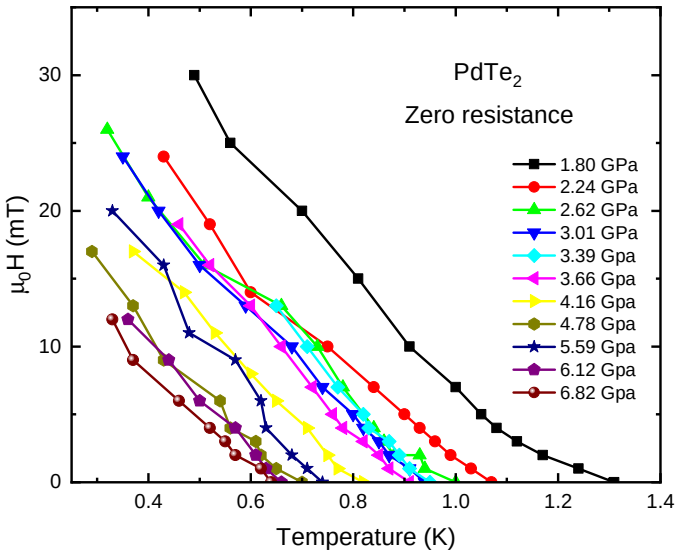

Figure 7.6: Phase diagram of magnetic field strength against temperature of the T_{cZero} of $PdTe_2$ at pressures between 1.80 and 6.82 GPa.

[160].

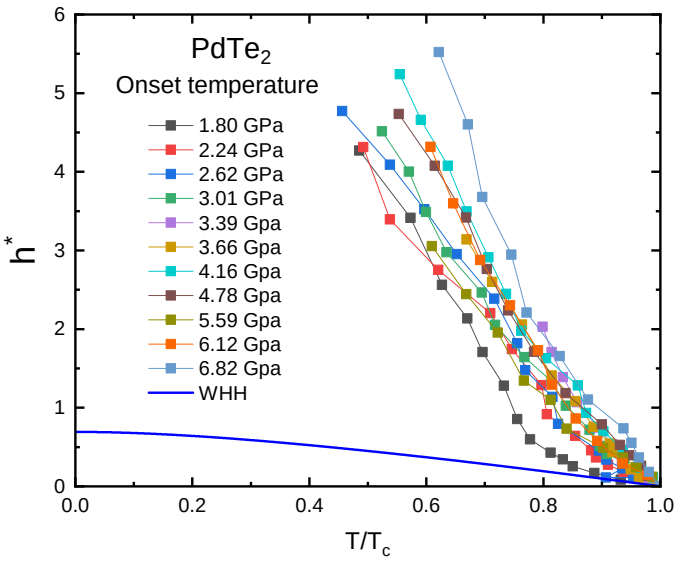

Figure 7.7: Reduced field $h^* = (B_{c2}(T)/T_c)/|dB_{c2}/dT|_{T_c}$ as a function of reduced temperature T/T_c for pressures between 1.80 and 6.82 GPa. The blue solid line depicts the WHH-curve. Data is taken from the T_{cOnset} curves.

To further analyse the pressure dependence of the superconducting state

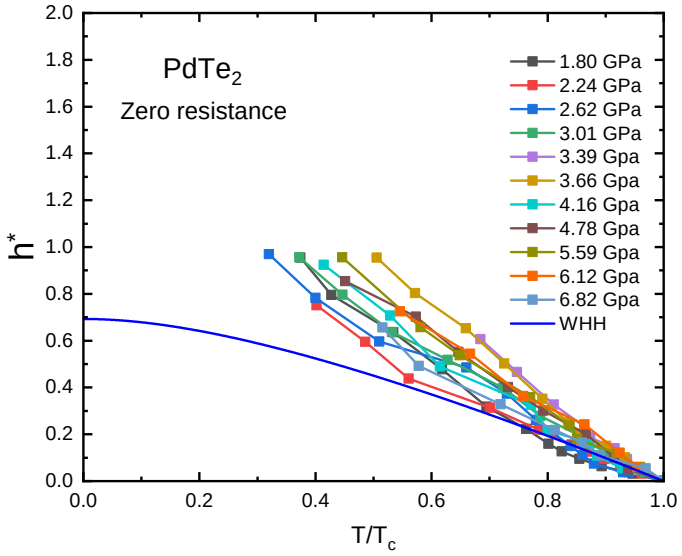

Figure 7.8: Reduced field $h^* = (B_{c2}(T)/T_c)/|dB_{c2}/dT|_{T_c}$ as a function of reduced temperature T/T_c for pressures between 1.80 and 6.82 GPa. The blue solid line depicts the WHH-curve. Data is taken from the T_{cZero} curves.

of $PdTe_2$ we have opted to compare it to the Werthamer-Helfland-Hohenberg (WHH) model for weakly coupled type-II superconductivity in the dirty limit. In figures 7.7 and 7.8 WHH plots are given for T_{cOnset} and T_{cZero}, respectively. Here $h^* = (B_{c2}(T)/T_c)/|dB_{c2}/dT|_{T_c}$. Evidently the behaviour of the T_{cOnset} curves is not accurately captured by the WHH model. The slope of the 1.80 GPa curve changes significantly around 0.8 T/T_c. We attribute this change to the T_c of the bulk superconductivity being overtaken by that of the superconductivity of the surface sheath at this temperature for 1.80 GPa. The T_{cZero} curves compare better but the incongruency with the WHH model remains large. Comparing the T_{cZero} curves to figure S4 of Ref. [101], where the same WHH plot was made for superconductivity of the surface sheath of $PdTe_2$ between 0 and 2.5 GPa, similar behaviour is observed. This is likely due to the T_c of the surface superconductivity overtaking the T_c of the bulk superconductivity near 1.5 GPa [101]. From the data presented in figure 7.8, the T_c of the surface superconductivity remains higher than that of the bulk superconductivity up to 6.82 GPa.

In figure 7.9 the $T - P$ phase diagram is presented. The T_c values extracted from figure 7.4 are given in cyan and purple dots for T_{cZero} and T_{cOnset}, respectively. The theoretical prediction of Ref. [160] is traced in orange and green dots. The orange data are directly taken from Ref. [160], whereas the light green data are normalised to the ambient pressure T_c reported in [44]. The general trend of decreasing T_c with respect to pressure

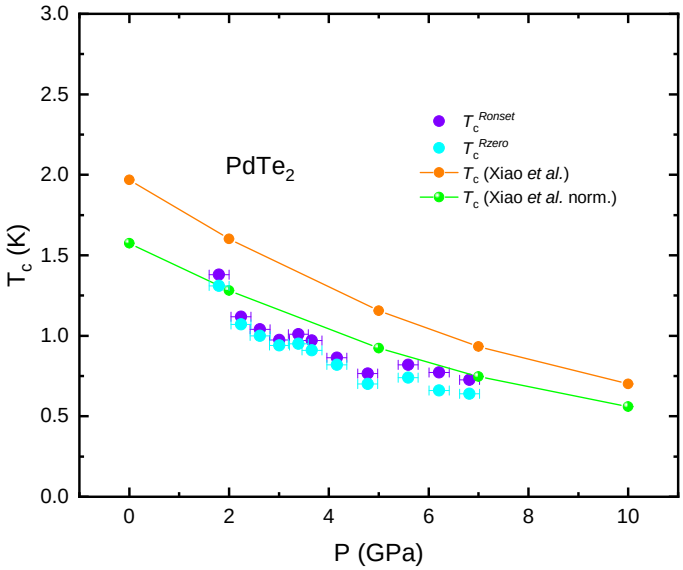

Figure 7.9: Phase diagram of temperature as a function of pressure. Purple and cyan dots depict T_{cOnset} and T_{cZero}, respectively. Calculated values of T_c adopted from Ref. [160] are presented in orange and green values for regular and normalised (see text), respectively.

of the measured data follows that of the prediction. Around 2 GPa a sharp decrease is found for the measured data that initiates the difference between the normalised prediction and the measured data. In other data-sets of measurements that have mapped out this pressure range in $PdTe_2$ using different equipment and samples, the decrease in T_c around 2 GPa is absent [38] (see figure 7.1). We therefore conclude this phenomenon to be sample-related or an artifact of the measurement.

7.4 Conclusion

We have carried out a high pressure transport study of superconductivity in $PdTe_2$ at temperatures down to 0.3 K. The results presented here are incorporated as T_c^{R3} in Ref. [38]. The effect of pressures higher than reported in Ref. [101] on superconductivity are shown to have a monotonic decrease with the exception of a sharp decrease around 2 GPa. This decrease was not reproduced in other high-pressure measurements on $PdTe_2$ [38] indicating it is not intrinsic behaviour of $PdTe_2$. The superconductivity of the surface sheath persisting up to 6.18 GPa is observed by the upturn around 5 mT as well as the discrepancy in the WHH plots for the T_{cOnset} curves and the T_{cZero} curves. No observable changes to the superconducting transition in

the 4.6-6.1 GPa range was observed, indicating no direct change from the predicted topological transitions of the Dirac cones.

Summary

Superconductivity has remained an active area of research for over 100 years. The interplay between superconductivity and other phases of matter continues to be an excellent avenue to explore novel physical phenomena. This thesis is a report on materials in which electrons form Cooper pairs and have symmetry properties that allow for the exhibition of novel phenomena in the superconducting state. The type-II Dirac semimetal $PdTe_2$ is a type-I superconductor with unusual superconductivity in the surface sheath. The results of relaxation calorimetry to investigate the intermediate state, and a pressure study as well as a doping study to tune the superconductivity, are presented here. The angle-dependent magnetotransport study on the layered superconductor $LaO_{0.8}F_{0.2}BiS_{2-x}Se_x$ ($x = 0.5$ and 1.0), with breaking of the local inversion symmetry possibly leading to the large anisotropy in the upper critical field is presented. The content of the chapters is as follows:

The first chapter served as a short introductory treatment on topological materials and superconductivity. The main purpose was to peak the interest of the reader by explaining why these phases of matter have garnered widespread interest. $PdTe_2$, the material which is the focus of this thesis, was introduced. The second chapter dealt with the experimental aspects used in the research that culminated in this thesis. The setups used to investigate material behaviour at low temperatures were given and described in detail. The third chapter introduces the relevant theoretical aspects to the later chapters.

In Chapter 4 the results of the heat capacity study on $PdTe_2$ using relaxation calorimetry were presented. The type-I nature of superconductivity was successfully probed by the observation of latent heat of the intermediate phase in fields, giving the first thermodynamic evidence for type-I superconductivity in $PdTe_2$. Weak-coupling was inferred from the zero-field jump size $\Delta C/\gamma T_c = 1.42$, exponential scaling in the low temperature range and the full superconducting temperature range being accurately captured by Mühlschlegel's tabulated values.

In Chapter 5 the study on the disorder-induced transition from type-I

to type-II superconductivity in $PdTe_2$ was presented. The goal was to intentionally induce disorder in $PdTe_2$ by the isoelectronic substitution of Pt to force the transition. Two single-crystalline batches $Pd_{1-x}Pt_xTe_2$ were prepared with nominal values $x = 0.05$ and $x = 0.10$. Sample characterization by EDX spectroscopy revealed Pt did not dissolve homogeneously in the crystals. The prepared samples could nonetheless sufficiently be characterised to attribute the transition to increasing disorder. By demonstrating the absence of the differential paramagnetic effect in ac susceptiblity measurements and the latent heat in heat capacity measurements for the $x = 0.10$ batch we have unambiguously presented evidence for the transition from type-I to type-II superconducting behaviour upon increasing disorder. In terms of the residual resistivity a minimum value of $\rho_0 = 1.4$ $\mu\Omega$cm suffices to turn $PdTe_2$ into a superconductor of the second kind.

In Chapter 6 the angle-dependent magnetotransport measurements on $LaO_{0.8}F_{0.2}BiS_{2-x}Se_x$ ($x = 0.5$ and 1.0) were shown. A large anisotropy in the angular variation of B_{c2} was observed with a large maximum value for $B \parallel ab$. The value of B_{c2} for $B \parallel ab$ exceeds the limits set by the orbital pair breaking and paramagnetic pair breaking effects. From measurements carried out at low temperatures it is inferred that the anisotropy in the superconducting state persists monotonously down to 0.3 K. Whether the anisotropy is of a 2D or a 3D nature can not be concluded from the current data-set. Local inversion symmetry breaking should manifest in these systems through Rashba-type spin-orbit coupling. This possibly leads to a significant suppression of the orbital and paramagnetic effects for B_{c2} allowing for the mediation of the large B_{c2} observed.

In Chapter 7 the details of a high pressure transport study of superconductivity in $PdTe_2$ were presented. The effect of pressures higher than reported previously on superconductivity are shown to have a monotonic decrease except for the observation of a sharp decrease around 2 GPa. Other measurements showed this decrease to be sample or run-specific as it was not reproducible, indicating a smooth monotonic decrease to be intrinsic behaviour of $PdTe_2$ under pressure. The superconductivity of the surface sheath was shown to persist at higher pressures as evidenced by the upturn around 5 mT and the differences in WHH plots between the $R = 0$ and onset temperature plots. No changes originating from the topological transitions of the Dirac cones predicted to occur around 4.6-6.1 GPa were observed.

Samenvatting

Supergeleiding is al meer dan 100 jaar een actief onderzoeksgebied. Het samenspel tussen supergeleiding en andere fasen van materie blijft een uitstekende manier om nieuwe fysische fenomenen te verkennen. Dit proefschrift is een rapport over materialen waarin elektronen Cooperparen vormen en symmetrie eigenschappen hebben die het mogelijk maken nieuwe fenomenen in de supergeleidende toestand te vertonen. Het type-II Dirac-semimetaal $PdTe_2$ is een type-I supergeleider met ongebruikelijke supergeleiding aan het oppervlak. De resultaten van relaxatiecalorimetrie om de intermediaire toestand te onderzoeken, en een hogedrukstudie evenals een dopingstudie om de supergeleiding af te stemmen, zijn hier gepresenteerd. Tevens werd een hoekafhankelijke magnetotransportstudie van de gelaagde supergeleider $LaO_{0.8}F_{0.2}BiS_{2-x}Se_x$ ($x = 0.5$ en 1.0), waarbij de lokale inversiesymmetrie gebroken is, hetgeen mogelijk leidt tot een grote anisotropie in het bovenste kritische veld, gepresenteerd. De inhoud van de hoofdstukken is als volgt:

Het eerste hoofdstuk diende als een korte inleidende behandeling over topologische materialen en supergeleiding. Het belangrijkste doel was om de interesse van de lezer te wekken door uit te leggen waarom deze fasen van materie wijdverbreide belangstelling hebben vergaard. $PdTe_2$, het materiaal waarop dit proefschrift zich richt, werd geïntroduceerd. Het tweede hoofdstuk behandelde de experimentele aspecten die werden gebruikt in het onderzoek dat resulteerde in dit proefschrift. De experimentele opstellingen die werden gebruikt om materiaalgedrag bij lage temperaturen te onderzoeken, werden in detail beschreven. Het derde hoofdstuk introduceerde de relevante theoretische aspecten voor de latere hoofdstukken.

In Hoofdstuk 4 werden de resultaten gepresenteerd van de warmtecapaciteitsstudie van $PdTe_2$ met behulp van relaxatiecalorimetrie. De type-I aard van de supergeleiding werd met succes onderzocht door de waarneming van de latente warmte van de intermediaire toestand in een magneetveld, wat het eerste thermodynamische bewijs opleverde voor type-I supergeleiding in $PdTe_2$. Supergeleiding van het zwakke-koppeling type werd afgeleid uit de spronggrootte $\Delta C/\gamma T_c = 1.42$ in nulveld bij T_c, de exponentiële afhanke-

lijkheid in het lage temperatuurgebied can de soortelijke warmte $C(T)$ en het nauwkeurig volgen van $C(T)$ in het volledige supergeleidende temperatuurgebied van de door Mühlschlegel's getabelleerde waarden.

In Hoofdstuk 5 werd het onderzoek naar een door verstoring van het kristalrooster geinduceerde overgang van type-I naar type-II supergeleiding in $PdTe_2$ gepresenteerd. Het doel was om opzettelijk wanorde in $PdTe_2$ te introduceren door de iso-elektronische substitutie van Pt. Twee eenkristallijne preparaten $Pd_{1-x}Pt_xTe_2$ werden gesynthetiseerd, met nominale waarden $x = 0.05$ en $x = 0.10$. Monsterkarakterisering door EDX-spectroscopie onthulde dat Pt niet homogeen oploste in de kristallen. De voorbereide monsters konden desalniettemin voldoende worden gekarakteriseerd om de overgang toe te schrijven aan de toegenomen wanorde. Door de afwezigheid aan te tonen van het differentiële paramagnetische effect in ac-susceptibilitietsmetingen en de latente warmte in warmtecapaciteitsmetingen voor het $x = 0.10$ preparaat, hebben we ondubbelzinnig bewijs gepresenteerd voor de overgang van type-I naar type-II supergeleidend gedrag bij toenemende wanorde. In termen van de restweerstand is een minimale waarde van $\rho_0 = 1.4$ $\mu\Omega$cm voldoende om van $PdTe_2$ een supergeleider van de tweede soort te maken.

In Hoofdstuk 6 werden de hoekafhankelijke magnetotransportmetingen aan $LaO_{0.8}F_{0.2}BiS_{2-x}Se_x$ ($x = 0.5$ en 1.0) gepresenteerd. Een grote anisotropie in de hoekafhankelijkheid van B_{c2} werd waargenomen met een grote maximale waarde voor $B \parallel ab$. De waarde van B_{c2} voor $B \parallel ab$ overschrijdt de limieten die zijn vastgesteld voor het orbitale paar-brekingseffect en het paramagnetische paar-brekingseffect. Uit metingen uitgevoerd bij lage temperaturen werd afgeleid dat de anisotropie van B_{c2} in de supergeleidende toestand monotoon blijft bestaan tot 0.3 K. Of de anisotropie van 2D of 3D aard is kan niet worden afgeleid uit de huidige dataset. Lokale inversiesymmetriebreking zou zich in deze systemen moeten manifesteren door middel van Rashba-type spin-orbit-koppeling. Dit leidt mogelijk tot een significante onderdrukking van het orbitale paar-brekingseffect en het paramagnetische paar-brekingseffect voor B_{c2}, waardoor de grote waargenomen B_{c2} kan worden verklaard.

In Hoofdstuk 7 werden de details gepresenteerd van een transportstudie van supergeleiding in $PdTe_2$ onder hoge druk. Het effect van drukken hoger dan eerder gerapporteerd op supergeleiding blijkt een monotone afname van T_c te zijn, behalve de waarneming van een scherpe afname rond 2 GPa. Andere metingen toonden aan dat deze afname monster- of run-specifiek was, omdat deze niet reproduceerbaar bleek, wat erop wijst dat een gelijkmatige monotone afname het intrinsieke gedrag van $PdTe_2$ is onder druk. De supergeleiding op het oppervlak bleek aan te houden bij hogere drukken, zoals bleek uit de stijging rond 5 mT en de verschillen in WHH-grafieken tussen

de $R = 0$ en de aanvangtemperatuurgrafieken. Er werden geen veranderingen waargenomen die voortkwamen uit de topologische overgangen van de Dirac-kegels die voorspeld waren rond een druk van 4.6-6.1 GPa.

Acknowledgements

First of all I would like to give thanks to my promotor and supervisor Dr. Anne de Visser. Having spent over 5 years under your supervision from the start of my bachelor project, throughout my master project and the duration of my PhD, I can wholeheartedly state that I have thoroughly enjoyed my time working with you. Your guidance in experimental know-how down to minute details and critical assessment of my writing and presentations is deeply appreciated. I am also grateful for the social events you organised for the betterment of social cohesion. My thanks goes out to my co-promotor Prof. Dr. Mark Golden. Throughout my years at the lab it has always been a pleasure to listen to your talks and your advice has been greatly appreciated. No experiment can be carried out without the samples to study, so for this I thank Dr. Yingkai Huang for his invaluable work on the synthesis of materials. I would like to express my gratitude to the members of the doctorate committee for their participation in the defence. A big thanks to the people of the technology centre for the assistance in the creation and maintenance/fixes of our setups. I am grateful to the IOP secretary for all the administrative work that has been carried out. Huaqian, I greatly enjoyed having worked with you in the lab. Discussing scientific work and other things, it was a pleasure to have your zestfulness around. Jelle, I hope you can your hands on some $IrTe_2$ during the remainder of your PhD. It was great fun working with you in the lab and outside. Kazu, I enjoyed working with you and conversing about various topics. I am happy the collaboration still went through despite the pandemic. Stephan, thank you for the small talks every so often. I greatly appreciate your presence in the lab and outside. A fresh pair of eyes is always conducive to productive contributions. Ayako and Fumi, your stay in the lab was quite succeful and I am happy to have collaborated with you. George, Lewis, Steef, Roel, Maarten and Xuanbo, thank you for having made the duration of my PhD enjoyable as colleagues and friends. Last but not least, I give thanks to my family and friends who have always been curious, supportive and energetic about my research.

List of publications

[**1**] A. M. Nikitin, V. Grinenko, R. Sarkar, J. -C. Orain, **M. V. Salis**, J. Henke, Y. K. Huang, H. -H. Klauss, A. Amato, A. de Visser, "Macroscopic phase separation of superconductivity and ferromagnetism in $Sr_{0.5}Ce_{0.5}FBiS_{2-x}Se_x$ revealed by μSR,"*Scientific Reports,* vol. 7, p. 17370, 2017.

[**2**] **M. V. Salis**, P. Rodière, H. Leng, Y. K. Huang, and A. de Visser, "Penetration depth study of the type-I superconductor PdTe2," *Journal of Physics: Condensed Matter,* vol. 30, no. 50, p. 505602, 2018.

[**3**] **M. V. Salis**, Y. K. Huang, and A. de Visser, "Heat capacity of type- I superconductivity in the Dirac semimetal $PdTe_2$," *Phys. Rev. B,* vol. 103, p. 104502, 2021.

[**4**] Y. Furue, T. Fujino, **M. V. Salis**, H. Leng, F. Ishikawa, T. Naka, S. Nakano, Y. Huang, A. de Visser, and A. Ohmura, "Superconducting and structural properties of the type-I superconductor $PdTe_2$ under high pressure," *Phys. Rev. B*, vol. 104, p. 144510, 2021.

[**5**] **M. V. Salis**, J. P. Lorenz, Y. K. Huang, and A. de Visser, Disorder-induced transition from type-I to type-II superconductivity in the Dirac semimetal $PdTe_2$, " *Phys. Rev. B*, vol 105, p. 054508, 2022.

Chapter 4 is based on [**3**].
Chapter 7 is partially based on [**4**].
Chapter 5 is based on [**5**].

Bibliography

[1] J. Bardeen, L. N. Cooper, and J. R. Schrieffer, "Microscopic theory of superconductivity," *Phys. Rev.*, vol. 106, pp. 162–164, 1957.

[2] J. G. Bednorz and K. A. Müller, "Possible high T_c superconductivity in the Ba-La-Cu-O system," *Zeitschrift für Physik B Condensed Matter*, vol. 64, no. 2, pp. 189–193, 1986.

[3] A. D. Huxley, "Ferromagnetic superconductors," *Physica C: Superconductivity and its Applications*, vol. 514, pp. 368–377, 2015.

[4] K. v. Klitzing, G. Dorda, and M. Pepper, "New method for high-accuracy determination of the fine-structure constant based on quantized hall resistance," *Phys. Rev. Lett.*, vol. 45, pp. 494–497, 1980.

[5] D. J. Thouless, M. Kohmoto, M. P. Nightingale, and M. den Nijs, "Quantized hall conductance in a two-dimensional periodic potential," *Phys. Rev. Lett.*, vol. 49, pp. 405–408, 1982.

[6] Y. K. Kato, R. C. Myers, A. C. Gossard, and D. D. Awschalom, "Observation of the spin hall effect in semiconductors," *Science*, vol. 306, no. 5703, pp. 1910–1913, 2004.

[7] C. L. Kane and E. J. Mele, "Z_2 topological order and the quantum spin hall effect," *Phys. Rev. Lett.*, vol. 95, p. 146802, 2005.

[8] C. L. Kane and E. J. Mele, "Quantum spin hall effect in graphene," *Phys. Rev. Lett.*, vol. 95, p. 226801, 2005.

[9] J. E. Moore and L. Balents, "Topological invariants of time-reversal-invariant band structures," *Phys. Rev. B*, vol. 75, p. 121306, 2007.

[10] Y. L. Chen, J. G. Analytis, J.-H. Chu, Z. K. Liu, S.-K. Mo, X. L. Qi, H. J. Zhang, D. H. Lu, X. Dai, Z. Fang, S. C. Zhang, I. R. Fisher, Z. Hussain, and Z.-X. Shen, "Experimental realization of a three-dimensional topological insulator, Bi_2Te_3," *Science*, vol. 325, no. 5937, pp. 178–181, 2009.

[11] Y. Ando, "Topological insulator materials," *Journal of the Physical Society of Japan*, vol. 82, no. 10, p. 102001, 2013.

[12] A. Hirohata, K. Yamada, Y. Nakatani, I.-L. Prejbeanu, B. Diény, P. Pirro, and B. Hillebrands, "Review on spintronics: Principles and device applications," *Journal of Magnetism and Magnetic Materials*, vol. 509, p. 166711, 2020.

[13] M. He, H. Sun, and Q. L. He, "Topological insulator: Spintronics and quantum computations," *Frontiers of Physics*, vol. 14, no. 4, p. 43401, 2019.

[14] Y. Xia, D. Qian, D. Hsieh, L. Wray, A. Pal, H. Lin, A. Bansil, D. Grauer, Y. S. Hor, R. J. Cava, and M. Z. Hasan, "Observation of a large-gap topological-insulator class with a single Dirac cone on the surface," *Nature Physics*, vol. 5, no. 6, pp. 398–402, 2009.

[15] A. A. Burkov, M. D. Hook, and L. Balents, "Topological nodal semimetals," *Phys. Rev. B*, vol. 84, p. 235126, 2011.

[16] B. Yan and C. Felser, "Topological materials: Weyl semimetals," *Annual Review of Condensed Matter Physics*, vol. 8, no. 1, pp. 337–354, 2017.

[17] Z. Wang, Y. Sun, X.-Q. Chen, C. Franchini, G. Xu, H. Weng, X. Dai, and Z. Fang, "Dirac semimetal and topological phase transitions in A_3Bi (A = Na, K, Rb)," *Phys. Rev. B*, vol. 85, p. 195320, 2012.

[18] H. Zheng and M. Z. Hasan, "Quasiparticle interference on type-I and type-II Weyl semimetal surfaces: a review," *Advances in Physics: X*, vol. 3, no. 1, p. 1466661, 2018.

[19] S. M. Young, S. Zaheer, J. C. Y. Teo, C. L. Kane, E. J. Mele, and A. M. Rappe, "Dirac semimetal in three dimensions," *Phys. Rev. Lett.*, vol. 108, p. 140405, 2012.

[20] S. M. Young and C. L. Kane, "Dirac semimetals in two dimensions," *Phys. Rev. Lett.*, vol. 115, p. 126803, 2015.

[21] A. A. Soluyanov, D. Gresch, Z. Wang, Q. Wu, M. Troyer, X. Dai, and B. Bernevig, "Type-II weyl semimetals," *Nature*, vol. 257, p. 495, 2015.

[22] L. Fu and C. L. Kane, "Superconducting proximity effect and Majorana Fermions at the surface of a topological insulator," *Phys. Rev. Lett.*, vol. 100, p. 096407, 2008.

[23] G. Moore and N. Read, "Nonabelions in the fractional quantum hall effect," *Nuclear Physics B*, vol. 360, no. 2, pp. 362–396, 1991.

[24] A. Kitaev, "Fault-tolerant quantum computation by anyons," *Annals of Physics*, vol. 303, no. 1, pp. 2–30, 2003.

[25] M. Z. Hasan and C. L. Kane, "Colloquium: Topological insulators," *Rev. Mod. Phys.*, vol. 82, pp. 3045–3067, 2010.

[26] M. Sato and Y. Ando, "Topological superconductors: a review," *Reports on Progress in Physics*, vol. 80, no. 7, p. 076501, 2017.

[27] M. Leijnse and K. Flensberg, "Introduction to topological superconductivity and Majorana fermions," *Semiconductor Science and Technology*, vol. 27, no. 12, p. 124003, 2012.

[28] L. Fu, "Odd-parity topological superconductor with nematic order: Application to $Cu_xBi_2Se_3$," *Phys. Rev. B*, vol. 90, p. 100509, 2014.

[29] Y. S. Hor, A. J. Williams, J. G. Checkelsky, P. Roushan, J. Seo, Q. Xu, H. W. Zandbergen, A. Yazdani, N. P. Ong, and R. J. Cava, "Superconductivity in $Cu_xBi_2Se_3$ and its implications for pairing in the undoped topological insulator," *Phys. Rev. Lett.*, vol. 104, p. 057001, 2010.

[30] S. Sasaki, M. Kriener, K. Segawa, K. Yada, Y. Tanaka, M. Sato, and Y. Ando, "Topological Superconductivity in $Cu_xBi_2Se_3$," *Phys. Rev. Lett.*, vol. 107, p. 217001, 2011.

[31] Shruti, V. Maurya, P. Neha, P. Srivastava, and S. Patnaik, "Superconductivity by Sr intercalation in the layered topological insulator Bi_2Se_3," *Phys. Rev. B*, vol. 92, p. 020506, 2015.

[32] J. L. Zhang, S. J. Zhang, H. M. Weng, W. Zhang, L. X. Yang, Q. Q. Liu, S. M. Feng, X. C. Wang, R. C. Yu, L. Z. Cao, L. Wang, W. G. Yang, H. Z. Liu, W. Y. Zhao, S. C. Zhang, X. Dai, Z. Fang, and C. Q. Jin, "Pressure-induced superconductivity in topological parent compound Bi_2Te_3," *Proceedings of the National Academy of Sciences*, vol. 108, no. 1, pp. 24–28, 2011.

[33] J. Zhu, J. L. Zhang, P. P. Kong, S. J. Zhang, X. H. Yu, J. L. Zhu, Q. Q. Liu, X. Li, R. C. Yu, R. Ahuja, W. G. Yang, G. Y. Shen, H. K. Mao, H. M. Weng, X. Dai, Z. Fang, Y. S. Zhao, and C. Q. Jin, "Superconductivity in topological insulator Sb_2Te_3 induced by pressure," *Scientific Reports*, vol. 3, no. 1, p. 2016, 2013.

[34] K. Kirshenbaum, P. S. Syers, A. P. Hope, N. P. Butch, J. R. Jeffries, S. T. Weir, J. J. Hamlin, M. B. Maple, Y. K. Vohra, and J. Paglione, "Pressure-induced unconventional superconducting phase in the topological insulator Bi_2Se_3," *Phys. Rev. Lett.*, vol. 111, p. 087001, 2013.

[35] L. He, Y. Jia, S. Zhang, X. Hong, C. Jin, and S. Li, "Pressure-induced superconductivity in the three-dimensional topological Dirac semimetal Cd_3As_2," *npj Quantum Materials*, vol. 1, no. 1, p. 16014, 2016.

[36] Y. Zhou, J. Wu, W. Ning, N. Li, Y. Du, X. Chen, R. Zhang, Z. Chi, X. Wang, X. Zhu, P. Lu, C. Ji, X. Wan, Z. Yang, J. Sun, W. Yang, M. Tian, Y. Zhang, and H. kwang Mao, "Pressure-induced superconductivity in a three-dimensional topological material $ZrTe_5$," *Proceedings of the National Academy of Sciences*, vol. 113, no. 11, pp. 2904–2909, 2016.

[37] E. Cheng, W. Xia, X. Shi, Z. Yu, L. Wang, L. Yan, D. C. Peets, C. Zhu, H. Su, Y. Zhang, D. Dai, X. Wang, Z. Zou, N. Yu, X. Kou, W. Yang, W. Zhao, Y. Guo, and S. Li, "Pressure-induced superconductivity and topological phase transitions in the topological nodal-line semimetal $SrAs_3$," *npj Quantum Materials*, vol. 5, no. 1, p. 38, 2020.

[38] Y. Furue, T. Fujino, M. V. Salis, H. Leng, F. Ishikawa, T. Naka, S. Nakano, Y. Huang, A. de Visser, and A. Ohmura, "Superconducting and structural properties of the type-I superconductor $PdTe_2$ under high pressure," *Phys. Rev. B*, vol. 104, p. 144510, 2021.

[39] M. S. Bahramy, O. J. Clark, B.-J. Yang, J. Feng, L. Bawden, J. M. Riley, I. Markovic, F. Mazzola, V. Sunko, D. Biswas, S. P. Cooil, M. Jorge, J. W. Wells, M. Leandersson, T. Balasubramanian, J. Fujii, I. Vobornik, J. E. Rault, T. K. Kim, M. Hoesch, K. Okawa, M. Asakawa, T. Sasagawa, T. Eknapakul, W. Meevasana, and P. D. C. King, "Ubiquitous formation of bulk Dirac cones and topological surface states from a single orbital manifold in transition-metal dichalcogenides," *Nature Mat.*, vol. 17, p. 21, 2018.

[40] M. Yan, H. Huang, K. Zhang, E. Wang, W. Yao, K. Deng, G. Wan, H. Zhang, M. Arita, H. Yang, Z. Sun, H. Yao, Y. Wu, S. Fan, W. Duan, and S. Zhou, "Lorentz-violating type-II Dirac fermions in transition metal dichalcogenide $PtTe_2$," *Nature Comm.*, vol. 8, p. 257, 2017.

[41] F. Fei, X. Bo, R. Wang, B. Wu, J. Jiang, D. Fu, M. Gao, H. Zheng, Y. Chen, X. Wang, H. Bu, F. Song, X. Wan, B. Wang, and G. Wang, "Nontrivial berry phase and type-II Dirac transport in the layered material $PdTe_2$," *Phys. Rev. B*, vol. 96, p. 041201, 2017.

[42] H.-J. Noh, J. Jeong, E.-J. Cho, K. Kim, B. I. Min, and B.-G. Park, "Experimental realization of Type-II Dirac Fermions in a $PdTe_2$ superconductor," *Phys. Rev. Lett.*, vol. 119, p. 016401, 2017.

[43] O. J. Clark, M. J. Neat, K. Okawa, L. Bawden, I. Marković, F. Mazzola, J. Feng, V. Sunko, J. M. Riley, W. Meevasana, J. Fujii, I. Vobornik, T. K. Kim, M. Hoesch, T. Sasagawa, P. Wahl, M. S. Bahramy, and P. D. C. King, "Fermiology and superconductivity of topological surface states in $PdTe_2$," *Phys. Rev. Lett.*, vol. 120, p. 156401, 2018.

[44] H. Leng, C. Paulsen, Y. K. Huang, and A. de Visser, "Type-I superconductivity in the Dirac semimetal $PdTe_2$," *Phys. Rev. B*, vol. 96, p. 220506, 2017.

[45] S. Teknowijoyo, N. H. Jo, M. S. Scheurer, M. A. Tanatar, K. Cho, S. L. Bud'ko, P. P. Orth, P. C. Canfield, and R. Prozorov, "Nodeless superconductivity in the type-II Dirac semimetal $PdTe_2$: London penetration depth and pairing-symmetry analysis," *Phys. Rev. B*, vol. 98, p. 024508, 2018.

[46] M. V. Salis, P. Rodière, H. Leng, Y. K. Huang, and A. de Visser, "Penetration depth study of the type-I superconductor PdTe2," *Journal of Physics: Condensed Matter*, vol. 30, no. 50, p. 505602, 2018.

[47] Amit and Y. Singh, "Heat capacity evidence for conventional superconductivity in the type-II Dirac semimetal $PdTe_2$," *Phys. Rev. B*, vol. 97, p. 054515, 2018.

[48] M. V. Salis, Y. K. Huang, and A. de Visser, "Heat capacity of type-I superconductivity in the Dirac semimetal $PdTe_2$," *Phys. Rev. B*, vol. 103, p. 104502, 2021.

[49] S. Das, Amit, A. Sirohi, L. Yadav, S. Gayen, Y. Singh, and G. Sheet, "Conventional superconductivity in the type-II Dirac semimetal $PdTe_2$," *Phys. Rev. B*, vol. 97, p. 014523, 2018.

[50] A. Sirohi, S. Das, P. Adhikary, R. R. Chowdhury, A. Vashist, Y. Singh, S. Gayen, T. Das, and G. Sheet, "Mixed type I and type II superconductivity due to intrinsic electronic inhomogeneities in the type II dirac semimetal $PdTe_2$," *Journal of Physics: Condensed Matter*, vol. 31, no. 8, p. 085701, 2019.

[51] Z. Liu, X. Yao, J. Shao, M. Zuo, L. Pi, S. Tan, C. Zhang, and Y. Zhang, "Superconductivity with topological surface state in $Sr_xBi_2Se_3$," *Journal of the American Chemical Society*, vol. 137, no. 33, pp. 10512–10515, 2015.

[52] G. Du, J. Shao, X. Yang, Z. Du, D. Fang, J. Wang, K. Ran, J. Wen, C. Zhang, H. Yang, Y. Zhang, and H.-H. Wen, "Drive the Dirac electrons into Cooper pairs in $Sr_xBi_2Se_3$," *Nature Communications*, vol. 8, no. 1, p. 14466, 2017.

[53] C. Q. Han, H. Li, W. J. Chen, F. Zhu, M.-Y. Yao, Z. J. Li, M. Wang, B. F. Gao, D. D. Guan, C. Liu, C. L. Gao, D. Qian, and J.-F. Jia, "Electronic structure of a superconducting topological insulator Sr-doped Bi_2Se_3," *Applied Physics Letters*, vol. 107, no. 17, p. 171602, 2015.

[54] Y. Pan, A. M. Nikitin, G. K. Araizi, Y. K. Huang, Y. Matsushita, T. Naka, and A. de Visser, "Rotational symmetry breaking in the topological superconductor $Sr_xBi_2Se_3$ probed by upper-critical field experiments," *Scientific Reports*, vol. 6, p. 28632, 2016.

[55] K. Willa, R. Willa, K. W. Song, G. D. Gu, J. A. Schneeloch, R. Zhong, A. E. Koshelev, W.-K. Kwok, and U. Welp, "Nanocalorimetric evidence for nematic superconductivity in the doped topological insulator $Sr_{0.1}Bi_2Se_3$," *Phys. Rev. B*, vol. 98, p. 184509, 2018.

[56] P. F. Sullivan and G. Seidel, "Steady-state, ac-temperature calorimetry," *Phys. Rev.*, vol. 173, pp. 679–685, 1968.

[57] W. Nernst, "Sitzungsbericht der k," *Preuss. Akad. Wiss*, vol. 12, no. 261, p. 154, 1910.

[58] A. Eucken, "Über die bestimmung spezifischer wärmen bei tiefen temperaturen," *Physikalische Zeitschrift*, vol. 10, pp. 586–589, 1909.

[59] R. Bachmann, F. J. DiSalvo, T. H. Geballe, R. L. Greene, R. E. Howard, C. N. King, H. C. Kirsch, K. N. Lee, R. E. Schwall, H. Thomas, and R. B. Zubeck, "Heat capacity measurements on small samples at low temperatures," *Review of Scientific Instruments*, vol. 43, no. 2, pp. 205–214, 1972.

[60] S. Inaba, S. Oda, and K. Morinaga, "Heat capacity of oxide glasses measured by ac calorimetry," *Journal of Non-Crystalline Solids*, vol. 306, no. 1, pp. 42–49, 2002.

[61] N. F. Mott, "Conduction in non-crystalline materials," *The Philosophical Magazine: A Journal of Theoretical Experimental and Applied Physics*, vol. 19, no. 160, pp. 835–852, 1969.

[62] A. F. Deutz, R. Hulstman, and F. J. Kranenburg, "Automatic mutual inductance bridge for accurate ac susceptibility measurements from 1.2 to 300 k," *Review of Scientific Instruments*, vol. 60, no. 1, pp. 113–120, 1989.

[63] Attocube, *User manual attocube system' Positioners*, 2011.

[64] A. M. Nikitin, *On the phase diagram of the superconducting ferromagnetic UCoGe and other unconventional superconductors*. PhD thesis, University of Amsterdam, 2017.

[65] T. Nakanishi, N. Takeshita, and N. Môri, "A newly developed high-pressure cell by using modified Bridgman anvils for precise measurements in magnetic fields at low temperatures," *Review of Scientific Instruments*, vol. 73, no. 4, pp. 1828–1831, 2002.

[66] T. Nakanishi, M. Nicklas, G. Sparn, and F. Steglich, "Compact hydrostatic pressure cell for precise resistivity measurements up to 10 GPa using PPMS," *Journal of the Physical Society of Japan*, vol. 76, no. Suppl.A, pp. 223–225, 2007.

[67] F. Ishikawa, K. Fukuda, S. Sekiya, A. Kaeriyama, Y. Yamada, and A. Matsushita, "Pressure effects on CuO double chain superconductivity," *Journal of the Physical Society of Japan*, vol. 76, no. Suppl.A, pp. 92–95, 2007.

[68] A. Einstein, "Die plancksche theorie der strahlung und die theorie der spezifischen wärme," *Annalen der Physik*, vol. 327, no. 1, pp. 180–190, 1907.

[69] P. Debye, "Zur theorie der spezifischen wärmen," *Annalen der Physik*, vol. 344, no. 14, pp. 789–839, 1912.

[70] A. Tari, *The Specific Heat of Matter at Low Temperatures*. Imperial College Press, 2003.

[71] N. Ashcroft and N. Mermin, *Solid State Physics*. Cengage Learning, 2011.

[72] C. Kittel and P. McEuen, *Introduction to Solid State Physics*. John Wiley & Sons, Limited, 2018.

[73] D. C. Rorer, H. Meyer, and R. C. Richardson, "Specific heat of aluminum near its superconductive transition point," *Zeitschrift für Naturforschung A*, vol. 18, no. 2, pp. 130–140, 1963.

[74] F. London and H. London, "The electromagnetic equations of the supraconductor," *Proceedings of the Royal Society of London Series A*, vol. 149, p. 71, 1935.

[75] L. D. Landau and V. L. Ginzburg, "On the theory of superconductivity," *Zh. Eksp. Teor. Fiz.*, vol. 20, p. 1064, 1950.

[76] L. Landau and E. Lifshitz, *Chapter XIV - Phase transitions of the second kind and critical phenomena*. Oxford: Butterworth-Heinemann, 1980.

[77] M. Tinkham, *Introduction to Superconductivity*. Dover Publications, 2004.

[78] C. P. Poole, H. A. Farach, R. J. Creswick, and R. Prozorov, *Superconductivity*. Academic Press, Amsterdam, 2007.

[79] R. A. Hein and R. L. Falge, "Differential paramagnetic effect in superconductors," *Phys. Rev.*, vol. 123, pp. 407–415, 1961.

[80] S. Yonezawa and Y. Maeno, "Type-I superconductivity of the layered silver oxide Ag_5Pb_2O6," *Phys. Rev. B*, vol. 72, p. 180504, 2005.

[81] E. Helfand and N. R. Werthamer, "Temperature and purity dependence of the superconducting critical field, H_{c2}. II," *Phys. Rev.*, vol. 147, pp. 288–294, 1966.

[82] N. R. Werthamer, E. Helfand, and P. C. Hohenberg, "Temperature and purity dependence of the superconducting critical field, H_{c2}. III. Electron spin and spin-orbit effects," *Phys. Rev.*, vol. 147, pp. 295–302, 1966.

[83] A. M. Clogston, "Upper limit for the critical field in hard superconductors," *Phys. Rev. Lett.*, vol. 9, pp. 266–267, 1962.

[84] B. S. Chandrasekhar, "A note on the maximum critical field of high-field superconductors," *Applied Physics Letters*, vol. 1, no. 1, pp. 7–8, 1962.

[85] K. Maki, "Effect of Pauli paramagnetism on magnetic properties of high-field superconductors," *Phys. Rev.*, vol. 148, pp. 362–369, 1966.

[86] J. Ketterson, J. Ketterson, S. Song, and K. B, *Superconductivity*. Cambridge University Press, 1999.

[87] M. Tinkham, "Effect of fluxoid quantization on transitions of superconducting films," *Phys. Rev.*, vol. 129, pp. 2413–2422, 1963.

[88] L. N. Cooper, "Bound electron pairs in a degenerate fermi gas," *Phys. Rev.*, vol. 104, pp. 1189–1190, 1956.

[89] V. Mineev and K. Samokhin, *Introduction to Unconventional Superconductivity*. Taylor & Francis, London, 1999.

[90] P. Anderson, "Theory of dirty superconductors," *Journal of Physics and Chemistry of Solids*, vol. 11, no. 1, pp. 26–30, 1959.

[91] D. A. Bonn, S. Kamal, K. Zhang, R. Liang, D. J. Baar, E. Klein, and W. N. Hardy, "Comparison of the influence of Ni and Zn impurities on the electromagnetic properties of $YBa_2Cu_3O_{6.95}$," *Phys. Rev. B*, vol. 50, pp. 4051–4063, 1994.

[92] H. Huang, S. Zhou, and W. Duan, "Type-II Dirac fermions in the $PtSe_2$ class of transition metal dichalcogenides," *Phys. Rev. B*, vol. 94, p. 121117, 2016.

[93] J. Guggenheim, F. Hulliger, and J. Müller, "$PdTe_2$, a superconductor with CdI_2 structure," *Helv. Phys. Acta*, vol. 34, p. 408, 1961.

[94] Y. Liu, J.-Z. Zhao, L. Yu, C.-T. Lin, A.-J. Liang, C. Hu, Y. Ding, Y. Xu, S.-L. He, L. Zhao, G.-D. Liu, X.-L. Dong, J. Zhang, C.-T. Chen, Z.-Y. Xu, H.-M. Weng, X. Dai, Z. Fang, and X.-J. Zhou, "Identification of topological surface state in $PdTe_2$ superconductor by angle-resolved photoemission spectroscopy," *Chinese Physics Letters*, vol. 32, p. 067303, jun 2015.

[95] B. Rosenstein, B. Y. Shapiro, D. Li, and I. Shapiro, "Magnetic properties of type-I and type-II Weyl semimetals in the superconducting state," *Phys. Rev. B*, vol. 97, p. 144510, 2018.

[96] D. Saint-James and P. G. de Gennes, "Onset of superconductivity in decreasing fields," *Phys. Lett.*, vol. 7, p. 306, 1963.

[97] B. Y. Shapiro, I. Shapiro, D. Li, and B. Rosenstein, "Type I superconductivity in Dirac materials," *Journal of Physics: Condensed Matter*, vol. 30, no. 33, p. 335403, 2018.

[98] J. A. Voerman, J. C. de Boer, T. Hashimoto, Y. Huang, C. Li, and A. Brinkman, "Dominant s-wave superconducting gap in $PdTe_2$ observed by tunneling spectroscopy on side junctions," *Phys. Rev. B*, vol. 99, p. 014510, 2019.

[99] H. Leng, J.-C. Orain, A. Amato, Y. K. Huang, and A. de Visser, "Type-I superconductivity in the Dirac semimetal $PdTe_2$ probed by μSR," *Phys. Rev. B*, vol. 100, p. 224501, 2019.

[100] P. Garcia-Campos, Y. K. Huang, A. de Visser, and K. Hasselbach, "Visualization by scanning SQUID microscopy of the intermediate state in the superconducting Dirac semimetal $PdTe_2$," *Phys. Rev. B*, vol. 103, p. 104510, 2021.

[101] H. Leng, A. Ohmura, L. N. Anh, F. Ishikawa, T. Naka, Y. K. Huang, and A. de Visser, "Superconductivity under pressure in the Dirac semimetal $PdTe_2$," *Journal of Physics: Condensed Matter*, vol. 32, no. 2, p. 025603, 2019.

[102] L. Thomassen, "Über kristallstrukturen einiger binärer verbindungen der platinmetalle," *Z. Phys. Chem.*, vol. B2, p. 349, 1929.

[103] A. Lyons, D. Schleich, and A. Wold, "Crystal growth and characterization of PdTe2," *Mat. Res. Bull.*, vol. 11, p. 1155, 1976.

[104] G. R. Stewart, "Measurement of low-temperature specific heat," *Review of Scientific Instruments*, vol. 54, no. 1, pp. 1–11, 1983.

[105] D.-X. Chen, E. Pardo, and A. Sanchez, "Demagnetizing factors of rectangular prisms and ellipsoids," *Magnetics, IEEE Transactions on*, vol. 38, pp. 1742 – 1752, 2002.

[106] K. Kudo, H. Ishii, and M. Nohara, "Composition-induced structural instability and strong-coupling superconductivity in $Au_{1-x}Pd_xTe_2$," *Phys. Rev. B*, vol. 93, p. 140505, 2016.

[107] B. Mühlschlegel, "Die thermodynamischen funktionen des supraleiters," *Zeitschrift für Physik*, vol. 155, no. 3, pp. 313–327, 1959.

[108] R. Karl, F. Burri, A. Amato, M. Donegà, S. Gvasaliya, H. Luetkens, E. Morenzoni, and R. Khasanov, "Muon spin rotation study of type-I superconductivity: Elemental β-Sn," *Phys. Rev. B*, vol. 99, p. 184515, 2019.

[109] K. Kim, S. Kim, J. S. Kim, H. Kim, J.-H. Park, and B. I. Min, "Importance of the van hove singularity in superconducting $PdTe_2$," *Phys. Rev. B*, vol. 97, p. 165102, 2018.

[110] E. van Heumen, M. Berben, L. Neubrand, and Y. Huang, "Scattering rate collapse driven by a van hove singularity in the Dirac semimetal $PdTe_2$," *Phys. Rev. Materials*, vol. 3, p. 114202, 2019.

[111] T. Le, L. Yin, Z. Feng, Q. Huang, L. Che, J. Li, Y. Shi, and X. Lu, "Single full gap with mixed type-I and type-II superconductivity on surface of the type-II Dirac semimetal $PdTe_2$ by point-contact spectroscopy," *Phys. Rev. B*, vol. 99, p. 180504, 2019.

[112] G. Ryu, "Superconductivity in Cu-intercalated CdI_2-type $PdTe_2$," *Journal of Superconductivity and Novel Magnetism*, vol. 28, p. 3275, 2015.

[113] M. K. Hooda and C. S. Yadav, "Electronic transport properties of intermediately coupled superconductors: $PdTe_2$ and $Cu_{0.04}PdTe_2$," *Europhysics Letters*, vol. 121, no. 1, p. 17001, 2018.

[114] A. Vasdev, A. Sirohi, M. K. Hooda, C. S. Yadav, and G. Sheet, "Enhanced, homogeneously type-II superconductivity in cu-intercalated $PdTe_2$," *Journal of Physics: Condensed Matter*, vol. 32, no. 2, p. 125701, 2019.

[115] N. R. Werthamer, E. Helfand, and P. C. Hohenberg, "Temperature and purity dependence of the superconducting critical field, H_{c2}. iii. electron spin and spin-orbit effects," *Phys. Rev.*, vol. 147, p. 295, 1966.

[116] E. I. Timmons, S. Teknowijoyo, M. Kończykowski, O. Cavani, M. A. Tanatar, S. Ghimire, K. Cho, Y. Lee, L. Ke, N. H. Jo, S. L. Bud'ko, P. C. Canfield, P. P. Orth, M. S. Scheurer, and R. Prozorov, "Electron irradiation effects on superconductivity in $PdTe_2$: An application of a generalized Anderson theorem," *Phys. Rev. Research*, vol. 2, p. 023140, 2020.

[117] M. Tinkham, *Introduction to Superconductivity.* McGraw-Hill Inc., New York, 1996.

[118] A. Samoilenka and E. Babaev, "Microscopic derivation of superconductor-insulator boundary conditions for Ginzburg-Landau theory revisited: Enhanced superconductivity at boundaries with and without magnetic field," *Phys. Rev. B*, vol. 103, p. 224516, 2021.

[119] Y. Mizuguchi, S. Demura, K. Deguchi, Y. Takano, H. Fujihisa, Y. Gotoh, H. Izawa, and O. Miura, "Superconductivity in novel BiS_2-based layered superconductor $LaO_{1-x}F_xBiS_2$," *Journal of the Physical Society of Japan*, vol. 81, no. 11, p. 114725, 2012.

[120] J. Xing, S. Li, X. Ding, H. Yang, and H.-H. Wen, "Superconductivity appears in the vicinity of semiconducting-like behavior in $CeO_{1-x}F_xBiS_2$," *Phys. Rev. B*, vol. 86, p. 214518, 2012.

[121] S. Demura, Y. Mizuguchi, K. Deguchi, H. Okazaki, H. Hara, T. Watanabe, S. James Denholme, M. Fujioka, T. Ozaki, H. Fujihisa, Y. Gotoh, O. Miura, T. Yamaguchi, H. Takeya, and Y. Takano, "New member of BiS_2-based superconductor $NdO_{1-x}F_xBiS_2$," *Journal of the Physical Society of Japan*, vol. 82, no. 3, p. 033708, 2013.

[122] J. Rajveer, K. Anuj, K. S. Shiva, and V. P. S. Awana, "Synthesis and superconductivity of new BiS_2 based superconductor $PrO_{0.5}F_{0.5}BiS_2$," *J Supercond Nov Magn*, vol. 26, pp. 499–502, 2013.

[123] D. Yazici, K. Huang, B. White, A. Chang, A. Friedman, and M. Maple, "Superconductivity of F-substituted $LnOBiS_2$ (Ln=La, Ce, Pr, Nd, Yb) compounds," *Philosophical Magazine*, vol. 93, no. 6, pp. 673–680, 2013.

[124] A. Miura, Y. Mizuguchi, T. Takei, N. Kumada, E. Magome, C. Moriyoshi, Y. Kuroiwa, and K. Tadanaga, "Structures and optical absorption of Bi_2OS_2 and $LaOBiS_2$," *Solid State Communications*, vol. 227, pp. 19–22, 2016.

[125] C. C. Tsuei and J. R. Kirtley, "Pairing symmetry in cuprate superconductors," *Rev. Mod. Phys.*, vol. 72, pp. 969–1016, 2000.

[126] K. Ishida, Y. Nakai, and H. Hosono, "To what extent iron-pnictide new superconductors have been clarified: A progress report," *Journal of the Physical Society of Japan*, vol. 78, no. 6, p. 062001, 2009.

[127] H. Usui, K. Suzuki, and K. Kuroki, "Minimal electronic models for superconducting BiS_2 layers," *Phys. Rev. B*, vol. 86, p. 220501, 2012.

[128] X. Wu, J. Yuan, Y. Liang, H. Fan, and J. Hu, "g-wave pairing in BiS_2 superconductors," *EPL (Europhysics Letters)*, vol. 108, no. 2, p. 27006, 2014.

[129] T. Yildirim, "Ferroelectric soft phonons, charge density wave instability, and strong electron-phonon coupling in BiS_2 layered superconductors: A first-principles study," *Phys. Rev. B*, vol. 87, p. 020506, 2013.

[130] X. Wan, H.-C. Ding, S. Y. Savrasov, and C.-G. Duan, "Electron-phonon superconductivity near charge-density-wave instability in $LaO_{0.5}F_{0.5}BiS_2$: Density-functional calculations," *Phys. Rev. B*, vol. 87, p. 115124, 2013.

[131] C. T. Van Degrift, "Tunnel diode oscillator for 0.001 ppm measurements at low temperatures," *Review of Scientific Instruments*, vol. 46, no. 5, pp. 599–607, 1975.

[132] L. Jiao, Z. Weng, J. Liu, J. Zhang, G. Pang, C. Guo, F. Gao, X. Zhu, H.-H. Wen, and H. Q. Yuan, "Evidence for nodeless superconductivity in $NdO_{1-x}F_xBiS_2$ (x = 0.3 and 0.5) single crystals," *Journal of Physics: Condensed Matter*, vol. 27, no. 22, p. 225701, 2015.

[133] T. Yamashita, Y. Tokiwa, D. Terazawa, M. Nagao, S. Watauchi, I. Tanaka, T. Terashima, and Y. Matsuda, "Conventional s-wave superconductivity in BiS_2-Based $NdO_{0.71}F_{0.29}BiS_2$ revealed by thermal transport measurements," *Journal of the Physical Society of Japan*, vol. 85, no. 7, p. 073707, 2016.

[134] N. Kase, "Specific heat study of the BiS_2-based superconductor," *Journal of the Physical Society of Japan*, vol. 88, no. 4, p. 041007, 2019.

[135] H. Fröhlich, "Theory of the superconducting state. I. The ground state at the absolute zero of temperature," *Phys. Rev.*, vol. 79, pp. 845–856, 1950.

[136] A. Yamashita, H. Usui, K. Hoshi, Y. Goto, K. Kuroki, and Y. Mizuguchi, "Possible pairing mechanism switching driven by structural symmetry breaking in BiS_2-based layered superconductors," *Scientific Reports*, vol. 11, no. 1, p. 230, 2021.

[137] K. Hoshi, Y. Goto, and Y. Mizuguchi, "Selenium isotope effect in the layered bismuth chalcogenide superconductor $LaO_{0.6}F_{0.4}Bi(S,Se)_2$," *Phys. Rev. B*, vol. 97, p. 094509, 2018.

[138] Y. C. Chan, K. Y. Yip, Y. W. Cheung, Y. T. Chan, Q. Niu, J. Kajitani, R. Higashinaka, T. D. Matsuda, Y. Yanase, Y. Aoki, K. T. Lai, and S. K. Goh, "Anisotropic two-gap superconductivity and the absence of a Pauli paramagnetic limit in single-crystalline $LaO_{0.5}F_{0.5}BiS_2$," *Phys. Rev. B*, vol. 97, p. 104509, 2018.

[139] J. Wu, A. T. Bollinger, X. He, and I. Božović, "Spontaneous breaking of rotational symmetry in copper oxide superconductors," *Nature*, vol. 547, p. 432–435, 2017.

[140] R. Fernandes, A. Chubukov, and J. Schmalian, "What drives nematic order in iron-based superconductors?," *Nature Phys*, vol. 10, p. 97–104, 2014.

[141] T. Shibauchi, T. Hanaguri, and Y. Matsuda, "Exotic superconducting states in fese-based materials," *Journal of the Physical Society of Japan*, vol. 89, no. 10, p. 102002, 2020.

[142] T. Asaba, B. J. Lawson, C. Tinsman, L. Chen, P. Corbae, G. Li, Y. Qiu, Y. S. Hor, L. Fu, and L. Li, "Rotational Symmetry Breaking in a Trigonal Superconductor Nb-doped Bi_2Se_3," *Phys. Rev. X*, vol. 7, p. 011009, 2017.

[143] M. P. Smylie, H. Claus, U. Welp, W.-K. Kwok, Y. Qiu, Y. S. Hor, and A. Snezhko, "Evidence of nodes in the order parameter of the superconducting doped topological insulator $Nb_xBi_2Se_3$ via penetration depth measurements," *Phys. Rev. B*, vol. 94, p. 180510, 2016.

[144] K. Hoshi, M. Kimata, Y. Goto, T. D. Matsuda, and Y. Mizuguchi, "Two-fold-symmetric magnetoresistance in single crystals of tetragonal $BiCh_2$-based superconductor $LaO_{0.5}F_{0.5}BiSSe$," *Journal of the Physical Society of Japan*, vol. 88, no. 3, p. 033704, 2019.

[145] K. Hoshi, R. Kurihara, Y. Goto, M. Tokunaga, and Y. Mizuguchi, "Extremely high upper critical field in $BiCh_2$-based (Ch: S and Se) layered superconductor $LaO_{0.5}F_{0.5}BiS_{2-x}Se_x$ (x = 0.22 and 0.69)," *Scientific Reports*, vol. 12, no. 1, p. 288, 2022.

[146] D. Aoki, A. Huxley, E. Ressouche, D. Braithwaite, J. Flouquet, J.-P. Brison, E. Lhotel, and C. Paulsen, "Coexistence of superconductivity and ferromagnetism in URhGe," *nature*, vol. 413, pp. 613–616, 2001.

[147] N. T. Huy, A. Gasparini, D. E. de Nijs, Y. Huang, J. C. P. Klaasse, T. Gortenmulder, A. de Visser, A. Hamann, T. Görlach, and H. v. Löhneysen, "Superconductivity on the border of weak itinerant ferromagnetism in UCoGe," *Phys. Rev. Lett.*, vol. 99, p. 067006, 2007.

[148] D. Aoki, J.-P. Brison, J. Flouquet, K. Ishida, G. Knebel, Y. Tokunaga, and Y. Yanase, "Unconventional superconductivity in UTe_2," *Journal of Physics: Condensed Matter*, vol. 34, no. 24, p. 243002, 2022.

[149] X. Zhang, Q. Liu, J.-W. Luo, A. J. Freeman, and A. Zunger, "Hidden spin polarization in inversion-symmetric bulk crystals," *Nature Phys*, vol. 10, p. 387–393, 2014.

[150] D. Maruyama, M. Sigrist, and Y. Yanase, "Locally noncentrosymmetric superconductivity in multilayer systems," *Journal of the Physical Society of Japan*, vol. 81, no. 3, p. 034702, 2012.

[151] S.-L. Wu, K. Sumida, K. Miyamoto, K. Taguchi, T. Yoshikawa, A. Kimura, Y. Ueda, M. Arita, M. Nagao, S. Watauchi, I. Tanaka, and T. Okuda, "Direct evidence of hidden local spin polarization in a centrosymmetric superconductor $LaO_{0.55}F_{0.45}BiS_2$," *Nature Communications*, vol. 8, no. 1, p. 1919, 2017.

[152] K. Hoshi and Y. Mizuguchi, "Experimental overview on pairing mechanisms of $BiCh_2$-based (Ch: S, Se) layered superconductors," *Journal of Physics: Condensed Matter*, vol. 33, no. 47, p. 473001, 2021.

[153] E. Paris, Y. Mizuguchi, M. Y. Hacisalihoglu, T. Hiroi, B. Joseph, G. Aquilanti, O. Miura, T. Mizokawa, and N. L. Saini, "Role of the local structure in superconductivity of $LaO_{0.5}BiS_{2-x}Se_x$," *Journal of Physics: Condensed Matter*, vol. 29, no. 14, p. 145603, 2017.

[154] N. Kase, Y. Terui, T. Nakano, and N. Takeda, "Superconducting gap symmetry of the BiS_2-based superconductor $LaO_{0.5}F_{0.5}BiSSe$ elucidated through specific heat measurements," *Phys. Rev. B*, vol. 96, p. 214506, 2017.

[155] M. Schossmann and J. P. Carbotte, "Pauli limiting of the upper critical magnetic field," *Phys. Rev. B*, vol. 39, pp. 4210–4216, 1989.

[156] Shruti, P. Srivastava, and S. Patnaik, "Evidence for fully gapped strong coupling s-wave superconductivity in $Bi_4O_4S_3$," *Journal of Physics: Condensed Matter*, vol. 25, no. 31, p. 312202, 2013.

[157] G. Lamura, T. Shiroka, P. Bonfà, S. Sanna, R. De Renzi, C. Baines, H. Luetkens, J. Kajitani, Y. Mizuguchi, O. Miura, K. Deguchi, S. Demura, Y. Takano, and M. Putti, "*s*-wave pairing in the optimally doped $LaO_{0.5}F_{0.5}BiS_2$ superconductor," *Phys. Rev. B*, vol. 88, p. 180509, 2013.

[158] P. K. Biswas, A. Amato, C. Baines, R. Khasanov, H. Luetkens, H. Lei, C. Petrovic, and E. Morenzoni, "Low superfluid density and possible multigap superconductivity in the BiS_2-based layered superconductor $Bi_4O_4S_3$," *Phys. Rev. B*, vol. 88, p. 224515, 2013.

[159] T. Yoshida, M. Sigrist, and Y. Yanase, "Parity-mixed superconductivity in locally non-centrosymmetric system," *Journal of the Physical Society of Japan*, vol. 83, no. 1, p. 013703, 2014.

[160] R. C. Xiao, P. L. Gong, Q. S. Wu, W. J. Lu, M. J. Wei, J. Y. Li, H. Y. Lv, X. Luo, P. Tong, X. B. Zhu, and Y. P. Sun, "Manipulation of type-I and type-II Dirac points in $PdTe_2$ superconductor by external pressure," *Phys. Rev. B*, vol. 96, p. 075101, 2017.